THE UNIVERSITY *of* EDINBURGH

Structure and Mechanical Properties of Model Colloids at Liquid Interfaces

Rudi Mears

Doctor of Philosophy
The University of Edinburgh
August 2019

Abstract

Colloidal particles adsorbed to liquid interfaces appear in a broad range of industries such as foods, mining and oil recovery. Yet our understanding of such systems remains incomplete. This thesis aims to characterise a model sterically-stabilised colloid system. We will explore their structure, stress-strain relationship, and the theoretical models used to describe them. Since the high barrier to adsorption and high desorption energy of particles are influenced strongly by size, we focus on the effects of varying particle size. This also allows us to begin connecting our micron-sized colloids to smaller surface active species such as proteins.

We focus on the mechanical properties of the particle-laden interface, which are crucial to applications such as emulsion stabilisation, and complement this investigation with microscopic imaging. For simplicity, we focus on the less frequently investigated sterically-stabilised particles, as opposed to charge-stabilised particles. The imaging reveals that for unsonicated samples, the characteristic structure changes with particle size: while large (1 μm radius) particles are relatively ordered in a two-dimensional crystal, as particle size decreases aggregates start to appear.

This apparent difference persists in their stress response - which we measure using a Langmuir-Pockels trough - where the largest and most ordered particles can withstand the most stress before buckling the interface. However, once the number and size of aggregates are reduced by sonication, the variation in mechanical properties with particle size disappears and all sizes (from 1 μm radius down to 0.2 μm radius) show a comparable response, consistent with the behaviour of charge-stabilised particles.

With particle size shown to be unimportant in our range, we focus on the smallest particles and use another technique - oscillating pendant drop tensiometry: first, to further explore the interfacial rheology, and second to verify our Langmuir-Pockels trough measurements by another method. The second point is particularly important because literature reports of pendant drop and trough

measurements seem to show a surprising inconsistency: drop measurements often only model the effect of colloid adsorption while trough measurements often only include colloid interactions, and each model is consistent with their own data. We demonstrate a pendant drop experiment which can be modelled with interactions, and use this to develop the theoretical understanding of how colloidal particles affect the interfacial rheology, thereby offering an explanation for this apparent inconsistency. We also quantitatively characterise the scaling of our interactions with the surface density of particles, and find that it is not inconsistent with interfacial electrostatic interactions, as with charge-stabilised particles. This result agrees with an independent report which more directly measured interparticle interactions. Directly comparing the results of our pendant drop and trough measurements, we find consistency at low surface pressures and deviation at higher surface pressures. This is attributed to the limitations of the trough and our modelling at high surface pressures.

In chapter 7 we present the first observations in particle-laden interfaces of a new mechanism of particle expulsion we call collective particle detachment, which was predicted to occur for particle-laden interfaces in earlier works on elastic sheets at liquid interfaces. In this process, thousands of particles collectively detach from the interface after wrinkling, producing long tubular structures, much like those produced by the highly elastic BslA protein in similar conditions. This provides a clear and novel link between particle and protein behaviour.

Finally, having investigated particles as a model system for proteins, we perform oscillating pendant drop measurements on a model particle-like protein - ferritin - to explore the applicability of our colloidal understanding to proteins. We find that its dilational elastic modulus is linear with surface pressure, as it was for particles. By applying our particle-based model to ferritin, we find that its interactions are short-ranged, consistent with previous studies. We conclude with a discussion of particle-protein similarities - such as their high desorption energy - and differences, such as the compressibility and unfolding potential of proteins.

This thesis explores a model colloidal system and adds to the literature a new approach where we use the adaptability of colloidal particles (at the synthesis stage) to explore key variables for fundamental interfacial properties. In the process we develop an improved model for the effect of adsorbed particles on the interfacial rheology, which allows us to measure interparticle interactions at the interface. We find the novel phenomenon of collective particle detachment, and show that our sterically-stabilised particles behave as charge-stabilised particles at the interface. Future work might explore other crucial variables for interfacial properties such as the contact angle or anisotropy.

Declaration

I declare that this thesis was composed by myself, that the work contained herein is my own except where explicitly stated otherwise in the text, and that this work has not been submitted for any other degree or professional qualification except as specified.

(*Rudi Mears, August 2019*)

Acknowledgements

First and foremost, thanks to Job Thijssen for the guidance and advice he has given me over the past few years. I have noticed myself change for the better under this guidance, and I am very grateful for it. I hope that others after me will also benefit from his care and critical eye. Many thanks also to Cait MacPhee for her wisdom and support throughout my time.
I am very grateful to Andrew B. Schofield for the synthesis of a range of particle systems, which allowed me to explore a wide range of behaviour.
Thanks to Jochen Arlt for the creation of the imaging module which allowed me to study the interfacial structure during my experiments.
Thanks also to Andrew Garrie for his expertise and for constructing a number of useful devices which helped improve my experiments, especially the miniature Langmuir-Pockels trough which allowed me to observe the interfacial structure of a particle monolayer under compression in a confocal microscope.
Thanks to Davide Marenduzzo for the simulations of interfacial particle interactions which helped build my theoretical understanding.
Thanks also to all of the above and to Paul Clegg, Tiffany Wood, Keith Bromley, Iain Muntz, Katy Dickinson, Matthew Reeves for useful advice and discussions along the long road to completion.
Finally, thanks and love to Luiza and my family for their love and support.

Contents

List of Figures

List of Tables

Chapter 1

Introduction and Background

1.1 Abstract

We introduce and explain the significance of colloids and proteins adsorbed to fluid interfaces. We describe the theoretical foundations of interfacial rheology, the microscopic properties and interactions of colloidal particles, and the models which link colloidal particle properties to their rheology. Finally, we briefly review the interfacial rheology of colloidal particles and proteins.

1.2 Overview

Colloidal particles can adsorb to liquid interfaces, and have a number of applications in industries - foods, mining, and oil recovery to name a few [1–3]. Yet our understanding of such systems is incomplete: while the important interparticle interactions are understood, our knowledge of the relationship between these microscopic properties, the overall structure of the particle-laden surface, and the interfacial rheology is still developing. For instance in pendant drop experiments, the surface stress data are often explained by the adsorption energy alone, while in Langmuir trough experiments only the interaction energy is considered, when we would expect both energies to contribute. To address this problem, we examine a model system in terms of its structure and interfacial rheology. We aim to use the simplest particle possible - a homogeneous, sterically-stabilised, spherical particle - and explore the effect of changing particle size.
The remainder of this chapter will give an overview of the interfacial rheology of particles and proteins. We will explain exactly what we mean by interfacial rheology and what we intend to measure. Then, in chapter 2 we will explain our

experimental techniques - Langmuir trough and pendant drop measurements with fluorescent imaging - and their limitations. Chapter 3 presents our analysis of the structures formed by three sizes of particle when they adsorb to a flat interface and finds that their structure can depend on size. Chapter 4 studies the stress response of these particle-laden interfaces and shows that while there initially seems to be a variation with particle size, this disappears once the structures are prepared differently - using a dispersion sonicated immediately before use. Chapter 5 then explores the interfacial rheology of the smallest particle size we consider with drop tensiometry, and uses our model to explain the results. Chapter 6 attempts to unite the results from chapters 5 and 4, and shows their agreement. Chapter 7 discusses what happens when particle laden interfaces are stressed into yielding and presents a novel yielding mechanism for such interfaces. Finally, in chapter 8 we present our measurements of the interfacial rheology of ferritin as a model particle-like protein and we discuss the connections between protein and particle behaviour before summarising our conclusions in chapter 9.

1.3 Background on Interfacial Rheology

To describe the interfacial stress-deformation behaviour, we must first clarify how we model the interface between our two fluid phases. In reality this interface has a small but finite thickness, over which properties vary rapidly but continuously from their values in one bulk phase to their values in the other [4]. For some systems where the interface is thick (such as membranes) accounting for this finite thickness is sensible, but it is more usual to model the interface as a two-dimensional surface placed within the true three-dimensional interfacial region - the so-called Gibbs dividing surface [5]. In this model bulk properties are considered constant up to the interface, and at the interface the difference between the actual value and the bulk value is considered an excess associated only with the dividing surface. With this two-dimensional interface in hand, we can then associate with it an interfacial tension γ.

However when we turn to complex interfaces e.g. those formed by adsorption of extra components to the interface, it is important to be careful about what we call interfacial tension, as Verwijlen *et al.* point out [6]. Interfacial tension is a static, isotropic quantity which is defined by the extra energy associated with forming an interfacial layer, but if the interface is deformed additional stresses can be generated. Generally, the surface stress tensor $\boldsymbol{\sigma}$ can be written as a sum

of the tension $\sigma_{\alpha\beta}\boldsymbol{I}$ and extra deformation stress tensor $\boldsymbol{\sigma_e}$ as

$$\boldsymbol{\sigma} = \sigma_{\alpha\beta}(\Gamma)\boldsymbol{I} + \boldsymbol{\sigma_e} \tag{1.1}$$

for two immiscible phases α and β, a surface concentration Γ of an additional component, and with $\boldsymbol{I}$ the second order unit surface dyadic tensor [6]. While bulk materials are often considered incompressible, interfaces are highly compressible so we have to consider both compression and shear. A general deformation of an interface may be decomposed into dilational (area change at constant shape) and shear deformations (shape change at constant area), illustrated in figure 1.1.

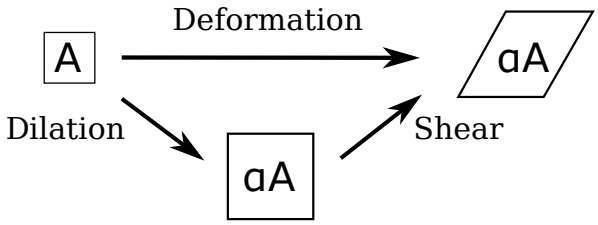

Figure 1.1 *Illustration of how the deformation of a square can be regarded as a composite of a dilation to a larger area αA, then shear to distort the shape without changing the total area.*

In order to analyse our interface independently of the specific geometry or bulk properties - which can vary across experiments - we have to extract material functions (discussed for bulk rheology in [7]) which describe how the material responds to stress; viscosity as a function of strain rate and stress is an example of a material function. To do that, we require a constitutive equation which will connect stress and strain. For example, for purely viscous interfaces one can use the linear Boussinesq-Scriven model [8], described for dilational and shear viscosities ν_d and ν_s by

$$\boldsymbol{\sigma}_{\boldsymbol{e}}^{\text{viscous}} = \nu_d \text{Tr}(\boldsymbol{D})\boldsymbol{I} + 2\nu_s \left(\boldsymbol{D} - \frac{1}{2}\text{Tr}(\boldsymbol{D})\boldsymbol{I} \right) \tag{1.2}$$

with $\boldsymbol{D}$ the rate-of-strain tensor, related to the deformation tensor $\boldsymbol{u}$ (which describes the strain) by $\boldsymbol{D} = \dot{\boldsymbol{u}} = d\boldsymbol{u}/dt$. The first term in equation 1.2 is the dilational response, and the second term is the shear response. However as we will see in sections 1.4 and 1.5, particles and proteins often show a significant elastic response. Purely elastic responses can be modelled by a generalization of Hooke's law, such that

$$\boldsymbol{\sigma}_{\boldsymbol{e}}^{\text{elastic}} = E_d \text{Tr}(\boldsymbol{u})\boldsymbol{I} + 2G_s \left(\boldsymbol{u} - \frac{1}{2}\text{Tr}(\boldsymbol{u})\boldsymbol{I} \right) \tag{1.3}$$

for surface dilational and shear moduli E_d and G_s and deformation tensor $\boldsymbol{u}$, again grouped by dilational and shear response. For our investigation we will look at viscoelastic properties, which can be captured by the Kelvin-Voigt model. This model is widely used, even if it is not explicitly specified, and can be represented by a simple spring in parallel with a single dashpot. The extra deformation stresses then simply add together to give the resultant stress from elastic and viscous contributions in the linear model, grouped into dilational and shear terms [9]:

$$\boldsymbol{\sigma_e^{KV}} = \boldsymbol{\sigma_e}^{\text{elastic}} + \boldsymbol{\sigma_e}^{\text{viscous}} \tag{1.4}$$

$$\begin{aligned}\boldsymbol{\sigma_e^{KV}} = &\underbrace{E_d(\mathrm{Tr}(\boldsymbol{u}))\boldsymbol{I} + \nu_d(\mathrm{Tr}(\boldsymbol{D}))\boldsymbol{I}}_{\text{dilational}} + \\ &\underbrace{2G_s\left[\boldsymbol{u} - \frac{1}{2}\mathrm{Tr}(\boldsymbol{u})\boldsymbol{I}\right] + 2\nu_s\left[\boldsymbol{D} - \frac{1}{2}\mathrm{Tr}(\boldsymbol{D})\boldsymbol{I}\right]}_{\text{shear}}\end{aligned} \tag{1.5}$$

Our investigations will focus on the dilational properties of interfaces, so let us use this constitutive equation to consider the extra stresses generated by a small purely dilational deformation, and allow the deformation to be oscillating sinusoidally with time t at angular frequency ω such that $\boldsymbol{u}(t) = \boldsymbol{u}_0 \exp[i(\omega t + \psi)]$. Then $\boldsymbol{D} = i\omega\boldsymbol{u}$ and we have

$$\boldsymbol{\sigma_e^{KV}} = (E_d + i\omega\nu_d)(\mathrm{Tr}(\boldsymbol{u}))\boldsymbol{I} = (E' + iE'')(\mathrm{Tr}(\boldsymbol{u}))\boldsymbol{I} = E^*\mathrm{Tr}(\boldsymbol{u})\boldsymbol{I} \tag{1.6}$$

where we have defined the dilational loss modulus as $E'' = \omega\nu_d$ and relabelled the dilational storage modulus E_d as E'. Here we have focused on a linear viscoelastic constitutive equation which, while limited to small strains [6], is widely used [4]. For small strains, the deformation of the interface described by the deformation tensor $\boldsymbol{u}$ is related to the displacement vector $\boldsymbol{e}(x, y)$ which describes the displacement of a point at (x, y) on the interface [10]. This relationship is usually represented by

$$u_{ij} = \frac{1}{2}\left(\frac{\partial e_i}{\partial x_j} + \frac{\partial e_j}{\partial x_i}\right) \tag{1.7}$$

with u_{ij}, e_i the components of $\boldsymbol{u}$ and $\boldsymbol{e}(x, y)$ and $x_1, x_2 = (x, y)$. Considering the dilational deformation of a small square with undeformed side length L and deformed length $L + \Delta L$, we find in this case that $\partial e_x/\partial x = \partial e_y/\partial y = \Delta L/L$ and $\partial e_y/\partial x = \partial e_x/\partial y = 0$. To first order the change in area $\Delta A = 2L\Delta L$ so the

deformation tensor becomes

$$\boldsymbol{u} = \frac{1}{2}\begin{pmatrix} \frac{\Delta A}{A} & 0 \\ 0 & \frac{\Delta A}{A} \end{pmatrix} \tag{1.8}$$

Substituting this into equation 1.6 yields

$$\boldsymbol{\sigma_e} = E^* \frac{\Delta A}{A} \boldsymbol{I} \tag{1.9}$$

With the assumption that the tension term ($\sigma^{\alpha\beta}(\Gamma)\boldsymbol{I}$) in equation 1.1 does not change during the deformation, we can then say that the magnitude of the isotropic change in surface stress sigma is

$$\Delta\sigma = E^* \frac{\Delta A}{A} \tag{1.10}$$

Or in the limit of small strains

$$E^* = \frac{\mathrm{d}\sigma}{\mathrm{d}\log(A)} = \frac{\frac{\mathrm{d}\sigma}{dt}}{\frac{\mathrm{d}\log(A)}{dt}} \tag{1.11}$$

This allows us to calculate the complex dilational modulus $E^* = E' + iE''$ from the measured tension $\sigma(t)$ and area $A(t)$ as a function of time t. When we describe our experimental methods in chapter 2 we will describe how we do this in detail. Extracting the complex dilational modulus allows us to analyse the interface in terms of its elastic response as measured by E' and its viscous response, which is related to E''. With our fundamental understanding of the dilational interfacial rheology in place, we can now discuss particles at interfaces.

1.4 Colloids at Fluid Interfaces

We will now discuss colloidal monolayers at liquid interfaces. These have been recently reviewed by several authors [1, 2, 8, 11–13] and discussed in two books [3, 14]. This section will provide a broad overview of the literature on spherical, homogeneous colloidal particles. We will discuss their adsorption, interactions, structure, dynamics, and interfacial rheology, expanding on certain aspects in later chapters.

1.4.1 Adsorption

Colloidal particles, like surfactant molecules, can spontaneously adsorb at fluid interfaces [3]. Unlike surfactant molecules, this adsorption need not be driven by an amphiphilic nature - though such 'Janus' particles do exist, see [15–17] for reviews. Even homogeneous colloidal particles can spontaneously accumulate at the interface because they block part of the water-oil interface, replacing it with water-particle and oil-particle interfaces. The particle thus acts as a preferable intermediary to the two immiscible phases. We can see this by considering the desorption energies of a such a particle, illustrated in figure 1.2. We will focus on situations where the interface around the particle is not significantly deformed due to gravity or other effects. The significance of gravitational deformation can be gauged by the magnitude of the Bond number [18] (also known as the Eötvös number) which describes the relative strength of gravitational to interfacial tension forces

$$\mathrm{Bo} = \frac{\Delta\rho g L^2}{\gamma}, \tag{1.12}$$

for a surface tension γ, difference in phase density $\Delta\rho$, lengthscale L and gravitational strength g. Our largest particles are around 1 μm in radius and sit at the water-dodecane interface ($\gamma_{wo} \approx 50mN/m$) and $\Delta\rho \approx 0.25$ g/mL, so we have $\mathrm{Bo} < 10^{-8}$. We can thus safely neglect this deformation. The free energy of desorption ΔG_d for a particle of radius r at an interface with tension γ_{ow} is then

$$\Delta G_d = \pi r^2 \gamma_{ow} \left(1 - |\cos(\theta)|\right)^2 . \tag{1.13}$$

The three-phase contact angle θ is a particularly important parameter for particles at interfaces, because of its significance to the desorption energy and because it relates to hydrophobicity. It is related to the interfacial tensions of each pair of phases by Young's equation

$$\cos(\theta) = \frac{\gamma_{po} - \gamma_{pw}}{\gamma_{ow}}. \tag{1.14}$$

For very small particles or non-spherical particles, it may be important to consider the effect of line tension [3, 19]. Line tension is the tension associated with the three-phase contact line, and while the magnitude and sign of this may vary considerably with system, radius, and conditions (dynamic or static) it is usually a small correction (for spherical particles at a flat interface) to the Young equation and can be neglected [14, 20].

From equation 1.13, typical interfacial tension values of several tens of mN/m,

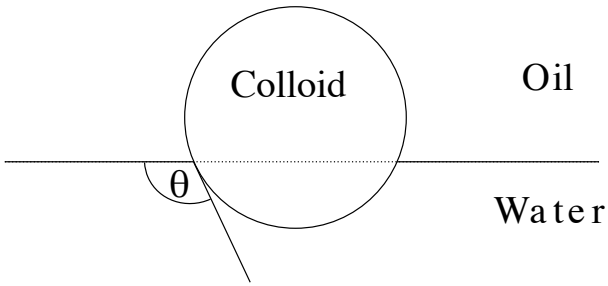

Figure 1.2 *Schematic of a colloidal particle adsorbed to a water-oil interface, showing the three-phase contact angle θ.*

and not too extreme contact angles we can see that even for particles only tens of nanometers in size that the desorption energy approaches $10^3 k_B T$ in contrast with 1-10$k_B T$ for amphiphilic molecules [21]. The dependence on r^2 means that this energy rapidly increases with size so that we may usually consider colloidal particles irreversibly adsorbed, in the sense that particles will not spontaneously desorb on experimental timescales.

While the adsorption is very thermodynamically favourable, this equilibrium may take some time to reach, for example because of energy barriers to adsorption arising from particle-interface interactions [21–23]. Once the particle begins adsorbing to the interface, if it is smooth it will quickly relax to its equilibrium depth into the interface. However, if it is rough, these inhomogeneities can greatly slow the acquisition of equilibrium by trapping the particle in metastable states on its way there [24, 25].

Dynamic interfacial tension measurements can be used to probe the kinetics of adsorption, provided the model used accounts for the irreversibility: the classical Ward and Tordai model [26] is unsuitable for irreversible adsorption, so use of the random sequential adsorption model is required [22, 27]. The kinetics of particle adsorption to a fluid interface also depends on the transport conditions - i.e. advection, convection, or diffusion. For diffusive conditions, the kinetics can be described by the evolution of the surface fraction $\phi(t)$

$$\phi(t) = 2\pi R^2 n_b \sqrt{\frac{Dt}{\pi}} \tag{1.15}$$

at a time t after adsorption begins, for colloid radius R, bulk diffusion constant D, and bulk concentration n_b. Equation 1.15 holds until ϕ approaches its maximum, and blocking effects become significant. In this thesis we will focus not on the adsorption process itself, but rather on the properties of the interface once particles have adsorbed to it.

1.4.2 Colloid Interfacial Interactions

Colloidal particles at an interface can interact with each other in various ways such as electrostatically, by capillary interactions, by steric repulsion, and by solvation interactions [3, 13, 21]. The interaction between particles in the monolayer depends on the fluids which form the interface as well as the nature of the adsorbed particle.

For example, charge-stabilised polystyrene particles spread at an air-water interface can be induced to aggregate by adding salt, but at the octane-water interface they remain ordered even at high salt concentrations [28]. This ordering is due to a dipole-dipole type repulsion arising from the mismatch in dielectric permittivity, which generates image charges if charges occur on one side of the interface, in addition to the screened Coulomb interaction which occurs in bulk [29, 30]. For an air-water interface, charges in the water phase (which can be screened) generate this dipole while for the oil-water interface the charges lie in the oil phase [13, 31].

The electrostatic interaction can be approximated for small ($e\psi_e \ll k_B T$) particle electrostatic potential ψ_e by solving the linear Poisson-Boltzmann equation to find the pair interaction potential $U_e(r)$ for separation r and inverse Debye length κ

$$U_e(r) = \underbrace{\frac{a_1 k_B T}{3r} \exp(-\kappa r)}_{\text{Screened monopole}} + \underbrace{\frac{a_2 k_B T}{r^3}}_{\text{Dipole}} \tag{1.16}$$

This was originally calculated by Hurd and improved upon by Masschaele *et al.* by the consideration of finite ion size effects in the Stern layer[29, 32]. The first term in equation 1.16 corresponds to a screened monopolar interaction, while the second term corresponds to a dipolar interaction which dominates at long range ($\kappa r \gg 10$).

Another interaction type particularly important for particles with higher Bond numbers is the capillary interaction. Particles which deform the interface can be driven together to minimise the surface free energy of the system. For gravitational deformation between like colloids, this is attractive. But particles can also deform the interface by having rough surfaces or anisotropic shapes, and these deformations can be both attractive and repulsive [33–35]. Further, deformations can be induced by an electric field (this is termed 'electrodipping' [3, 36]) which then causes capillary interaction. While gravitational deformations are unlikely to be significant in our system, it is important to be aware that these other types of deformation may occur even for particles as small as 10 nm [13].

While electrostatic and capillary forces are usually long-ranged, van der Waals forces become important at shorter ranges. Between like particles, the van der Waals interaction is always attractive [37]. Quantifying it for particles at an interface is more difficult than for particles in bulk, though it can be approximated by

$$U_{vdW}(r) \approx -\frac{A_i}{12}\frac{R}{r-2R} \tag{1.17}$$

for short-ranges ($r-2R \ll R$) for particles of radius R [3]. The effective Hamaker constant A_i is estimated from a combination of the Hamaker constants in each phase (A_1,A_2) and the contact angle θ [38]. Ignoring interactions between parts of the particle in different phases, this leads to

$$A_i = A_1 + \frac{1}{4}(1-\cos(\theta))^2(2+\cos(\theta))(A_2 - A_1). \tag{1.18}$$

Another interaction largely important at short range is the hydrophobic interaction. The interaction of the particle with the surrounding fluid molecules affects their structure near the particle surface, increasing or decreasing its order compared to the structure far from it [3]. Depending on the hydrophilicity (which can be quantified by the contact angle θ) this interaction can be attractive or repulsive. In bulk aqueous solutions, hydrophobic attraction was found to be important for contact angles greater than 64° and was significantly stronger than the van der Waals force at very short (< 8 nm) range [39]. For planar surfaces the interaction was found to decay exponentially [40], and using the Derjaguin approximation we can estimate the interaction for particles at short-range as

$$U_{\text{hydrophobic}} = W_0 \exp(-(r-2R)/\lambda_0) \tag{1.19}$$

for constants W_0 and λ_0 describing the strength and range. Typical values for λ_0 are around 1 nm, which justifies using this approximation [37].

Finally, we turn to steric interactions. Polymer hairs are commonly used to stabilise colloids, either by grafting (chemisorption) or adsorption from bulk (physisorption) [37]. When adsorbed, they generate a repulsive interaction between coated surfaces by increasing the entropy as the surfaces approach because the polymer chains become increasingly restricted. Theories of this interaction are complex, depending on coverage, whether the polymer is grafted or adsorbed, and the quality of the solvent. We might approximate the interaction by the de Gennes equation for a polymer brush of length L_p and density σ (molecules

per area) as

$$U_{\text{steric}} \approx RL^2\sigma^{3/2}\left(\frac{2L}{r-2R}\right)^{1/4} \tag{1.20}$$

for short ranges [13], but we should bear in mind that it depends on the details of the steric hairs. Despite the complexity, steric interactions are unlikely to be significant at separations beyond twice the length of the polymer hairs.

For our system of sterically-stabilised particles, we expected that steric repulsion and roughness-induced capillary attraction would be the most significant interactions. However, we will see in chapter 3 that there is a significant long-range repulsion at the interface, which we attribute to electrostatic repulsion arising either from dissociated PHSA groups on the particle surface, or the natural charge on the water-oil interface which leads particles to act as holes in a charged plane - see chapter 5 for a detailed discussion.

1.4.3 Colloid Interfacial Structure

Colloidal particle interactions at the interface are an important part of what structure is formed there, though dynamics, thermal forces, and external factors such as gravity or applied magnetic fields can also be relevant [3, 41–43]. The possible structures of self-assembled colloidal monolayers range from well ordered arrays to disordered aggregates and gel-like structures.

Generally, repulsive particle-particle interactions will induce order and strong attractive interactions will lead to a less ordered structure but this can depend on the dynamics. For example if charge-stabilised particles have a long-range electrostatic repulsion, but attractive van der Waals forces can bind the particles at short range, then the system may be trapped in a largely ordered structure even if aggregation is thermodynamically favourable [3].

The structure is important to certain technological applications such as photonic crystals and lithography masks [44, 45], and it is also connected to the interfacial rheology of the interface. For example Petkov *et al.* showed that aggregation could increase the surface pressure, and Razavi *et al.* observed different surface pressure responses and interfacial structure for different degrees of hydrophobization [46, 47].

1.4.4 Colloid Interfacial Rheology

The interfacial rheology of colloidal monolayers is dependent on the factors we have discussed so far: adsorption, interactions, and structure. The interfacial

rheology is the lens we will use to understand particles as a model system for proteins, so naturally it is important that we first understand the rheology of particles. Investigations of this have usually focused on charge-stabilised particles, though there has been recent interest in sterically-stabilised particles [2]. Because we seek the simplest possible model system, and the charge distribution around particles is system-dependant and complicated by the asymmetry introduced by the interface, we will focus on sterically-stabilised particles. Van Hooghten *et al.* have argued that depending on the system, either shear or dilational rheology may be dominant [2]. They found that dilational rheology dominates for the sterically-stabilised PHSA-PMMA particles we will use here (described in detail in chapter 2) so we will focus on that aspect.

Dilational properties are thought to be relevant in processes such as Ostwald ripening - e.g. through the Gibbs criterion which provides a lower limit for the elastic modulus if the system is to be stable against ripening in the form $E' > \gamma/2$ and its refinements [48]. They also offer useful insight into relaxation processes at the interface [12, 49].

To characterise the dilational rheology, authors most commonly use Langmuir trough (LT) and pendant drop (PD) tensiometry experiments and report the dilational elastic modulus, though other techniques such as studying capillary wave propagation or capillary pressure tensiometry are also used [4, 50, 51]. For this reason we will focus on both LT and PD measurements to probe the dilational interfacial rheology. In chapter 5 we will highlight and discuss a discrepancy between LT and PD measurements in the literature, and in chapter 6 we will make direct comparisons between our own LT and PD experiments to further this discussion and verify our own measurements.

Finally, we note that one of the most basic properties of our sterically-stabilised particles is their size. Therefore we will focus on the effect of particle size on the interfacial rheology. We will discuss the background literature on the effect of particle size and present our comparison of three particle sizes in chapter 4. In the next section we will describe the existing theoretical models for colloid interfacial rheology.

1.4.5 Modelling Colloid Interfacial Rheology

We now discuss thermodynamic approaches to modelling the surface pressure of colloidal particles adsorbed to fluid interfaces. This work has developed in close collaboration with my supervisor Dr. Thijssen, and a corresponding manuscript is in preparation [52].

Grand Canonical Ensemble Approach

We begin by considering what surface tension means for an interface with adsorbed colloidal particles, and how it relates to the particles' properties. One way to do this is to consider the bulk phases and interface as one grand canonical ensemble as done for surfactants [53]. We then assume that the grand canonical free energy can be written as a sum of the free energies of each bulk phase α and β and the interface

$$G = G_\alpha + G_\beta + G_I. \tag{1.21}$$

These are extensive quantities, proportional to the volume and area of each component of the system such that

$$G_\alpha = V_\alpha g_\alpha(T, \mu_i) \tag{1.22}$$

$$G_\beta = V_\beta g_\beta(T, \mu_i) \tag{1.23}$$

$$G_I = A\gamma(T, \mu_i). \tag{1.24}$$

By considering the total differential of G_I [53], it can be shown that the force acting on a length in the interface i.e. the physical interfacial tension is equal to the $\gamma(T, \mu_i)$ defined by equations 1.21 and 1.24, and we therefore have

$$\gamma = G_I/A. \tag{1.25}$$

Or, in terms of the commonly used surface pressure defined by $\Pi = \gamma_0 - \gamma$ (γ_0 is the interfacial tension of the bare interface) we find

$$\Pi = \gamma_0 - G_I/A. \tag{1.26}$$

Canonical Ensemble Approach

But for colloids the high desorption energy means that chemical equilibrium might not be attained on an experimental timescale, so a more suitable description for such a case would be to consider the interface as a canonical ensemble. We then consider the interface as the whole system, with constant temperature T, area A and number of adsorbed particles N. For this system the appropriate free energy is the Helmholtz free energy $F(A, T, N)$. To express this extensive free energy in terms of its extensive and intensive parts, we suggest

$$F(A, T, N) = Af(T, \rho) \tag{1.27}$$

for a surface density $\rho = N/A$, so that the free energy density $f(T, \rho)$ is an intensive quantity. The full differential of the canonical free energy is [54]

$$\mathrm{d}F = \gamma \mathrm{d}A - S\mathrm{d}T + \mu \mathrm{d}N. \tag{1.28}$$

From equation 1.27

$$\mathrm{d}F = A\mathrm{d}f + f\mathrm{d}A = f\mathrm{d}A + A\left(\left(\frac{\partial f}{\partial T}\right)_{A,\rho}\mathrm{d}T + \left(\frac{\partial f}{\partial \rho}\right)_{A,T}\mathrm{d}\rho\right). \tag{1.29}$$

To compare this with equation 1.28, we have to put $\mathrm{d}\rho$ in terms of $\mathrm{d}N$ and $\mathrm{d}A$ using its definition $\rho = N/A$. This leads to

$$\mathrm{d}\rho = \frac{\mathrm{d}N}{A} - \rho\frac{\mathrm{d}A}{A} \tag{1.30}$$

which lets us express equation 1.29 as

$$\mathrm{d}F = \left(f - \rho\left(\frac{\partial f}{\partial \rho}\right)_{A,T}\right)\mathrm{d}A + A\left(\frac{\partial f}{\partial T}\right)_{A,\rho}\mathrm{d}T + \left(\frac{\partial f}{\partial \rho}\right)_{A,T}\mathrm{d}N. \tag{1.31}$$

Comparison with equation 1.28 yields

$$\gamma = f - \rho\left(\frac{\partial f}{\partial \rho}\right)_{A,T}. \tag{1.32}$$

In terms of the surface pressure this is

$$\Pi = \gamma_0 - f + \rho\left(\frac{\partial f}{\partial \rho}\right)_{A,T}. \tag{1.33}$$

Example: Non-interacting Particles

Is is useful at this point to ground this understanding with an example, both to predict the surface pressure for a realistic system and to compare the grand canonical and canonical approaches described above. Consider N non-interacting particles which each lower the free energy by $\epsilon_0(\theta)$ when they attach to the interface. The free energy and free energy density are then

$$F = \gamma_0 A - N\epsilon_0(\theta) \tag{1.34}$$

$$f = \frac{F}{A} = \gamma_0 - \rho\epsilon_0(\theta). \tag{1.35}$$

If we apply the grand canonical approach described above with $G_I = F$ and using equation 1.26, we find the surface pressure to be

$$\Pi_G = \gamma_0 - (\gamma_0 + \rho\epsilon_0(\theta)) = \rho\epsilon_0(\theta). \tag{1.36}$$

If we instead use equation 1.33 we find

$$\Pi_F = \gamma_0 - f + \rho\left(\frac{\partial f}{\partial \rho}\right)_{A,T} = \gamma_0 - \gamma_0 + \rho\epsilon_0(\theta) - \rho\epsilon_0(\theta) = 0. \tag{1.37}$$

This difference arises because the canonical approach measures the extractable work at constant interfacial particle number - so adsorption energies cannot contribute - and it highlights the importance of experimental conditions to the measured surface pressure. We will discuss this point further in chapter 5.

Example: Interacting Particles

Having examined non-interacting particles, let us now introduce interactions. The free energy density then becomes

$$f = \frac{F}{A} = \gamma_0 - \rho\epsilon_0(\theta) + \rho\bar{u}_p \tag{1.38}$$

for an internal energy per particle $\bar{u}_p$. Again using equation 1.26, we find

$$\Pi_G = \rho\epsilon_0(\theta) + \rho\bar{u}_p \tag{1.39}$$

while using equation 1.33 instead yields

$$\Pi_F = \rho^2\left(\frac{\partial \bar{u}_p}{\partial \rho}\right)_{A,T}. \tag{1.40}$$

We again see the significance of whether particle number or particle chemical potential is fixed.

In the above examples, we have neglected the discussion of entropy. This is because it is thought to be negligible in comparison to the enthalpic contribution discussed, as we will now demonstrate. One method of estimating the entropic contribution is to simply use the van der Waals equation for surface pressure [55]

$$\Pi_{vdW} = \underbrace{\frac{\Gamma k_B T}{1 - \Gamma/\Gamma_{\text{inf}}}}_{\text{entropic}} - \underbrace{\beta_{vdW}\Gamma^2}_{\text{enthalpic}}. \tag{1.41}$$

This is usually used for surfactant molecules, but since it is based on there being some number of sites and a smaller number of occupants for those sites it is not unreasonable to apply it to colloidal particles. If we take $1/\Gamma_{\text{inf}} = A/N$ at close packing and $1/\Gamma = 2/\Gamma_{\text{inf}}$ as typical values, then the entropic surface pressure for a hexagonal lattice is

$$\Pi_{\text{ent}} = \frac{N_p k_B T}{A} \approx \frac{0.9 k_B T}{2\sqrt{3} R^2} \tag{1.42}$$

While surfactant molecules provide surface pressures > 10 mN/m by this estimate, micrometer-sized colloidal particles generate $< 10^{-5}$ mN/m, so we can justify neglecting the entropy for large enough particles. We also note that particle radii of about a nanometer or less are needed to generate more than 1 mN/m of surface pressure by this estimate. That said, this method does not account for the entropy of the fluid molecules, and this is a low density approximation, so a more complete description is desirable.

In addition to our warning on the exclusion of entropy, we should also add that the grand canonical ensemble and canonical ensemble approaches are both based on the assumption of some sort of equilibrium. In the case of the grand canonical ensemble we assume equilibrium between the number of particles in the bulk and adsorbed to the interface. This may not be true for colloids which are adsorbed with a very high energy (compared to the thermal energy) and so may not desorb on experimental timescales. In the case of the canonical ensemble, we assume that particles can obtain their equilibrium interaction energy. This assumption may fail if the colloids become trapped in metastable states, for example during interfacial compression.

Various other models have been proposed to explain the connection between the particle interactions and surface pressure, which we described above. However, those models tend to focus on the effect of either adsorption or interaction, depending on the experiment. For example, Aveyard *et al.* only considered the forces between charged particles at an interface to calculate the surface pressure, while Du *et al.* considered only the adsorption energy and neglected interactions [23, 28]. Both found their models to be consistent with their results. We suggest this is due to the difference in experimental conditions, as mentioned above, though we will discuss this in detail in chapter 5.

1.5 Proteins at Fluid Interfaces

Fluid interfaces are common in food and nature, and proteins are the most ubiquitous surface active polymers in nature [56]. They adsorb to interfaces and form stable films which can stabilise foams and emulsions through steric or electrostatic repulsion - where the film acts as an armour - or through the interfacial rheology of the film as it resists destabilising deformations. This stabilising ability is crucial to many food products [57] and the interfacial rheology has relevance to several biological processes such as the function of lung alveoli. There, lung surfactant reduces the interfacial tension of the air-liquid interface and prevents collapse [58]. Interfacial rheology is also important in processes such as digestion and spider-silk fibre formation [56]. As an analytical technique it has been used to investigate the protein BslA [59], which has been shown to be a critical component in certain biofilms and has remarkably elastic interfacial properties [60].

Proteins can partition to a liquid interface, but their subsequent behaviour can be hard to predict, since proteins are polymers composed of a range of amino acid residues, which all affect their final structure and properties. Further, once adsorbed to the interface proteins may unfold or change conformation from their native state in bulk [57, 59, 61–63]. These conformational changes can then lead to different inter-protein interactions, for example through disulphide bonds to generate an interfacial gel [64]. This means that their properties and behaviour are very complex and not easily controllable, unlike colloidal particles. The interfacial behaviour of proteins has been addressed by a number of reviews [10, 56, 57, 61, 64–66] so we will only give a brief overview here. We will first describe why and how they adsorb to the interface. Then, we will discuss their interfacial dilational rheology and how it is modelled. We will return to this discussion in chapter 8, when we have described our colloid experiments and we are in a position to apply our understanding of the colloidal systems to the case of proteins.

1.5.1 Adsorption

Proteins are large molecules consisting of long chains of amino acid residues, folded into a specific structure. The variety allowed by these residues means that they are complex, amphipathic molecules with ionic, polar and non-polar regions [66]. This nature makes them surface active, though it remains unclear how much of this surface activity is attributable to their 'colloid' nature. As

for colloids, the kinetics of their adsorption to a fluid interface depends on the transport conditions but for diffusive conditions, the kinetics can be described by the evolution of the surface fraction $\phi(t)$

$$\phi(t) = 2\pi R^2 \sqrt{\frac{Dt}{\pi}} n_b \tag{1.43}$$

at a time t after adsorption begins, for protein size R, bulk diffusion constant D, and bulk concentration n_b. Like colloids, the adsorption constant (the equilibrium ratio of adsorption rate to desorption rate) is large ($> 10^3$) and the adsorption is typically considered irreversible [27, 57]. Equation 1.43 holds until ϕ approaches its maximum, and blocking effects become significant. Here, we will focus more on the rheology of the adsorbed layer than the kinetics of its formation because of the dependence on transport conditions.

1.5.2 Interfacial Rheology

The dilational interfacial rheology of proteins is typically measured in the same way as that of colloids is - by the Langmuir trough and oscillating pendant drop or oscillating bubble methods - to extract the dilational elastic modulus [4]. Usually the Kelvin-Voigt constitutive equation (see section 1.3) is employed, though often implicitly. By considering a number of commonly investigated proteins at various fluid interfaces, Lucassen-Reynders *et al.* found that the dilational interfacial rheology is generally viscoelastic but mainly elastic, and is dominated by three factors: *i*) how rigid the protein molecules are, *ii*) the non-ideality of the behaviour, i.e. the size of the entropic and enthalpic corrections to the ideal equation of state, and *iii*) the bare interfacial tension γ_0 [67]. Also, proteins may unfold or change conformation from their native state in bulk when they adsorb to the interface [57, 59, 61–63]. Flexible proteins such as β-casein do this much more readily than globular proteins. The extent of this unfolding depends on the fluid phases which form the interface [57, 67–69]. Conformational changes can lead to different inter-protein interactions, for example through disulphide bonds to generate an interfacial gel [64].

These behaviours limit the extent to which we can hope to model proteins with colloids, but there are significant similarities. For example, Cicuta *et al.* showed that both colloidal particles and β-lactoglobulin produced a master curve for the shear modulus as a function of frequency, which held for various surface concentrations [70]. More recently, Tcholakova *et al.* compared particles, globular proteins, and surfactants as emulsifiers and found that globular proteins can

indeed behave similarly to particles as an emulsifier depending on experimental conditions such as pH [65]. This comparison may also inform our understanding of colloid behaviour - Fainerman *et al.* used a model developed for proteins to understand surface pressure isotherms for micro and nano sized particles [71]. We discuss this model in the next section.

1.5.3 Modelling Protein Interfacial Rheology

One model for the effect of proteins on the interfacial dilational rheology is a two-dimensional solution model, where the interface is regarded as a mixture of the components available in the bulk [67, 72–74]. Further, the area occupied by the protein can be allowed to take different states to model the effect of compressibility. Following from equation 2 in [67], the predicted surface pressure Π takes the form

$$\Pi = -\frac{RT}{\omega_0}\left[\underbrace{\ln(1-\phi) + (1-\frac{\omega_0}{\omega})\phi}_{\text{entropic}} + \underbrace{a\phi^2}_{\text{enthalpic}}\right] \tag{1.44}$$

in terms of partial molar areas for solvent ω_0, the average protein partial molar area ω, the surface fraction ϕ, and a constant a reflecting the strength of the enthalpic contribution which is estimated by a first-order Flory-type model [72, 74]. The average partial area ω is calculated from the set of allowed areas and the adsorption of each state Γ_i by

$$\omega = \frac{\omega_1\Gamma_1 + \omega_2\Gamma_2 + \ldots}{\Gamma_1 + \Gamma_2 + \ldots} = \frac{\sum_{i\geq 1}\omega_i\Gamma_i}{\sum_{i\geq 1}\Gamma_i} = \frac{\sum_{i\geq 1}\omega_i\Gamma_i}{\Gamma} \tag{1.45}$$

defining the total adsorption as Γ. The adsorption of each state is then given by

$$b_i c = \frac{\omega\Gamma_i}{(1-\phi)^{\omega_i/\omega}}\exp\left[-2a(\omega_i/\omega)\phi\right] \tag{1.46}$$

for a bulk concentration c of protein and an equilibrium adsorption constant of b_i. Assuming equal adsorption probability for each protein state, all b_i are equal. Then, we can use equation 1.46 along with the fact that the sum of adsorptions Γ_i over all n possible area states is the total adsorption to find the distribution

of area states

$$\Gamma_i = (1-\phi)^{\omega_i/\omega} \exp\left[2a(\omega_i/\omega)\phi\right] b_i c \tag{1.47}$$

$$\Gamma = \sum_{i=1}^{n} \Gamma_i = \sum_{i=1}^{n} (1-\phi)^{\omega_i/\omega} \exp\left[2a(\omega_i/\omega)\phi\right] b_i c \tag{1.48}$$

$$\Gamma_i = \Gamma \frac{(1-\phi)^{(\omega_i-\omega_1)/\omega} \exp\left[2a((\omega_i-\omega_1)/\omega)\phi\right]}{\sum_{i=1}^{n}(1-\phi)^{(\omega_i-\omega_1)/\omega} \exp\left[2a((\omega_i-\omega_1)/\omega)\phi\right]} \tag{1.49}$$

The area states are modelled by allowing the possible area to range from $\omega_{\min} = \omega_1$ through $\omega_i = \omega_1 + (i-1)\omega_0$ to a maximum of $\omega_{\max} = \omega_1 + (n-1)\omega_0$, so that they are quantized in units of the solvent area ω_0. The $\omega_{\min}$, $\omega_{\max}$, and ω_0 can then take the roles of fitting parameters.

It is important to note that the partial molar areas ω_i are excess quantities because they are defined in terms of the surface excess quantities Γ_i by

$$\sum_{i\geq 0} \omega_i \Gamma_i = 1. \tag{1.50}$$

Therefore they depend on the choice of the Gibbs dividing surface. Because we include the excess of the solvent we must use a different convention to the usual Gibbs convention - where the excess of the solvent is defined as zero. Instead we choose the ω_i in equation 1.50 to be constant.

For a given surface fraction ϕ, we can find the average protein area ω by combining equation 1.45 and 1.49 to find

$$\omega = \frac{\sum_{i=1}^{n} \omega_i (1-\phi)^{(\omega_i-\omega_1)/\omega} \exp\left[2a((\omega_i-\omega_1)/\omega)\phi\right]}{\sum_{i=1}^{n}(1-\phi)^{(\omega_i-\omega_1)/\omega} \exp\left[2a((\omega_i-\omega_1)/\omega)\phi\right]} \tag{1.51}$$

which can then be solved for a given ϕ to yield the average protein area ω. We illustrate the model behaviour by plotting surface pressure Π as a function of surface coverage ϕ in figure 1.3a, and the average area as a function of ϕ in figure 1.3b. We can see that surface pressure increases with surface fraction, and the protein becomes more compact as surface fraction increases.

For the model parameters, we used the best fit values for the commonly studied milk protein β-lactoglobulin at an air/water interface from [67], which are tabulated in table 1.1. We note that for simplicity we have not included multilayer adsorption or two-dimensional condensation as Lucassen-Reynders *et al.* do [67]: equations 1.44, 1.46 and 1.49 have been found to be sufficient until the adsorption becomes too high [74–76].

To model the finding that above a critical bulk protein concentration the

Protein	ω_0 [m^2/mol]	ω_{min} [m^2/mol]	ω_{max} [m^2/mol]	a
β-LG	3.5×10^5	5.8×10^6	1.3×10^7	0.8

Table 1.1 *Parameters used for illustration of model.*

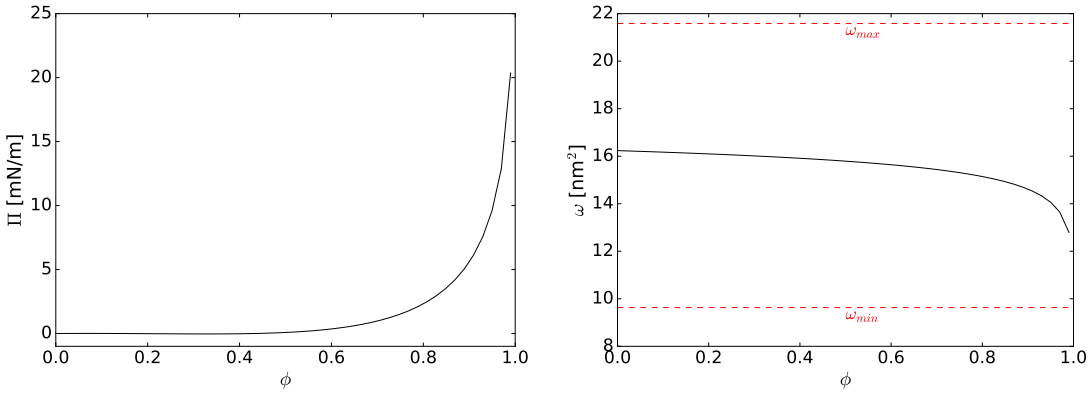

(a) **(b)**

Figure 1.3 *Protein model behaviour shown in terms of a) surface pressure and b) average partial protein area, each as a function of surface fraction.*

adsorption can increase while the surface pressure remains constant, aggregation can be included by modifying the expression for the average partial molar area ω of the proteins to account for this by

$$\omega^* = \omega \frac{\Gamma}{\Gamma^*} \exp\left[\frac{-\epsilon(\Pi - \Pi^*)\omega}{RT}\right] \tag{1.52}$$

where Γ^* and Π^* are the critical adsorption and surface pressure, and $\epsilon = 0.0-0.1$ is a parameter describing the decrease in area per molecule with condensation. Further, multilayer adsorption can be included in the model by allowing molecules to adsorb into other layers which do not affect the surface pressure, so that the total adsorption Γ_Σ is related to the monolayer adsorption Γ (the only layer which affects the surface pressure) by

$$\Gamma_\Sigma \approx \Gamma \sum_{i=1}^{m} \left(\frac{b_{\mathrm{II}} c}{1 + b_{\mathrm{II}} c}\right)^{i-1} \tag{1.53}$$

for m allowed multilayers, and adsorption constants b_{II} for each layer.
The refinements of condensation and multilayer adsorption are considered in the ProteinM software [77, 78], which we will use to apply the above model to our protein data in chapter 8.

1.6 Conclusions

We motivated the need for a simple model interfacial colloidal system, laid the theoretical foundations for our interfacial rheological investigation including a new model for colloid surface pressure, and gave a brief overview of what is known of the interfacial rheology of particles and proteins and how they are similar. In the next chapter, we detail the specific methods we will use to conduct the rheological investigation.

Bibliography

[1] J Thijssen and Jan Vermant. Interfacial rheology of model particles at liquid interfaces and its relation to (bicontinuous) pickering emulsions. *J. Phys. Condens. Matter*, 30:023002, 2018.

[2] Rob Van Hooghten, Victoria E Blair, Anja Vananroye, Andrew B Schofield, Jan Vermant, and Job HJ Thijssen. Interfacial rheology of sterically stabilized colloids at liquid interfaces and its effect on the stability of pickering emulsions. *Langmuir*, 33(17):4107–4118, 2017.

[3] Bernard P Binks and Tommy S Horozov. *Colloidal particles at liquid interfaces*. Cambridge University Press, 2006.

[4] Leonard MC Sagis. Dynamic properties of interfaces in soft matter: Experiments and theory. *Reviews of Modern Physics*, 83(4):1367, 2011.

[5] J Willard Gibbs. *The collected works of JW Gibbs*. Longmans, Green, 1928.

[6] T Verwijlen, L Imperiali, and J Vermant. Separating viscoelastic and compressibility contributions in pressure-area isotherm measurements. *Advances in colloid and interface science*, 206:428–436, 2014.

[7] Christopher W Macosko and Ronald G Larson. *Rheology: principles, measurements, and applications*. VCH New York, 1994.

[8] Philipp Erni. Deformation modes of complex fluid interfaces. *Soft Matter*, 7(17):7586–7600, 2011.

[9] Jordan T Petkov, Theodor D Gurkov, Bruce E Campbell, and Rajendra P Borwankar. Dilatational and shear elasticity of gel-like protein layers on air/water interface. *Langmuir*, 16(8):3703–3711, 2000.

[10] Reinhard Miller and Libero Liggieri. *Interfacial rheology*. CRC Press, 2009.

[11] Armando Maestro, Eva Santini, Dominika Zabiegaj, Sara Llamas, Francesca Ravera, Libero Liggieri, Francisco Ortega, Ramón G Rubio, and Eduardo Guzman. Particle and particle-surfactant mixtures at fluid interfaces: assembly, morphology, and rheological description. *Advances in Condensed Matter Physics*, 2015, 2015.

[12] Alma J. Mendoza, Eduardo Guzmán, Fernando Martínez-Pedrero, Hernán Ritacco, Ramón G. Rubio, Francisco Ortega, Victor M. Starov, and Reinhard Miller. Particle laden fluid interfaces: Dynamics and interfacial rheology. *Advances in Colloid and Interface Science*, 206:303–319, 2014.

[13] Valeria Garbin, John C. Crocker, and Kathleen J. Stebe. Nanoparticles at fluid interfaces: Exploiting capping ligands to control adsorption, stability and dynamics. *Journal of Colloid and Interface Science*, 387(1):1–11, 2012.

[14] P Kralchevsky and Kuniaki Nagayama. *Particles at fluid interfaces and membranes: attachment of colloid particles and proteins to interfaces and formation of two-dimensional arrays*, volume 10. Elsevier, 2001.

[15] Laura C Bradley, Wei-Han Chen, Kathleen J Stebe, and Daeyeon Lee. Janus and patchy colloids at fluid interfaces. *Current opinion in colloid & interface science*, 30:25–33, 2017.

[16] Andreas Walther and Axel HE Mller. Janus particles: synthesis, self-assembly, physical properties, and applications. *Chemical reviews*, 113(7):5194–5261, 2013.

[17] Adeline Perro, Stéphane Reculusa, Serge Ravaine, Elodie Bourgeat-Lami, and Etienne Duguet. Design and synthesis of janus micro-and nanoparticles. *Journal of materials chemistry*, 15(35-36):3745–3760, 2005.

[18] Moncho-Jordá Arturo Martínez-López Francisco Fernández-Toledano, Juan C. and Roque Hidalgo-Álvarez. Theory for interactions between particles in monolayers. In Bernard P Binks and Tommy S Horozov, editors, *Colloidal particles at liquid interfaces*, chapter 3, page 111. Cambridge University Press, 2006.

[19] Lichun Dong and Duane T Johnson. Adsorption of acicular particles at liquid- fluid interfaces and the influence of the line tension. *Langmuir*, 21(9):3838–3849, 2005.

[20] A Amirfazli and AW Neumann. Status of the three-phase line tension: a review. *Advances in colloid and interface science*, 110(3):121–141, 2004.

[21] Omkar S Deshmukh, Dirk van den Ende, Martien Cohen Stuart, Frieder Mugele, and Michel HG Duits. Hard and soft colloids at fluid interfaces: Adsorption, interactions, assembly & rheology. *Advances in colloid and interface science*, 222:215–227, 2015.

[22] Navid Bizmark, Marios A Ioannidis, and Dale E Henneke. Irreversible adsorption-driven assembly of nanoparticles at fluid interfaces revealed by a dynamic surface tension probe. *Langmuir*, 30(3):710–717, 2014.

[23] Kan Du, Elizabeth Glogowski, Todd Emrick, Thomas P Russell, and Anthony D Dinsmore. Adsorption energy of nano-and microparticles at liquid- liquid interfaces. *Langmuir*, 26(15):12518–12522, 2010.

[24] David M Kaz, Ryan McGorty, Madhav Mani, Michael P Brenner, and Vinothan N Manoharan. Physical ageing of the contact line on colloidal particles at liquid interfaces. *Nature materials*, 11(2):138, 2012.

[25] Carlos E Colosqui, Jeffrey F Morris, and Joel Koplik. Colloidal adsorption at fluid interfaces: regime crossover from fast relaxation to physical aging. *Physical review letters*, 111(2):028302, 2013.

[26] AFH Ward and L Tordai. Time-dependence of boundary tensions of solutions i. the role of diffusion in time-effects. *The Journal of Chemical Physics*, 14(7):453–461, 1946.

[27] Zbigniew Adamczyk. Kinetics of diffusion-controlled adsorption of colloid particles and proteins. *Journal of colloid and interface science*, 229(2):477–489, 2000.

[28] Robert Aveyard, John H Clint, Dieter Nees, and Vesselin N Paunov. Compression and structure of monolayers of charged latex particles at air/water and octane/water interfaces. *Langmuir*, 16(4):1969–1979, 2000.

[29] Alan J Hurd. The electrostatic interaction between interfacial colloidal particles. *Journal of Physics A: Mathematical and General*, 18(16):L1055, 1985.

[30] R Aveyard, BP Binks, JH Clint, PDI Fletcher, TS Horozov, B Neumann, VN Paunov, J Annesley, SW Botchway, D Nees, et al. Measurement of long-range repulsive forces between charged particles at an oil-water interface. *Physical review letters*, 88(24):246102, 2002.

[31] F Bresme and M Oettel. Nanoparticles at fluid interfaces. *Journal of Physics: Condensed Matter*, 19(41):413101, 2007.

[32] Kasper Masschaele, Bum Jun Park, Eric M Furst, Jan Fransaer, and Jan Vermant. Finite ion-size effects dominate the interaction between charged colloidal particles at an oil-water interface. *Physical review letters*, 105(4):048303, 2010.

[33] Dimitris Stamou, Claus Duschl, and Diethelm Johannsmann. Long-range attraction between colloidal spheres at the air-water interface: The consequence of an irregular meniscus. *Physical Review E*, 62(4):5263, 2000.

[34] Jean-Christophe Loudet, Arjun G Yodh, and Bernard Pouligny. Wetting and contact lines of micrometer-sized ellipsoids. *Physical review letters*, 97(1):018304, 2006.

[35] Eric P Lewandowski, Marcello Cavallaro Jr, Lorenzo Botto, Jorge C Bernate, Valeria Garbin, and Kathleen J Stebe. Orientation and self-assembly of cylindrical particles by anisotropic capillary interactions. *Langmuir*, 26(19):15142–15154, 2010.

[36] Krassimir D Danov, Peter A Kralchevsky, and Mariana P Boneva. Electrodipping force acting on solid particles at a fluid interface. *Langmuir*, 20(15):6139–6151, 2004.

[37] Jacob N Israelachvili. *Intermolecular and surface forces*. Academic press, 2011.

[38] David F Williams and John C Berg. The aggregation of colloidal particles at the airwater interface. *Journal of colloid and interface science*, 152(1):218–229, 1992.

[39] JN Israelachvili and RM Pashley. Measurement of the hydrophobic interaction between two hydrophobic surfaces in aqueous electrolyte solutions. *Journal of colloid and interface science*, 98(2):500–514, 1984.

[40] Hugo K Christenson and Per M Claesson. Cavitation and the interaction between macroscopic hydrophobic surfaces. *Science*, 239(4838):390–392, 1988.

[41] Peter HF Hansen and Lennart Bergström. Perikinetic aggregation of alkoxylated silica particles in two dimensions. *Journal of colloid and interface science*, 218(1):77–87, 1999.

[42] Tommy S Horozov, Robert Aveyard, Bernard P Binks, and John H Clint. Structure and stability of silica particle monolayers at horizontal and vertical octane- water interfaces. *Langmuir*, 21(16):7405–7412, 2005.

[43] Alexey Snezhko, IS Aranson, and W-K Kwok. Dynamic self-assembly of magnetic particles on the fluid interface: Surface-wave-mediated effective magnetic exchange. *Physical Review E*, 73(4):041306, 2006.

[44] Junhu Zhang, Zhiqiang Sun, and Bai Yang. Self-assembly of photonic crystals from polymer colloids. *Current Opinion in Colloid & Interface Science*, 14(2):103–114, 2009.

[45] Lucio Isa, Karthik Kumar, Mischa Muller, Jan Grolig, Marcus Textor, and Erik Reimhult. Particle lithography from colloidal self-assembly at liquid-liquid interfaces. *ACS nano*, 4(10):5665–5670, 2010.

[46] Plamen V Petkov, Krassimir D Danov, and Peter A Kralchevsky. Monolayers of charged particles in a langmuir trough: Could particle aggregation increase the surface pressure? *Journal of colloid and interface science*, 462:223–234, 2016.

[47] Sepideh Razavi, Kathleen D Cao, Binhua Lin, Ka Yee C Lee, Raymond S Tu, and Ilona Kretzschmar. Collapse of particle-laden interfaces under compression: buckling vs particle expulsion. *Langmuir*, 31(28):7764–7775, 2015.

[48] Alexandre I Romoscanu and Raffaele Mezzenga. Cross linking and rheological characterization of adsorbed protein layers at the oil- water interface. *Langmuir*, 21(21):9689–9697, 2005.

[49] Daniela Georgieva, Véronique Schmitt, Fernando Leal-Calderon, and Dominique Langevin. On the possible role of surface elasticity in emulsion stability. *Langmuir*, 25(10):5565–5573, 2009.

[50] Carole Planchette, Elise Lorenceau, and Anne-Laure Biance. Surface wave on a particle raft. *Soft Matter*, 8(8):2444–2451, 2012.

[51] L Liggieri, E Santini, E Guzmán, A Maestro, and F Ravera. Wide-frequency dilational rheology investigation of mixed silica nanoparticle–ctab interfacial layers. *Soft Matter*, 7(17):7699–7709, 2011.

[52] R Mears, I Muntz, and JHJ Thijssen. Surface pressure of a colloid-laden liquid interface. in preparation.

[53] Masao Doi. *Soft matter physics*. Oxford University Press, 2013.

[54] Charles Kittel and Herbert Kroemer. *Thermal Physics*. W. H. Freeman and Company, New York, 1999.

[55] Peter A Kralchevsky, Krassimir D Danov, and Plamen V Petkov. Soft electrostatic repulsion in particle monolayers at liquid interfaces: surface pressure and effect of aggregation. *Philosophical Transactions of the Royal Society A: Mathematical, Physical and Engineering Sciences*, 374(2072):20150130, 2016.

[56] Brent S Murray. Rheological properties of protein films. *Current Opinion in Colloid & Interface Science*, 16(1):27–35, 2011.

[57] Martin A Bos and Ton van Vliet. Interfacial rheological properties of adsorbed protein layers and surfactants: a review. *Advances in colloid and interface science*, 91(3):437–471, 2001.

[58] Minoru Ueno. Colloidal and interfacial properties of lung surfactants. *Membrane*, 27:233–43, 2002.

[59] Keith M Bromley, Ryan J Morris, Laura Hobley, Giovanni Brandani, Rachel MC Gillespie, Matthew McCluskey, Ulrich Zachariae, Davide Marenduzzo, Nicola R Stanley-Wall, and Cait E MacPhee. Interfacial self-assembly of a bacterial hydrophobin. *Proceedings of the National Academy of Sciences*, 112(17):5419–5424, 2015.

[60] Ryan J Morris, Keith M Bromley, Nicola Stanley-Wall, and Cait E MacPhee. A phenomenological description of bsla assemblies across multiple length scales. *Philosophical Transactions of the Royal Society A: Mathematical, Physical and Engineering Sciences*, 374(2072):20150131, 2016.

[61] Brent S Murray. Interfacial rheology of food emulsifiers and proteins. *Current opinion in colloid & interface science*, 7(5-6):426–431, 2002.

[62] BA Noskov, DO Grigoriev, AV Latnikova, S-Y Lin, G Loglio, and R Miller. Impact of globule unfolding on dilational viscoelasticity of β-lactoglobulin adsorption layers. *The Journal of Physical Chemistry B*, 113(40):13398–13404, 2009.

[63] Boris A Noskov. Protein conformational transitions at the liquid–gas interface as studied by dilational surface rheology. *Advances in colloid and interface science*, 206:222–238, 2014.

[64] Gerald G Fuller and Jan Vermant. Complex fluid-fluid interfaces: rheology and structure. *Annual review of chemical and biomolecular engineering*, 3:519–543, 2012.

[65] S Tcholakova, ND Denkov, and A Lips. Comparison of solid particles, globular proteins and surfactants as emulsifiers. *Physical Chemistry Chemical Physics*, 10(12):1608–1627, 2008.

[66] Eric Dickinson. Adsorbed protein layers at fluid interfaces: interactions, structure and surface rheology. *Colloids and surfaces B: Biointerfaces*, 15(2):161–176, 1999.

[67] EH Lucassen-Reynders, J Benjamins, and VB Fainerman. Dilational rheology of protein films adsorbed at fluid interfaces. *Current Opinion in Colloid & Interface Science*, 15(4):264–270, 2010.

[68] Julia Maldonado-Valderrama, Reinhard Miller, Valentin B Fainerman, Peter J Wilde, and Victor J Morris. Effect of gastric conditions on β-lactoglobulin interfacial networks: Influence of the oil phase on protein structure. *Langmuir*, 26(20):15901–15908, 2010.

[69] Jotam Bergfreund, Pascal Bertsch, Simon Kuster, and Peter Fischer. Effect of oil hydrophobicity on the adsorption and rheology of β-lactoglobulin at oil–water interfaces. *Langmuir*, 34(16):4929–4936, 2018.

[70] Pietro Cicuta, Edward J Stancik, and Gerald G Fuller. Shearing or compressing a soft glass in 2d: time-concentration superposition. *Physical review letters*, 90(23):236101, 2003.

[71] VB Fainerman, VI Kovalchuk, EH Lucassen-Reynders, DO Grigoriev, JK Ferri, ME Leser, M Michel, R Miller, and H Möhwald. Surface-pressure isotherms of monolayers formed by microsize and nanosize particles. *Langmuir*, 22(4):1701–1705, 2006.

[72] EH Lucassen-Reynders. Competitive adsorption of emulsifiers 1. theory for adsorption of small and large molecules. *Colloids and Surfaces A: Physicochemical and Engineering Aspects*, 91:79–88, 1994.

[73] VB Fainerman and R Miller. Equation of state for concentrated protein surface layers at the water/air interface. *Langmuir*, 15(5):1812–1816, 1999.

[74] VB Fainerman, EH Lucassen-Reynders, and R Miller. Description of the adsorption behaviour of proteins at water/fluid interfaces in the framework of a two-dimensional solution model. *Advances in colloid and interface science*, 106(1-3):237–259, 2003.

[75] Julia Maldonado-Valderrama, Valentin B Fainerman, Eugene Aksenenko, M Jose Gálvez-Ruiz, Miguel A Cabrerizo-Vílchez, and Reinhard Miller. Dynamics of protein adsorption at the oil–water interface: comparison with a theoretical model. *Colloids and Surfaces A: Physicochemical and Engineering Aspects*, 261(1-3):85–92, 2005.

[76] Günther Jutz. *Mineralized Bionanoparticle Pickering Emulsions*. PhD thesis, University of Bayreuth: Germany, 2008.

[77] EV Aksenenko. Software tools to interpret the thermodynamics and kinetics of surfactant adsorption. In *Studies in Interface Science*, volume 13, pages 619–648. Elsevier, 2001.

[78] Eugene Aksenenko. ProteinM Software Access. `http://www.thomascat.info/Scientific/AdSo/AdSo.htm`. [Online; accessed 25-May-2019].

Chapter 2

Experimental Methods and Materials

2.1 Abstract

This chapter discusses the experimental methods and materials used throughout this thesis, detailing the principles of each technique as well as their limitations and our calibration procedures. We discuss oscillating pendant drop tensiometry, the Langmuir-Pockels trough and interfacial imaging. We also describe the characterisation of our particles by size and contact angle. We measured radii of $r \approx 1100$ nm, $r \approx 450$ nm, and $r \approx 200$ nm by static and dynamic light scattering for three particle batches, allowing us to explore the effect of size variation in later chapters. For our largest particle size, we found the contact angle to be $\theta = 164.8 \pm 1.7°$, which is reasonable given previously reported values.

2.2 Introduction

In this chapter we describe the experimental and analytical techniques which are commonly used throughout this thesis, though we leave some details which are only used in one chapter - for example image processing - to that chapter. Here, we first describe the materials used and their preparation. Then, we describe two interfacial rheological techniques: oscillating pendant drop tensiometry and the Langmuir-Pockels trough. Following that, we describe the imaging apparatus used to complement those rheological techniques. Finally we describe the methods used to characterise the particle size and contact angle of our colloidal particles and present our measurement of those parameters.

2.3 Materials

We used poly(12-hydroxystearic acid) (PHSA) stabilised poly(methyl methacrylate) (PMMA) particles labelled with the fluorescent monomer, 7-nitrobenzo-2-oxa-1,3-diazole-methyl methacrylate (NBD-MMA), synthesised according to Jardine and Bartlett's method [1] by Andrew B. Schofield. We have not directly measured the excitation wavelength λ_{ex} and emission wavelength λ_{em} maxima for NBD-MMA, but Jardine and Bartlett reported $\lambda_{ex} = 472 \pm 2$ nm and $\lambda_{em} = 542 \pm 2$ nm [1]. For us it is only important to selectively image particles.
The particles are dispersed in n-dodecane (Acros Organics, 99% pure) to make a stock solution with a volume fraction of 1% measured by drying samples, which is sufficient for our purposes [2]. Samples of various volume fractions are then derived from that stock according to what is needed. Immediately before each experiment the mixture is shaken, then sonicated (VWR, USC300T) for at least 30 minutes at 45 kHz and 80 W to ensure good dispersion. The n-dodecane was purified before use by filtration of a 1 L batch through a 25 cm×4 cm alumina (Honeywell, Aluminium Oxide, activated, basic, Brockmann I) column three times. This is necessary to clean trace impurities in the oil phase [3].
Water was distilled, then deionised to a resistivity of 18 MΩ.cm. For pendant drop experiments where bubbles can disrupt the oscillations, water was then degassed by heating and stirring under reduced pressure for one hour.

2.4 Pendant drop tensiometry

Here we describe the technique of pendant drop tensiometry, first providing some background on the static drop, then the oscillating drop technique in section 2.4.1. Following that, in section 2.4.2 we describe our application of this technique, beginning with the preparation of a pendant drop, then the measurement of rheological parameters. Finally, in section 2.4.3 we test our assumptions and verify our measurements.

2.4.1 Background on Pendant Drop Tensiometry

Pendant drop tensiometry is a technique for measuring the interfacial tension γ of a pair of fluids such as water and air, or water and oil. It works by analysing the drop shape, which is captured by imaging the silhouette of an evenly backlit (i.e. by an extended, diffuse light source) fluid drop attached to a vertical needle. A single image provides us with γ, the drop area A, volume V, and data regarding

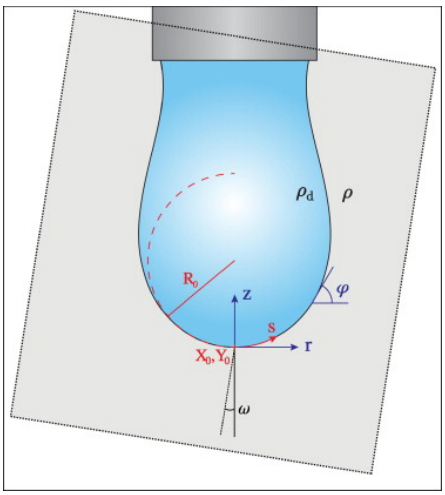

Figure 2.1 *Schematic of a pendant drop with labelled co-ordinate systems which are described in the text. Reproduced from [4] with permission.*

the quality of the fit (e.g. a profile of the residuals). It is based on the Young-Laplace equation, which relates the pressure difference ΔP across an interface to its curvature in terms of the principal radii of curvature $R_{c,1}$ and $R_{c,2}$ by

$$\Delta P = \gamma \left(\frac{1}{R_{c,1}} + \frac{1}{R_{c,2}} \right). \tag{2.1}$$

Assuming an isotropic interfacial tension, that the interface has a negligible bending modulus, and that the pressure difference is due only to the hydrostatic pressure, this can be expressed as a set of axisymmetric equations describing the shape [4]:

$$\frac{\mathrm{d}\psi}{\mathrm{d}\bar{s}} = 2 - \beta\bar{z} - \frac{\sin\psi}{\bar{r}} \tag{2.2}$$

$$\frac{\mathrm{d}\bar{r}}{\mathrm{d}\bar{s}} = \cos\psi \tag{2.3}$$

$$\frac{\mathrm{d}\bar{z}}{\mathrm{d}\bar{s}} = \sin\psi \tag{2.4}$$

Here z is the height above the drop apex, r is the perpendicular distance from the axis of symmetry, s is the arclength along the drop profile from the apex, and ψ is the tangent angle to the drop profile as shown in figure 2.1. The overbar denotes normalisation by R_0, the radius of curvature at the drop apex. The shape therefore depends only on the Bond number β, defined by:

$$\beta = \frac{\Delta\rho g R_0^2}{\gamma} \tag{2.5}$$

where $\Delta\rho = \rho_d - \rho_c$ is the density difference between the drop phase ρ_d and the continuous phase ρ_c surrounding it and g is the local acceleration due to gravity. Essentially, gravity tries to elongate the spherical shape preferred by surface tension. To recover information from the shape, we must first extract the drop profile by edge detection (e.g. in the OpenDrop software presented in [4] the Canny algorithm is used, which is well established [5]). Edge detection is not expected to be problematic and is rarely mentioned in the literature; a sharp profile edge is easily achievable.

Once the profile is extracted from the image - which is discretized as pixels - solutions to the shape equations are fit to it by minimising the sum of squared residuals. The drop must be in equilibrium, shielded from air currents and rapid temperature fluctuations, and spurious light sources must be eliminated. The best fit solution returns the Bond number β as well as the drop volume and area which are calculated by assuming an axisymmetric drop. Then by measuring R_0 from the image we can recover the interfacial tension using equation 2.5 since the density difference and local strength of gravity are known quantities.

Having discussed how a single image is analysed, we now turn to the oscillating drop. Oscillating the drop lets us probe the dilational rheology of the interface, which we discussed earlier in chapter 1. This is done by measuring how the dynamic interfacial tension $\gamma(t)$ responds as the drop area $A(t)$ is varied (by varying the drop volume $V(t)$): we measure a stress-strain relationship by controlling the strain.

The dynamic quantities $\gamma(t)$, $A(t)$, $V(t)$, and fit parameters are recorded for each image in a series of time-stamped images or video with known framerate, as we detailed above. The complex dilational modulus E^* is, for small sinusoidal strains (as shown earlier, see equation 1.11)

$$E^* = \frac{\mathrm{d}\gamma}{\mathrm{d}\ln(A)} = \frac{\frac{\mathrm{d}\gamma}{\mathrm{d}t}}{\frac{\mathrm{d}\ln(A)}{\mathrm{d}t}} \quad . \tag{2.6}$$

To find E^* from the set of interfacial tension, area and time points γ_i, A_i, t_i respectively, we assume that area and interfacial tension oscillate sinusoidally with amplitudes ΔA,$\Delta\gamma$ around their mean values A_m,γ_m such that at time t

$$A(t) = A_m + \Delta A \exp(i\omega t) \tag{2.7}$$

$$\gamma(t) = \gamma_m + \Delta\gamma_\omega \exp(i(\omega t + \psi)). \tag{2.8}$$

Using equation (2.6), this gives

$$E^* = \frac{\Delta\gamma}{\left(\frac{\Delta A}{A(t)}\right)} e^{i\psi}. \tag{2.9}$$

Which, to first order in $\Delta A/A_m$ is

$$E^* = \frac{\Delta\gamma}{\left(\frac{\Delta A}{A_m}\right)} e^{i\psi}. \tag{2.10}$$

Now we consider the ratio X, defining it as

$$X = \frac{\mathrm{FT}\left[\delta\gamma\right]}{\mathrm{FT}\left[\delta \ln(A)\right]} = \frac{\mathrm{FT}\left[\gamma_{i+1} - \gamma_i\right]}{\mathrm{FT}\left[\ln(A_{i+1}) - \ln(A_i)\right]}. \tag{2.11}$$

Substituting (2.7) and (2.8) into (2.11), we find

$$X = \frac{\mathrm{FT}\left[\Delta\gamma e^{i(\omega t_i + \psi)}\left(e^{i\omega(t_{i+1}-t_i)} - 1\right)\right]}{\mathrm{FT}\left[\ln\left(A_m + \Delta A e^{i(\omega t_{i+1})}\right) - \ln\left(A_m + \Delta A e^{i(\omega t_i)}\right)\right]}. \tag{2.12}$$

Taylor expanding the logarithms, this leads to

$$X = \frac{\mathrm{FT}\left[\Delta\gamma e^{i(\omega t_i + \psi)}\left(e^{i\omega(t_{i+1}-t_i)} - 1\right)\right]}{\mathrm{FT}\left[\frac{\Delta A}{A_m} e^{i(\omega t_i)}\left(e^{i\omega(t_{i+1}-t_i)} - 1\right) + \mathcal{O}\left(\left(\frac{\Delta A}{A_m}\right)^2\right)\right]}. \tag{2.13}$$

To first order in $\Delta A/A_m$ this leaves

$$X = \frac{\Delta\gamma}{\left(\frac{\Delta A}{A_m}\right)} e^{i\psi}. \tag{2.14}$$

This is the same as equation (2.10), thus showing that to first order in $\Delta A/A_m$, the dilational modulus can be found from a ratio of Fourier transforms as

$$E^* = \frac{\mathrm{FT}\left[\delta\gamma\right]}{\mathrm{FT}\left[\delta \ln(A)\right]}. \tag{2.15}$$

The process of extracting this dilational modulus from an image sequence is summarised in figure 2.2. We may further analyse how the modulus E^* develops over a timescale much larger than the video length by capturing several videos, and taking each to be a snapshot of E^*. This allows us to explore other variables such as frequency or ageing for example, which we do in chapter 5.

$$\text{Image Sequence} \xrightarrow[\text{Profile fit}]{\text{Edge detection}} \text{Surface tension } \gamma(t) \text{ Surface Area } A(t) \xrightarrow{\text{Equation 2.15}} \text{Complex dilational modulus } E^*$$

Figure 2.2 *Schematic showing the stages of analysis.*

2.4.2 Application of Pendant Drop Tensiometry

Having described the principles of pendant drop tensiometry, we move on to how we conducted our experiments. To capture images or videos of the drop and to extract the interfacial tension from those images we used a Krüss DSA100 drop tensiometer (which uses a 780 × 580 pixel CCD camera) controlled by a PC. A Krüss DS3265 surface rheology module (a PC-controlled piezoelectric pump) and a separate syringe pump (New Era, model NE-1000) were used to control the drop volume. A schematic of the instrument is shown in figure 2.3.

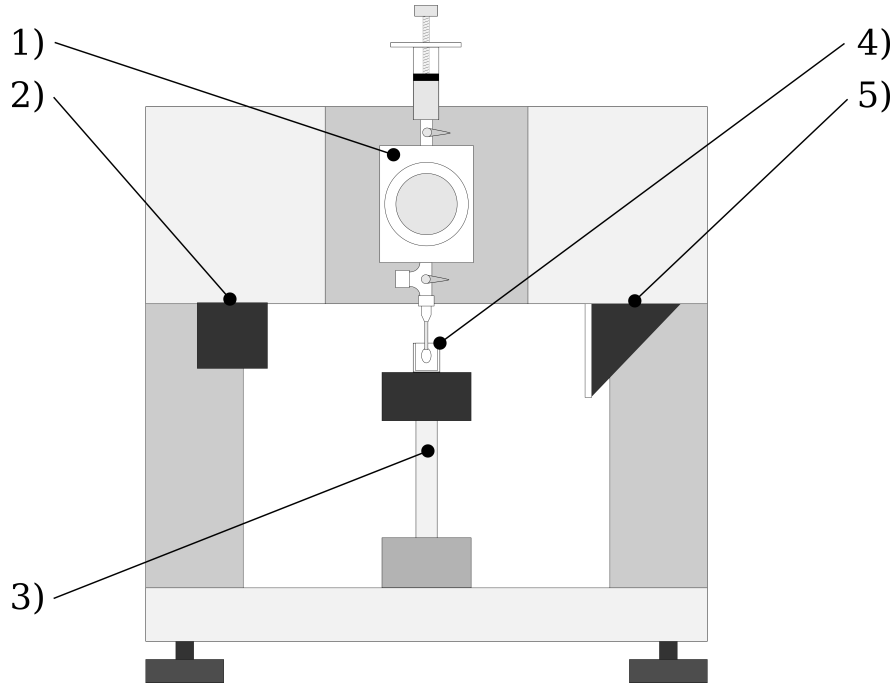

Figure 2.3 *Schematic of Krüss DSA100 drop tensiometer. 1) Computer-controlled piezoelectic pump for volume oscillations, 2) CCD camera and prism to reflect drop image into camera, 3) Moveable z-stage, 4) Glass cuvette and pendant drop suspended from needle, 5) Diffuse light source.*

To clean the system, glassware was first soaked overnight in 1 M NaOH, rinsed thoroughly with distilled water and ethanol, then dried and put to use. Between experiments the glass cuvette and the needle tip were sonicated for 15 minutes in toluene (Fisher, Analytical Reagent Grade) at 30 kHz and 80 W to dissolve the PHSA/PMMA particles, then rinsed thoroughly with ethanol (Fisher, Analytical

Reagent Grade) and dried before use.

To test for surface active contaminants we first measure the interfacial tension of the water-air interface and compare it to the expected value of 72.75±0.36 mN/m at 20 °C reported in [6] to verify that the water is clean. We then prepared a 55 μL drop of water in n-dodecane and compare its interfacial tension to the reported value of 52.55 ± 0.04 mN/m from [7] at 20 °C. An important source of contamination was the foil-lined caps of vials - the glue holding the foil lining to the cap was surface active and soluble in dodecane. We eliminated this by using wholly glass vials. Unfortunately the best value we could consistently achieve was around 50.5 mN/m with the lab thermostat at 22 °C (decreasing slightly (<1 mN/m) over an hour) despite following a comparable cleaning protocol to [7]. In section 2.4.3 we show that even ideal drop profiles do not yield the expected surface tension, so given the relatively stable (over time) value of the interfacial tension it is likely that this deficit is mainly due to the limitations of the apparatus.

Having calibrated our interfacial tension measurement, we calibrated our dilational modulus measurement by oscillating the drop at 10 Hz with a 4 % amplitude area strain. For a pure interface, the interfacial tension should be independent of area, and thus the dilational modulus should be zero. We found a storage modulus of $E' = 2.07 \pm 0.14$ mN/m and a loss modulus of $E'' = 0.08 \pm 0.08$ mN/m. We attribute this mainly to variation in apparent interfacial tension with area due to measurement errors, discussed below in section 2.4.3.

To prepare the colloid-laden interface we allowed colloids to spontaneously adsorb from one of the fluid phases, with various volume fractions. If the colloidal dispersion is the continuous phase we cannot use a volume fraction much higher than 0.2 % (depending on colloid size) because scattering from the bulk phase around the drop blurs the drop profile and prevents edge detection.

We can instead have the dispersion as the drop phase, and use a J-shaped needle so that the drop rises instead of hangs from a needle. In this case, much higher volume fractions can be used, but because we cannot fill the piezo-electric pump (shown in figure 2.3) with oil only the J-needle is filled with oil. In practice we found that this can make the volume oscillations of the drop jerky, perhaps due to air bubbles or perhaps due to movement of the three phase contact line of the oil-water-apparatus boundary internal to the needle and pump system. For this reason, we used a water-in-oil drop and a low volume fraction.

Once the interface is prepared, we can begin measuring the dynamic interfacial tension $\gamma(t)$ and dilational modulus E^* as described above.

2.4.3 Discussion and Verification of Pendant Drop Tensiometry

Now that we have described the principles and practical application of the pendant drop technique to our system we turn next to discuss the assumptions and validity of our measurements. We begin with the issues affecting a single interfacial tension measurement, then discuss the additional complications introduced by oscillation.

Recall from the derivation of equations 2.3-2.4 that interfacial tension measurement can be invalidated if there is anisotropy or additional bending resistance introduced by surface-active species such as surfactants or colloids. Theory exists to extract useful information such as the surface equivalent of a Young's modulus, Poisson ratio and interfacial bending modulus in that case [8], but here we focus on the simpler Young-Laplace fit described above which seems sufficient for most of our purposes.

This is appropriate for most of our measurements because the fit error parameter reported by the DSA4 software is around 1 μm, no more than for the pure water-dodecane case. This fit error - which is the mean squared deviation of the real profile from the fit - can rise to tens or hundreds of microns if the interface becomes solid and wrinkles e.g. under compression, but we do not use those measurements.

However the fit error cannot capture a fundamental limitation of drop tensiometry: as the drop volume decreases, the deviation from a spherical drop becomes smaller and harder to detect. This leads to the apparent interfacial tension γ_{app} deviating from the true interfacial tension γ as the drop volume is reduced, and introduces an artificial dependence of γ_{app} on the area. Berry *et al.* showed that the Worthington number $\mathrm{Wo} = V_d/V_{max}$ can indicate whether a measurement is likely to be accurate [4], where V_d is the drop volume, V_{max} is the maximum stable drop volume before gravity causes it to detach. The larger the drop volume, the better the accuracy.

To test the accurate range of our apparatus we first generated drop profiles of a known true interfacial tension by solving equations 2.3-2.4 for the drop profile numerically. We then mapped that solution onto a grid of pixels to match the image that would be generated by the instrument's camera, and fed this simulated image into the DSA4 analysis software to extract an apparent interfacial tension. If the instrument is working as intended, this apparent interfacial tension ought to match the known interfacial tension used to generate the simulated image.

The simulated drop image and the apparent interfacial tensions as a function of drop volume are shown in figure 2.4.

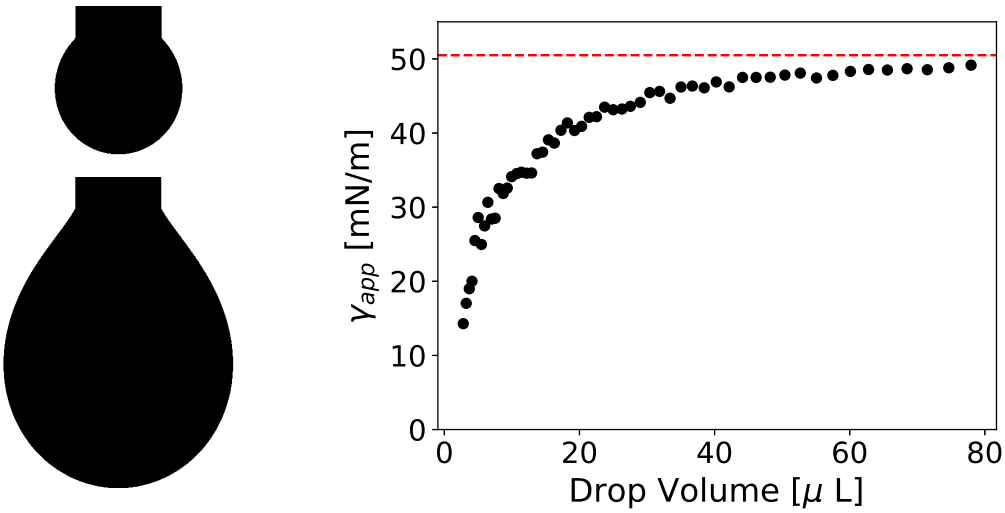

Figure 2.4 *Simulated drop images of volumes $V = 10$ μL and $V = 70$ μL, and apparent interfacial tension γ_{app} vs. drop volume V for a known interfacial tension of* 50.5 *mN/m (indicated by the dashed red line) and a needle width of 1.83 mm.*

It is clear that γ_{app} deviates further from the true value as the drop shrinks - there is an artificial dependance of γ_{app} on drop volume and area. The largest possible stable drop volume is approximately $V_{max} = 120$ μL, so it might seem that we have room to increase the drop volume from $V = 55$ μL. However, because the interfacial tension drops as particles adsorb, we need a smaller volume to maintain a safe distance from instability.

In principle, one could adjust the drop volume as the interfacial tension varies to minimise this instrument error. But we considered this too disruptive to our measurements; adjustments to the volume introduce additional interfacial strain and another timescale.

We now move on to the additional considerations required in the oscillating drop case. Following on from our discussion above and equation 2.6, it is clear that if the apparent interfacial tension has an artificial dependence on volume it must have an artificial dependance on area. Thus, we will observe an apparent dilational modulus E_{app}. To estimate the magnitude of this, we smoothed the simulated drop data shown in figure 2.4 (using [9]) and calculated the dilational modulus using equation 2.6. The resulting E_{app} is shown in figure 2.5. Even at our drop volume of 55 μL, the apparent dilational modulus is around 5 mN/m.

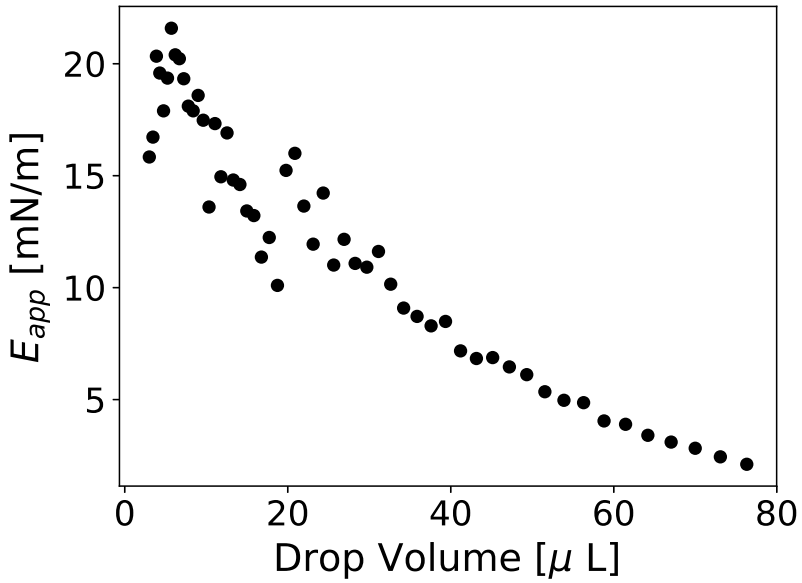

Figure 2.5 *Apparent dilational modulus E_{app} for simulated drop profiles as a function of drop volume V.*

This could explain the non-zero E' we reported in section 2.4.2.

Another key assumption we must discuss is of linearity: it has been noted that particle laden interfaces often display non-linear behaviour [10], and van Kempen *et al.* recommend that an investigation of the amplitude response be part of any rheological study of complex interfaces [11]. It is therefore prudent to check that we are measuring in the linear regime. Bykov *et al.* recently reviewed the available models for quantifying and characterising non-linear behaviour. One method of quantifying the linearity is by the total harmonic distortion or THD [12, 13]:

$$\text{THD} = \frac{(a_2^2 + a_3^2 + \cdots + a_N^2)^{1/2}}{a_1} \tag{2.16}$$

where a_1 is the amplitude of the Fourier component at the fundamental frequency and the a_n $(2 \leq n \leq N)$ are the amplitudes of higher harmonics. The fundamental frequency ω_0 is set by the applied volume oscillation. Strong linearity yields THD$\approx$0, while higher values indicate non-linearity.

We also note that while the volume is oscillated sinusoidally there is not a general linear relationship between volume and area, so we may not be applying linear area oscillations in practice. So there are in fact two linearity conditions we should test. In table 2.1 we report the THD for a number of measurements in a typical experiment which we describe fully in chapter 5. The mean THDs are comparable to the values obtained by Loglio *et al.*, with the exception of a particularly large

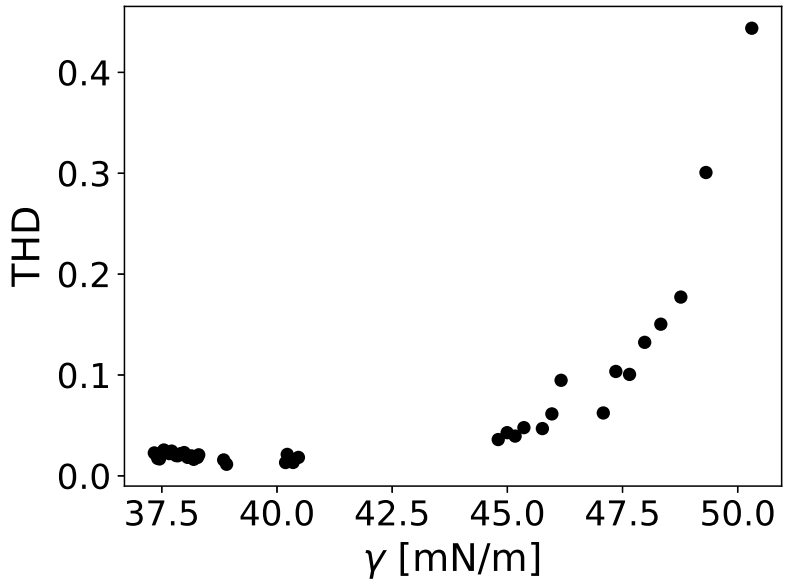

Figure 2.6 *Total Harmonic Distortion (THD) as a function of the average measured interfacial tension γ for a typical pendant drop experiment.*

maximum THD for the $\gamma(t)$ data.

Quantity	Mean THD	THD Std. Dev.	Maximum THD
$A(t)$	2.5 %	0.7 %	4.1 %
$\gamma(t)$	5.6 %	8 %	44 %

Table 2.1 *Total Harmonic Distortion (THD) for area $A(t)$ and interfacial tension $\gamma(t)$ for a typical oscillating drop experiment consisting of 43 videos ranging over interfacial tensions from $\gamma = 50$ mN/m to $\gamma = 37$ mN/m. Harmonics up to the tenth are considered in the calculation.*

Plotting THD against γ in figure 2.6 reveals that the large THD values occur at high γ where few particles are adsorbed. This is because the magnitude of γ oscillation, $\Delta\gamma$ defined in equation 2.8, becomes drowned out by noise as the interface tends towards a pure water-oil case. When γ is reduced by particle adsorption, the THD is low. This tells us that the interfacial rheology is linear when significant numbers of particles are adsorbed.

As well as linearity we must also consider that bulk flow effects - inertial and viscous forces - may distort the shape during oscillation. The strength of these

effects may be indicated by the Weber and Capillary numbers respectively [14].

$$\mathrm{We} = \frac{\text{inertial forces}}{\text{capillary forces}} = \frac{\Delta\rho\omega^2(\Delta V)^2}{\gamma a^3} \tag{2.17}$$

$$\mathrm{Ca} = \frac{\text{viscous forces}}{\text{capillary forces}} = \frac{\Delta\mu\omega\Delta V}{\gamma a^2} \tag{2.18}$$

Where $\Delta\rho$ is the difference in densities between the fluid phases, $\Delta\mu$ is the difference in Newtonian viscosities, ω is the frequency of oscillation, ΔV is the amplitude of volume oscillation, a is the radius of the needle, and γ is the dynamic interfacial tension. From the above equations it is clear that we can lessen the influence of bulk flow effects by reducing the amplitude and frequency of oscillation. In our case we find $\mathrm{We} = 3 \times 10^{-7}$ and $\mathrm{Ca} = 7 \times 10^{-7}$, so we do not expect bulk flow effects to matter. We can also approach the question of whether bulk effects are important by using the interfacial rheology. Erk *et al.* define the ratio of interfacial to bulk stresses by the Boussinesq number [15]

$$\mathrm{Bq} = \frac{\nu_d}{\nu L} \tag{2.19}$$

for dilational viscosity ν_d, bulk viscosity ν and system lengthscale L. In our system the dilational elasticity is dominant and the dilational viscosity is small, so we instead consider the interfacial stresses arising from elasticity and find the Boussinesq number by

$$\mathrm{Bq} = \frac{E'}{\omega\nu L}. \tag{2.20}$$

Even for a small dilational elasticity $E' = 1$ mN/m, we find $\mathrm{Bq} > 10^3$ for $L = 1$ mm, and taking dodecane's viscosity to be $\nu = 1.34$ mPa s at an oscillation frequency of 0.1 Hz. This agrees with the previous approach and verifies that the interfacial stresses outweigh the bulk stresses, suggesting that interfacial rheological measurements are feasible.

In summary, we have introduced the technique of pendant drop tensiometry, described the preparation of a colloid-laden pendant drop, detailed our application of the technique to such a drop, and verified those measurements. Specifically, we showed that 1) we are reasonably free of surface active contamination, 2) we have chosen an appropriate drop volume, 3) we do apply a sinusoidal area oscillation which yields a linear interfacial tension response, and 4) that bulk flow effects are likely insignificant.

2.5 Langmuir-Pockels Trough

This section describes the use of a Langmuir-Pockels trough and Wilhelmy plate to measure the mechanical properties of an interface. We will first introduce the technique in section 2.5.1, then detail our application of it in section 2.5.2. Finally, in section 2.5.3 we will discuss its limitations.

2.5.1 Langmuir-Pockels Trough Background

A Langmuir-Pockels trough is a large trough with moveable barriers which allow fluid to flow past those barriers while not allowing the fluid interface to move past the barriers - thus compressing the interface between the barriers. It is often used with a Wilhelmy plate, which allows the interfacial tension to be measured during compression i.e. in a strain controlled experiment.

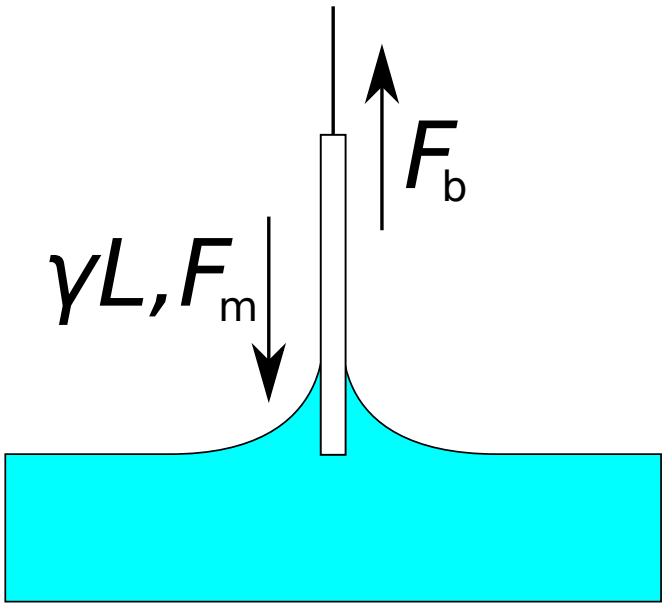

Figure 2.7 *Schematic of a Wilhelmy plate at a water-air interface, showing the downwards forces due to interfacial tension (γL) and the plate weight (F_m) opposed to the buoyant force F_b. The sum of these forces gives the force measured by the balance. Plate support tension is not shown.*

The Wilhelmy plate is a thin plate which becomes wet by the fluid in the trough and therefore feels a force towards the interface, as shown in figure 2.7. If the plate is perfectly wet so that the contact angle θ is zero and its base is level with the liquid interface, then the force F on the plate follows $F = \gamma L + F_m - F_b$ where L is the wetted perimeter of the plate. F_m and F_b are the weight of the

plate and buoyant force respectively, which are constant if the plate is fixed in position. The interfacial tension γ is then found from

$$\gamma = \frac{F - F_m + F_b}{L}. \tag{2.21}$$

Usually, the surface pressure is measured rather than the interfacial tension as we only need to set this to zero at the beginning of the experiment. If the plate is partially submerged in two fluids - oil and water for example - such that it protrudes through both the water/oil and water/air interfaces, we can still measure interfacial properties but now the expression for the water/oil interfacial tension γ_{wo} becomes

$$\gamma_{wo} = \frac{F - F_m + F_b'}{L} - \gamma_{oa}\cos(\theta_{oa}). \tag{2.22}$$

with γ_{oa} and θ_{oa} the oil-air tension and contact angle respectively, and F_b' includes the effect of displaced oil. We can again measure only the surface pressure to eliminate constant terms, but this assumes a constant γ_{oa}.

2.5.2 Langmuir-Pockels Trough Measurements

For the Langmuir-Pockels trough measurements we used a poly-tetrafluorethylene (PTFE) trough with a quartz glass window to allow imaging of the interface, a custom aluminium insert, and PTFE barriers - as shown in figure 2.8. The trough allows an interfacial area of dimensions 31.5 cm $\times$ 5.4 cm. The Wilhelmy plate used was a 10.3 mm width filter paper plate soaked in the subphase liquid for 20 minutes prior to use to dissolve contaminants. The plate was kept perpendicular to the barriers for all measurements, though we lacked precise control over the angle between the plate and the barriers and judged whether it was perpendicular by eye. Surface pressure measurements were made and recorded by a balance (KSV mini-trough, KSV Instruments Ltd., Finland) which was calibrated by a known mass.

The trough was first filled with water, and the cleanliness of the interface was tested by compression at 100 mm/min until the barrier meniscus began to interfere with the measurement. If the surface pressure rose by less than 0.1 mN/m over this range the interface was considered clean and purified dodecane would be added, otherwise the trough was cleaned by aspirating the interface, or rinsed with ethanol and dried before repeating the measurement. After oil addition, the surface pressure was recorded as a function of time for 20 minutes, and the interface was subjected to compression-expansion cycles at a barrier

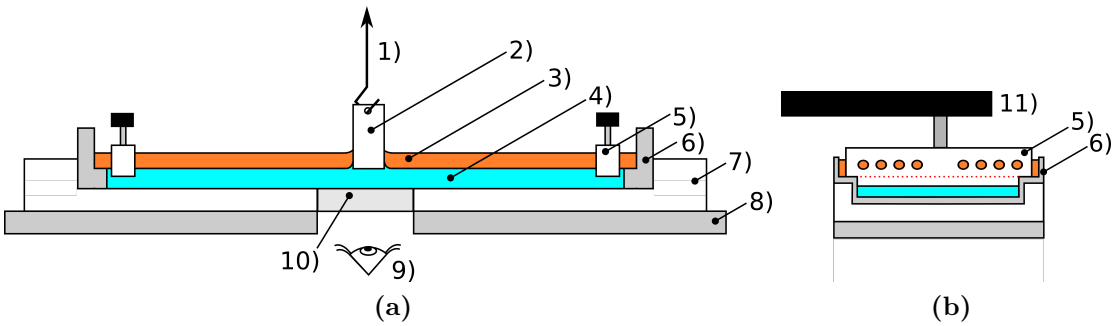

Figure 2.8 *Cross-sections of Langmuir-Pockels trough apparatus. 1) Hook connecting Wilhelmy plate to a balance, 2) Wilhelmy plate, 3) oil phase, 4) water phase, 5) trough barrier, 6) custom aluminium insert, 7) PTFE trough, 8) aluminium base, 9) imaging apparatus, 10) quartz glass window, 11) computer controlled barrier arm which moves the trough barrier. The dashed red line indicates where the fluid interface meets the barrier.*

speed of 100 mm/min. The oil-water interface was not cleaned, and typically showed a small increase at high compressions, as shown in figure 2.9. The surface pressure of the bare interface in compression shows a minimum of -0.29 mN/m, a maximum of 0.21 mN/m, an average of 0.00 mN/m and a standard deviation of 0.06 mN/m.

Particles would then be added to the interface by pipetting a particles-in-dodecane dispersion of volume fraction $\phi = 0.2\,\%$ near the interface. The volume added was chosen such that the particles were expected to occupy 130 cm^2 of the available 170 cm^2, corresponding to an area fraction below that of random or ordered close packing, except for $r = 193$ nm particles where ca. 740 cm^2 of particle area was added. This was necessary to observe a surface pressure response after the given waiting period. A waiting period of one hour was allowed, during which time images were recorded. The interface was then compressed and expanded at a constant barrier speed of 5 mm/min while imaging. The surface pressure was measured relative to the bare water-dodecane interface just after addition.

2.5.3 Langmuir-Pockels Trough Discussion

Now that we have described our measurement procedure, we can discuss its limitations and calibration. While the experiment is strain-controlled, the strain applied in the rectangular trough we described is actually a mixture of the dilational and shear modes we explained in chapter 1. This results in a combination of dilational and shear responses. If the shear response is significant, the interfacial stress can become anisotropic. An anisotropic interfacial stress

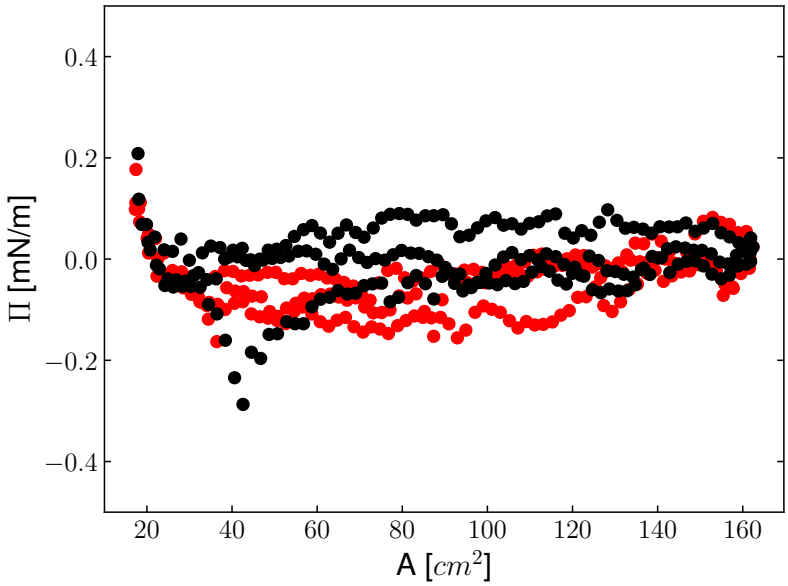

Figure 2.9 *Typical surface pressure data for a bare water-dodecane interface under compression (black) and expansion (red) in a Langmuir-Pockels trough.*

means that the measured surface pressure will depend on the orientation of the Wilhelmy plate. As Aveyard *et al.* and Kumaki have noted, the surface pressure seems to become anisotropic for smaller particles (less than 1 μm radius) [16, 17]. There are two solutions to this issue. One can apply a purely dilational strain, e.g. by using a radial trough [18]. Alternatively, one can take advantage of the mixed mode deformation and use two perpendicular Wilhelmy plates to capture all of the information and extract the dilational and shear responses [19, 20]. Unfortunately we are limited to one plate and cannot tell whether the shear response is significant.

A difficulty which is particular to colloidal particles is that their granular nature may cause the stress distribution to become non-uniform throughout the monolayer [21]. This so-called Janssen effect was observed for relatively large particles (100 μm) by comparing the surface pressure at the onset of buckling for various particle loadings, with care taken to measure the surface pressure in two perpendicular directions. Finally, in contrast with oscillating pendant drop tensiometry the strain applied in a Langmuir-Pockels trough is typically quite large. For example, in our apparatus the maximum Cauchy strain is around 80%. It is questionable whether the linear treatment we discussed in chapter 1 applies at this point, so measurements of material functions such as E from such experiments should be viewed critically.

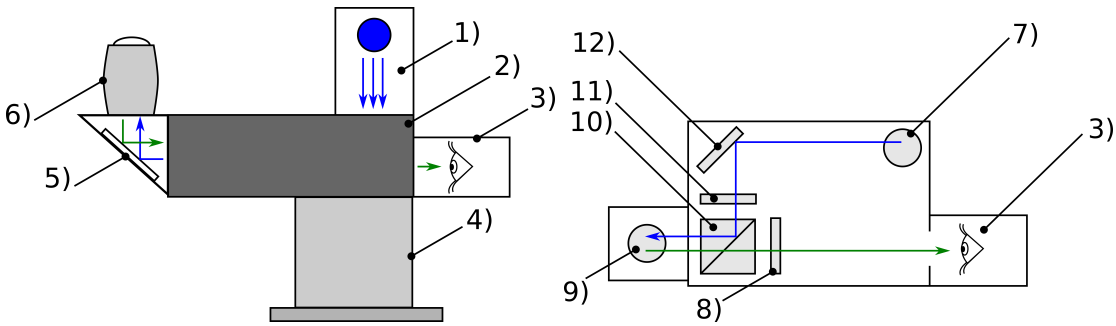

(a) *Side view* **(b)** *Top view*

Figure 2.10 *Cross-sections of imaging apparatus. 1) LED Light source, 2) module body, 3) camera, 4) xyz stage, 5) mirror, 6) objective lens, 7) mirror, 8) tube lens, 9) mirror, 10) filter cube, 11) collimating lens, 12) mirror. Blue arrows indicate the path of excitation light and green arrows show the path of the fluorescence light.*

2.6 Imaging the Interface

This section introduces fluorescent microscopy, explains how we use it for our system, and discusses its limitations. In light microscopy, a broad range of wavelengths are captured by the objective lens. Fluorescent microscopy uses the presence of fluorescent dyes - fluorophores - in the sample. These fluorophores absorb specific wavelengths λ_{ex} of light and emit different specific wavelengths λ_{em}. By using chromatic filters only light emitted from those fluorophores is captured by the objective. This improves the contrast of the image and specifically records the dyed parts of the sample.

As noted in section 2.3 our colloidal particles incorporate the fluorescent monomer NBD-MMA into their structure. Using the custom-built imaging module shown in figure 2.10, we illuminated the sample with a CoolLED precisExcite operating at 470 nm with various illumination strengths, captured the fluorescent emission and reflected excitation light with a Nikon, 20×, plan fluor, numerical aperture (NA)=0.45 objective lens, filtered out the excitation light with a Semrock GFP-30LP-B_NQF filter cube, and recorded this light on a CCD camera (Manta G-033B, Allied Vision Technologies) controlled by custom LabView software. Image processing and analysis are described later in chapter 3.

As in light microscopy, fluorescence microscopy is fundamentally diffraction limited. The point spread function (PSF) of an imaging system describes its response to a point source of light, or to put it another way the PSF describes how much the imaging system blurs a point source. This blurring can obscure small features (e.g. individual particles) from being resolved. Microscopes, for

example, can only resolve particle separations d larger than the Abbe diffraction limit for light of wavelength λ, where d satisfies

$$d = \frac{\lambda}{2\mathrm{NA}}. \tag{2.23}$$

For our system ($\lambda_{\mathrm{em}} = 530$ nm, NA $= 0.45$) this results in $d = 0.59$ μm, so we expect difficulties imaging particles smaller than this in diameter, as particles approach each other.

2.7 Particle Characterisation

In this section we report and discuss the characterisation of our particles in two key aspects: radius r and contact angle θ. We assess particle size by static light scattering (SLS) and dynamic light scattering (DLS). We measure the contact angle by a recently developed spectroscopic technique [22].

2.7.1 Dynamic Light Scattering

In dynamic light scattering, a laser is shone onto a sample of particles and the scattered light from those particles is measured from a particular angle as a function of time. Over time, particles are moved around by thermal fluctuations and the scattering intensity changes. How quickly this change occurs depends on the particle diffusion, which depends on particle size. The change over time is captured by measuring the autocorrelation of the scattered intensity (of a small number of speckles) at a fixed observation angle. To calculate the particle size, we must know the temperature T and the solvent viscosity η. Further details may be found in [23]. A key consideration is that the DLS size is a hydrodynamic size - it is an effective size which depends on the drag on each particle - which is likely to be larger than the actual particle. Particle radii measured by DLS are therefore expected to be larger than SLS reports.

We prepared a sample of colloidal dispersion from a stock solution with a volume fraction of 0.2 % which was sonicated for one hour at 45kHz to re-disperse the particles before dilution with n-dodecane to a volume fraction of 0.001% for ASM449, 0.0001% for ASM613, and 0.004 % for ASM530 to achieve a suitable scattered intensity for the detector. The autocorrelation of the scattering intensity was recorded using an ALV CGS-3 Goniometer and ALV/LSE-5004 correlator controlled by a PC with ALV software. The light source was a JDSU 1145P He-Ne laser of wavelength 632.8 nm, and the temperature was regulated

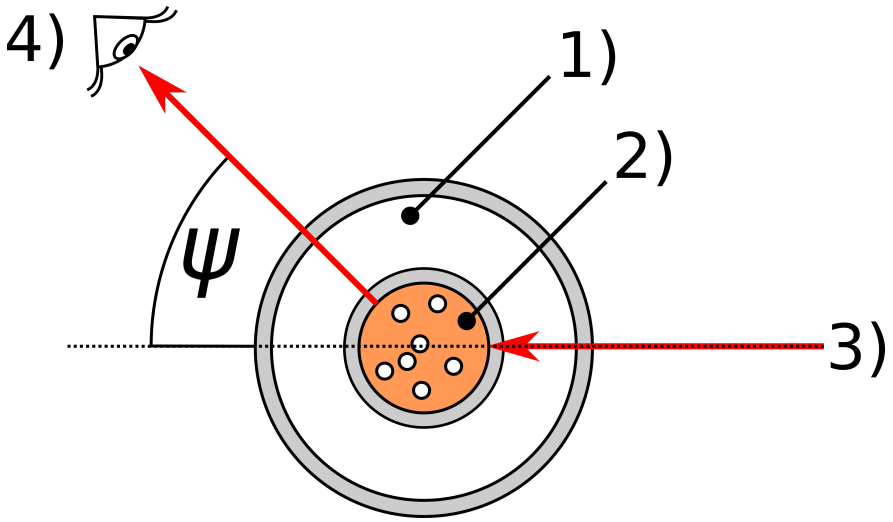

Figure 2.11 *Schematic of DLS/SLS apparatus. 1) Thermostated toluene bath, 2) Colloidal dispersion, 3) Laser light, 4) Scattered light received by detector at an angle of ψ.*

with a Haake K20 and DC1 circulating bath and temperature control. We took the solvent viscosity to be $\eta = 1.34$ mPa s [24] and controlled the temperature to 297.56 K. A schematic of the apparatus is shown in figure 2.11.
The autocorrelation of the scattered light was fitted with a series of exponential decays for each size to calculate the intensity distribution across decay times. This was then expressed as a histogram of particle sizes by accounting for the variation of scattered intensity with particle size: the scattering intensity from a particle of radius r is proportional to r^6. These results are shown in figure 2.12 and summarised in table 2.2.

2.7.2 Static Light Scattering

In static light scattering (SLS) as in DLS we also observe the scattered light from a sample of disperse particles. However we now observe the scattered light (from many speckles) as a function of angle to gain information about the scatterers. Because we cannot uniquely extract the properties of the particles from the scattering function, we must assume that they scatter in a similar way to a particular model. In our case, Mie scattering is the most appropriate since the particle size is comparable to the wavelength of the light $\lambda = 632.8$ nm. In this model, we need to know the particle refractive index n_p, the solvent refractive index n_s, and the laser wavelength λ. The colloid concentration ought also to be low enough to avoid multiple scattering. Further information is available in [25]. SLS measurements were carried out using the same apparatus described in section

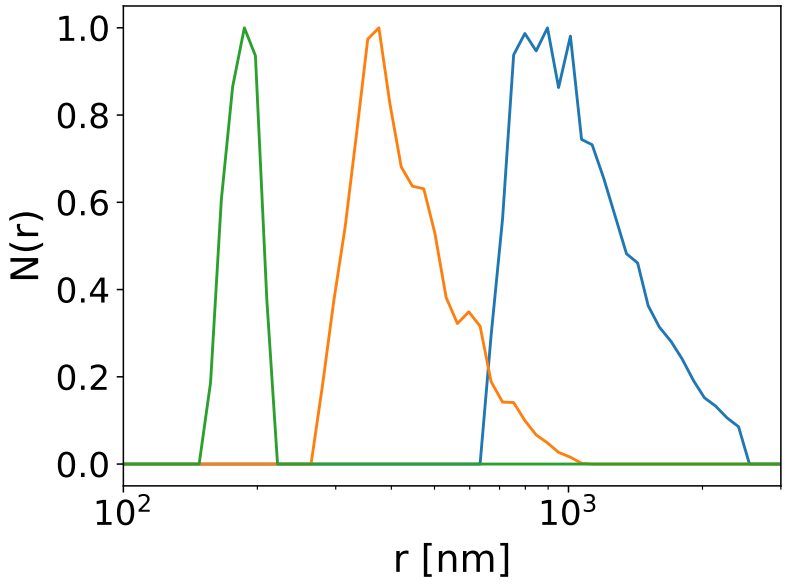

Figure 2.12 *Particle size distributions for ASM449 (blue), ASM613 (orange), and ASM530 (green) measured by dynamic light scattering. Distributions are normalised by the peak value.*

2.7.1, but the scattering was recorded for every 2° from 30° to 150°. We used sample volume fractions of 0.0002 % for ASM449, 0.0001 % for ASM613, and 0.004% for ASM530 to achieve a suitable scattered intensity. With temperature again at 297.56 K we took the refractive index of the solvent to be $n_s = 1.4197$ [26, 27] and of the particle $n_p = 1.5$ [28]. The logarithmic intensity was plotted as a function of scattering vector magnitude $q = \frac{4\pi n_s}{\lambda} \sin(\psi/2)$ with scattering angle ψ as shown in figure 2.11. These measurements were then fitted with a Mie scattering function generated from assuming particles of radius r_M and a polydispersity of p_M: the r_M and p_M were varied until the model data was judged by eye to fit the measurements. The resulting fits are shown with the accompanying data in figure 2.13.

Both techniques show that we have three quite different sizes of particles, as required. DLS sizes are slightly smaller than SLS sizes, which is surprising. Because DLS is based on the hydrodynamic size of the particle which is affected by its steric hairs, we expect the DLS sizes to be systematically larger than the scattering based SLS method where scattering occurs mainly from the polymer core rather than the steric hairs. The length of the steric hairs has been reported as 13-19 nm [29] in a decalin solvent, with possible variation in practice due to variation in the grafting density of the hairs. Nevertheless the SLS and DLS results for each batch are largely in agreement and the differences between batches

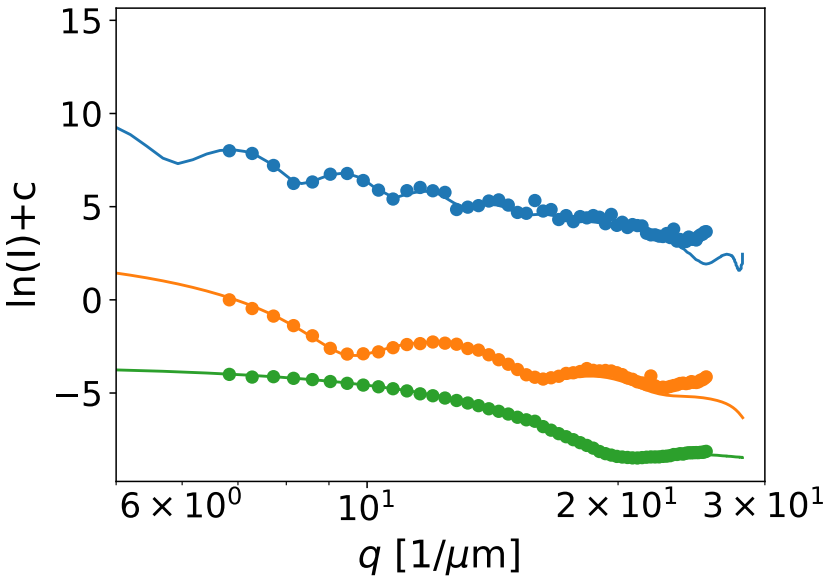

Figure 2.13 *Static light scattering data (points) and fits (lines) for three particle sizes (blue: ASM449, orange: ASM613, green: ASM530) with arbitrary shifts applied to the logarithm of the intensity of each to better display them as a function of scattering vector magnitude.*

Particle Batch	Particle Size [nm]		Polydispersity
	DLS	SLS	SLS
ASM449	1120 ± 60	1260 ± 10	5%
ASM613	440 ± 10	450 ± 5	9%
ASM530	187 ± 4	193 ± 3	12%

Table 2.2 *Particle size measured by dynamic light scattering (DLS) and static light scattering (SLS).*

are significantly larger than the measurements errors.

2.7.3 Contact Angle Measurements

The measurement of particle contact angles has attracted a fair amount of interest in recent years given its importance for interfacial behaviour. Various methods ranging from fluid uptake methods to scanning angle reflectrometry were recently reviewed by Zanini and Isa [30].

We use a recently developed spectroscopic method developed by Horváth *et al.* to measure the microscopic contact angle in situ [22]. This technique relies on the particle's refractive index difference with the medium. Particles trapped at a fluid interface are partially immersed in two phases with different refractive indices. This difference allows the immersion depth δ_D to be characterised by the shift in the wavelength of a feature in the spectrum of the particle dispersion when the particles adsorb to the interface.

Two measurements are required: one with the particles dispersed in a homogeneous medium and the other with the particles forming a monolayer on the interface between media 1 and 2. For each case the transmission $\alpha(\lambda)$ is calculated from the recorded intensities $S(\lambda)$, $R(\lambda)$ and $D(\lambda)$ - the system with particle, the system without particles, and the dark count respectively:

$$\alpha(\lambda) = \frac{S(\lambda) - D(\lambda)}{R(\lambda) - D(\lambda)}. \tag{2.24}$$

These transmission spectra allow us to identify a feature which occurs at λ_{hm} in the homogeneous medium and λ_i for the interface. Then δ_D can be calculated by

$$\delta_D = \frac{\frac{\lambda_i}{\lambda_{\mathrm{hm}}}\left(n_p^{(\lambda_{\mathrm{hm}})} - n_{\mathrm{hm}}^{(\lambda_{\mathrm{hm}})}\right) - \left(n_p^{(\lambda_i)} - n_1^{(\lambda_i)}\right)}{\left(n_1^{(\lambda_i)} - n_2^{(\lambda_i)}\right)}. \tag{2.25}$$

From which one can simply use geometry to calculate the contact angle by

$$\theta = \cos^{-1}\left(2\delta_D - 1\right). \tag{2.26}$$

In the above, $n_p^{(\lambda)}$, $n_{\mathrm{hm}}^{(\lambda)}$, $n_1^{(\lambda)}$ and $n_2^{(\lambda)}$ are the refractive indices of the particle, the homogeneous medium mentioned above, and media 1 and 2 respectively at the wavelength λ.

To carry out this experiment, we first measure the transmission spectrum $R_{bulk}(\lambda)$ of n-dodecane without particles as a reference. We are using n-dodecane both as the homogeneous medium and medium 1, so $n_{\mathrm{hm}} = n_1$. We can then measure

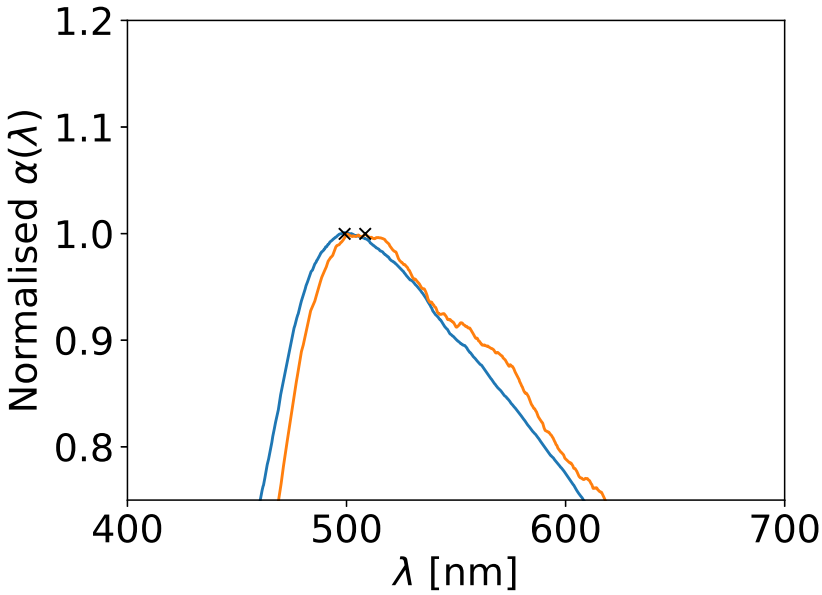

Figure 2.14 *Example transmission spectra for ASM449 in bulk (blue) and at the interface (orange).*

the spectrum $S_{bulk}(\lambda)$ of particles dispersed in oil to a volume fraction of 0.001 %. Using equation 2.24, we can then find $\alpha_{\text{bulk}}(\lambda)$ and identify a feature at λ_{hm}. With a known feature at λ_{hm}, we perform a similar process - recording the spectrum of a bare interface $R_{int}(\lambda)$ and monolayer of particles $S_{int}(\lambda)$, then calculating $\alpha_{\text{int}}(\lambda)$. The monolayer is prepared by allowing sedimentation from 3mL of colloidal dispersion with a volume fraction $\mathcal{O}(0.01)$ %. The interfacial $\alpha_{\text{int}}(\lambda)$ shows the same feature shifted to λ_i. Example bulk and interfacial $\alpha(\lambda)$ for ASM449 are shown in figure 2.14, where we can see a clear shift in the wavelength of the feature.

From the identified λ_{hm} and λ_i, and the known refractive indices at each wavelength we find the contact angles given in table 2.3. We find the refractive indices at each wavelength using tabulated values for water [31] and for *n*-dodecane the empirical formula

$$n^{(\lambda)}_{\text{dodecane}} = 1.41336 + \frac{2349.37\text{nm}^2}{\lambda^2} + \frac{193451000\ \text{nm}^4}{\lambda^4} \tag{2.27}$$

which is derived by using refractive index data from Yahya *et al.* [32] to calculate the coefficients of the Cauchy equation up to λ^{-4} [33].

The literature values for the contact angle of PHSA-PMMA particles were recently summarised by Van Hooghten *et al.* [34]. At the water-dodecane interface Thijssen *et al.* found $\theta = 160.3 \pm 0.4°$ from the contact angle of

Particle Batch	Contact Angle [°]
ASM449	164.8±1.7
ASM613	-
ASM530	-

Table 2.3 *Particle contact angles for three different batches. We could not reliably measure contact angles for ASM613 and ASM530.*

a macroscopic water drop on a PHSA-PMMA substrate under dodecane. At the water-decane interface, which we expect to be comparable, Isa *et al.* found $\theta = 157.3 \pm 6.6°$ by a gel-trapping technique and $\theta = 129.8 \pm 11.8°$ by a freeze-fracture method [34, 35]. In light of these values, our measured $\theta = 164.8 \pm 1.7°$ is not unreasonable.

We might expect some practical differences in the contact angles of different particle sizes to emerge because of the dynamics of binding, and the inherent variations arising during synthesis. There is a sudden breach of the interface as the particle adsorbs, but equilibrium can take a long time to be achieved due to the local pinning of the contact line [36]. Larger particles have a larger adsorption energy and a larger contact line, but the adsorption energy scales with particle radius r^2 while the contact line length scales with r. Thus we expect smaller particles to have larger contact angles if dynamic effects are important.

2.8 Conclusion

We described the interfacial rheology techniques - pendant drop tensiometry and the Langmuir-Pockels trough - which we will use in later chapters, and discussed their merits and shortcomings. We described our imaging apparatus and its limitations, and reported our characterisation of three batches of colloidal particles by their size and contact angles. We found that we have three different sizes of colloid - radii $r \approx 1090$ nm, $r \approx 440$ nm, and $r \approx 190$ nm - that we can use to explore the effect of size variation. For our largest particle size, we found the contact angle to be $\theta = 164.8 \pm 1.7°$, which compares favourably with the literature.

Bibliography

[1] Roger S. Jardine and Paul Bartlett. Synthesis of non-aqueous fluorescent hard-sphere polymer colloids. *Colloids and Surfaces A: Physicochemical and Engineering Aspects*, 211(2-3):127–132, 2002.

[2] Wilson CK Poon, Eric R Weeks, and C Patrick Royall. On measuring colloidal volume fractions. *Soft Matter*, 8(1):21–30, 2012.

[3] A Goebel and Klaus Lunkenheimer. Interfacial tension of the water/n-alkane interface. *Langmuir*, 13(2):369–372, 1997.

[4] Joseph D Berry, Michael J Neeson, Raymond R Dagastine, Derek YC Chan, and Rico F Tabor. Measurement of surface and interfacial tension using pendant drop tensiometry. *Journal of colloid and interface science*, 454:226–237, 2015.

[5] Mohsen Sharifi, Mahmood Fathy, and Maryam Tayefeh Mahmoudi. A classified and comparative study of edge detection algorithms. In *Information Technology: Coding and Computing, 2002. Proceedings. International Conference on*, pages 117–120. IEEE, 2002.

[6] NB Vargaftik, BN Volkov, and LD Voljak. International tables of the surface tension of water. *Journal of Physical and Chemical Reference Data*, 12(3):817–820, 1983.

[7] Susana Zeppieri, Jhosgre Rodríguez, and AL López de Ramos. Interfacial tension of alkane+ water systems. *Journal of Chemical & Engineering Data*, 46(5):1086–1088, 2001.

[8] Sebastian Knoche, Dominic Vella, Elodie Aumaitre, Patrick Degen, Heinz Rehage, Pietro Cicuta, and Jan Kierfeld. Elastometry of deflated capsules: Elastic moduli from shape and wrinkle analysis. *Langmuir*, 29(40):12463–12471, 2013.

[9] Scipy v0.16.1 reference guide. `https://docs.scipy.org/doc/scipy-0.16.1/reference/generated/scipy.signal.savgol_filter.html`. Accessed: 2019-01-23.

[10] Valeria Garbin, John C. Crocker, and Kathleen J. Stebe. Nanoparticles at fluid interfaces: Exploiting capping ligands to control adsorption, stability and dynamics. *Journal of Colloid and Interface Science*, 387(1):1–11, 2012.

[11] Silvia EHJ van Kempen, Henk A Schols, Erik van der Linden, and Leonard MC Sagis. Non-linear surface dilatational rheology as a tool for understanding microstructures of air/water interfaces stabilized by oligofructose fatty acid esters. *Soft Matter*, 9(40):9579–9592, 2013.

[12] AG Bykov, L Liggieri, BA Noskov, P Pandolfini, F Ravera, and G Loglio. Surface dilational rheological properties in the nonlinear domain. *Advances in colloid and interface science*, 222:110–118, 2015.

[13] Giuseppe Loglio, Piero Pandolfini, Reinhard Miller, Alexander V Makievski, Jürgen Krägel, Francesca Ravera, and Boris A Noskov. Perturbation–response relationship in liquid interfacial systems: non-linearity assessment by frequency–domain analysis. *Colloids and Surfaces A: Physicochemical and Engineering Aspects*, 261(1-3):57–63, 2005.

[14] EM Freer, H Wong, and CJ Radke. Oscillating drop/bubble tensiometry: effect of viscous forces on the measurement of interfacial tension. *Journal of colloid and interface science*, 282(1):128–132, 2005.

[15] Kendra A Erk, Jeffrey D Martin, Jonathan T Schwalbe, Frederick R Phelan Jr, and Steven D Hudson. Shear and dilational interfacial rheology of surfactant-stabilized droplets. *Journal of colloid and interface science*, 377(1):442–449, 2012.

[16] Robert Aveyard, John H Clint, Dieter Nees, and Nick Quirke. Structure and collapse of particle monolayers under lateral pressure at the octane/aqueous surfactant solution interface. *Langmuir*, 16(23):8820–8828, 2000.

[17] Jiro Kumaki. Monolayer of polystyrene monomolecular particles on a water surface studied by langmuir-type film balance and transmission electron microscopy. *Macromolecules*, 21(3):749–755, 1988.

[18] Martina Pepicelli, Tom Verwijlen, Theo A Tervoort, and Jan Vermant. Characterization and modelling of langmuir interfaces with finite elasticity. *Soft matter*, 13(35):5977–5990, 2017.

[19] Jordan T Petkov, Theodor D Gurkov, Bruce E Campbell, and Rajendra P Borwankar. Dilatational and shear elasticity of gel-like protein layers on air/water interface. *Langmuir*, 16(8):3703–3711, 2000.

[20] P Cicuta and EM Terentjev. Viscoelasticity of a protein monolayer from anisotropic surface pressure measurements. *The European Physical Journal E*, 16(2):147–158, 2005.

[21] Pietro Cicuta and Dominic Vella. Granular character of particle rafts. *Physical review letters*, 102(13):138302, 2009.

[22] Imre T Horváth, Pierre Colinet, and Maria Rosaria Vetrano. Measuring contact angles of small spherical particles at planar fluid interfaces by light extinction. *Applied Physics Letters*, 108(20):201605, 2016.

[23] Clemens Bechinger, Francesco Sciortino, and Primoz Ziherl. *Physics of complex colloids*, volume 184. IOS Press, 2013.

[24] DR Caudwell, JPM Trusler, V Vesovic, and WA Wakeham. The viscosity and density of n-dodecane and n-octadecane at pressures up to 200 mpa and temperatures up to 473 k. *International Journal of Thermophysics*, 25(5):1339–1352, 2004.

[25] Thomas Zemb and Peter Lindner. *Neutrons, X-rays and light: scattering methods applied to soft condensed matter*. North-Holland, 2002.

[26] Tejraj M Aminabhavi and Bindu Gopalakrishna. Density, viscosity, refractive index, and speed of sound in binary mixtures of 2-ethoxyethanol with n-alkanes (c6 to c12), 2, 2, 4-trimethylpentane, and cyclohexane in the temperature interval 298.15-313.15 k. *Journal of Chemical and Engineering Data*, 40(3):632–641, 1995.

[27] MD Lechner. *Refractive indices of pure liquids and binary liquid mixtures (supplement to III/38)*. Springer, 2008.

[28] Guy Beadie, Michael Brindza, Richard A Flynn, A Rosenberg, and James S Shirk. Refractive index measurements of poly (methyl methacrylate)(pmma) from 0.4–1.6 μm. *Applied optics*, 54(31):F139–F143, 2015.

[29] AL Washington, Xin Li, AB Schofield, Kunlun Hong, MR Fitzsimmons, Robert Dalgliesh, and Roger Pynn. Inter-particle correlations in a hard-sphere colloidal suspension with polymer additives investigated by spin echo small angle neutron scattering (sesans). *Soft Matter*, 10(17):3016–3026, 2014.

[30] Michele Zanini and Lucio Isa. Particle contact angles at fluid interfaces: pushing the boundary beyond hard uniform spherical colloids. *Journal of Physics: Condensed Matter*, 28(31):313002, 2016.

[31] George M Hale and Marvin R Querry. Optical constants of water in the 200-nm to 200-μm wavelength region. *Applied optics*, 12(3):555–563, 1973.

[32] Mohammed Yahya and M Ziad Saghir. Prediction and experimental measurement of refractive index in ternary hydrocarbon mixtures. *Journal of Chemical & Engineering Data*, 60(8):2329–2342, 2015.

[33] FA Jenkins and HE White. *Fundamentals of Optics, 4th edition*. McGraw-Hill Inc., 1981.

[34] Rob Van Hooghten, Victoria E Blair, Anja Vananroye, Andrew B Schofield, Jan Vermant, and Job HJ Thijssen. Interfacial rheology of sterically stabilized colloids at liquid interfaces and its effect on the stability of pickering emulsions. *Langmuir*, 33(17):4107–4118, 2017.

[35] Lucio Isa, Falk Lucas, Roger Wepf, and Erik Reimhult. Measuring single-nanoparticle wetting properties by freeze-fracture shadow-casting cryo-scanning electron microscopy. *Nature communications*, 2:438, 2011.

[36] David M Kaz, Ryan McGorty, Madhav Mani, Michael P Brenner, and Vinothan N Manoharan. Physical ageing of the contact line on colloidal particles at liquid interfaces. *Nature materials*, 11(2):138, 2012.

Chapter 3

Structural Characterisation of Particle-Laden Liquid Interfaces

3.1 Abstract

In this chapter we characterise deposited colloidal layers at a flat interface for three particle sizes, in preparation for later interfacial rheology experiments. We measure the surface fraction by three image-analysis methods, and find that using the fraction of white pixels in a binarised fluorescent micrograph provides the most consistent estimate across the particle sizes and structures considered. We find that all three particle sizes present comparable densities, but also much lower densities than expected from the number of particles added, which highlights the importance of measuring the surface fraction. We also measure the cluster size distribution and find that as particle size decreases, aggregates become larger.

3.2 Introduction

To understand the interfacial rheology of particle-laden interfaces, we must consider structure. Surface materials have two key aspects: density and structure. We first discuss density, and then the interfacial structure.

Despite the known importance of particle surface density for rheological properties it is not yet standard practice to measure it directly in interfacial rheological measurements [1, 2]. Often, surface pressure is simply reported as a function of area [3], which makes it difficult to compare the surface pressure of different systems, or even of the same system measured by different techniques.

Another common practice is to measure the surface fraction indirectly. Typically,

surface pressures are measured in a Langmuir trough during the compression of a colloidal layer where a fixed number of particles have been spread at the interface with a spreading solvent, similar to how surface pressure isotherms are captured for surfactants. Then the surface density or surface fraction is calculated using a feature of the surface pressure curve, for example by assuming that all spread particles are adsorbed [4]. This ignores the possibility that particles are prevented from adsorbing to the interface, for example by energetic barriers to adsorption [5]. Additionally, the use of spreading solvent has been demonstrated to affect the three-phase contact angle, which is a key parameter for interfacial properties [6]. We have chosen to avoid a spreading solvent and allow particles to adsorb spontaneously from the bulk oil phase above the interface, so that sedimentation drives particles to the interface and aids adsorption. This method allows us to maintain a cleaner system and more easily calibrate the interfacial tension measurement.

Alternative indirect methods exist to measure surface fraction, for example assuming that the particles are close-packed at the 'knee' in the surface pressure curve (see figure 4.1) but it is not clear that this assumption should generally hold [1, 2, 7].

In pendant drop experiments it is usual to allow particles to spontaneously adsorb to the interface without a spreading solvent, which might be expected to be simpler and more reproducible since it is driven by thermodynamics though in practice it can prove difficult [5, 8]. Pendant drop measurements can also be complicated by the influence of gravity, the difficulty of accurately measuring the interfacial tension over a range of drop areas, and the invalidity for complex interfaces of the Young-LaPlace equation used to extract the surface pressure [9–11]. Thus it is even more challenging to rely on surface pressure features to estimate surface fraction.

A number of authors have made direct measurements of the surface fraction with various techniques. For large enough particles, direct microscopy provides a simple and clear method to determine the surface fraction [12, 13]. For smaller particles, Garbin *et al.* used the optical absorbance of a pendant drop, Kutuzov *et al.* used transmission electron microscopy to image a comparable interface to the one studied, Reincke *et al.* used fluorescence microscopy and a theoretical model for particle chemical potential to calculate the surface concentration, and for a curved interface Zhang *et al.* used scanning electron microscopy after first polymerising one of the liquid phases [14–17]. These direct measurements are more time-consuming than assuming all spread particles adsorb, or that a feature

of the surface pressure corresponds to close packing of particles, but they are preferable for the sake of accuracy.

While the surface fraction is likely the most important parameter for the rheological properties of a given system, the interfacial arrangement is also important. For example Petkov *et al.* showed that aggregation could increase the surface pressure, and Razavi *et al.* observed different surface pressure responses and interfacial structure for different degrees of hydrophobization [3, 18]. Possible structures for self-assembled colloidal monolayers range from well ordered crystal-like structures to disordered aggregates [19]. Mesostructures have also been observed, but are possibly due to contamination [20].

Different approaches to structural characterisation are required depending on whether the colloidal layer is ordered or disordered. For ordered systems, the interparticle spacing is determined by the surface fraction, which we have already discussed, the lattice type, the domain size, and the distribution of defects. For disordered systems, a fractal approach is often used. Colloidal systems may display a statistical self-similarity, which can be quantified by the fractal dimension D_f, such that the mass $m(L_{frac})$ within a certain length scale L_{frac} scales as $m(L_{frac}) \propto L_{frac}^{D_f}$. This scaling will only apply down to the a cut off determined by the basic building block of the structure, which may be an individual particle or a cluster, and may not apply for high densities for example at close packing. For aggregating systems, the dynamics have been studied to characterise systems by the distribution across time and cluster sizes. For our system, we note that aggregates do not grow over the experimental timescales we have considered. Thus we only consider the cluster size distribution.

We have described the importance and measurement of two key aspects of the interfacial layer: the density of particles, and their arrangement. In this chapter we will describe our use of fluorescence microscopy to characterise the interfacial layer, and to estimate the density of particles and the distribution of interfacial cluster sizes for three sizes of sterically-stabilised particles at a flat interface. We will show that while the densities for each layer of differing particle size are comparable, there are some significant structural changes which are described by the density distribution and the cluster size distribution. This understanding of our generated monolayers will then allow us to compare rheological measurements in later chapters.

3.3 Method

In chapter 2 we described the imaging apparatus and preparation method for flat particle-laden interfaces. Here we detail how we process and analyse these images to determine the interfacial structure of the colloidal layer.

3.3.1 Surface Fraction Measurement

We used three image-analysis methods to measure the surface fraction from fluorescent microscopy images. We call these methods 'particle counting', 'white fraction' and 'Fourier lengthscale', and denote the surface fractions estimated by them ϕ_p, ϕ_w, and ϕ_F respectively. The first two are performed on binarised images, and are described below.

To estimate ϕ_p or ϕ_w we first enhanced the images by adjusting the brightness and contrast using ImageJ's 'enhance contrast' and 'sharpen' functions. We then binarised the image by applying a local threshold algorithm which considers a window of radius r_{local} around each pixel before applying the threshold method. Various methods are available to binarise grey value images, some of which we compare in figure 3.1. We found the method of Otsu *et al.* [21] to provide a good representation of our original image for a variety of structures. We chose $r_{\text{local}} = 100$ pixels by probing a range of values of r_{local} for some typical images until the variation in the number of bright pixels in the binarised image was low. An example image and its processed form using the Otsu method with $r_{\text{local}} = 100$ pixels are shown in figure 3.2.

After the image had been binarised, to perform the 'particle counting' method we identify particles in the image using ImageJ's 'Analyse Particles' function, excluding particles which were one square pixel in size to ignore the contribution of noise. We then use the number of identified particles N_I in a $L_{I,a} \times L_{I,b}$ image and our knowledge of particle radius r to calculate the surface fraction ϕ by

$$\phi_p = \frac{N_I \pi r^2}{L_{I,a} L_{I,b}} \quad \text{(particle counting)}. \tag{3.1}$$

To perform the 'white fraction' method we simply calculated the fraction of white pixels by

$$\phi_w = \frac{N_{\text{white}}}{N_{\text{black}} + N_{\text{white}}} \quad \text{(white fraction)}. \tag{3.2}$$

Each method has its advantages. Particle counting is suited to well separated and easily distinguishable particles, but the white fraction method better accounts for

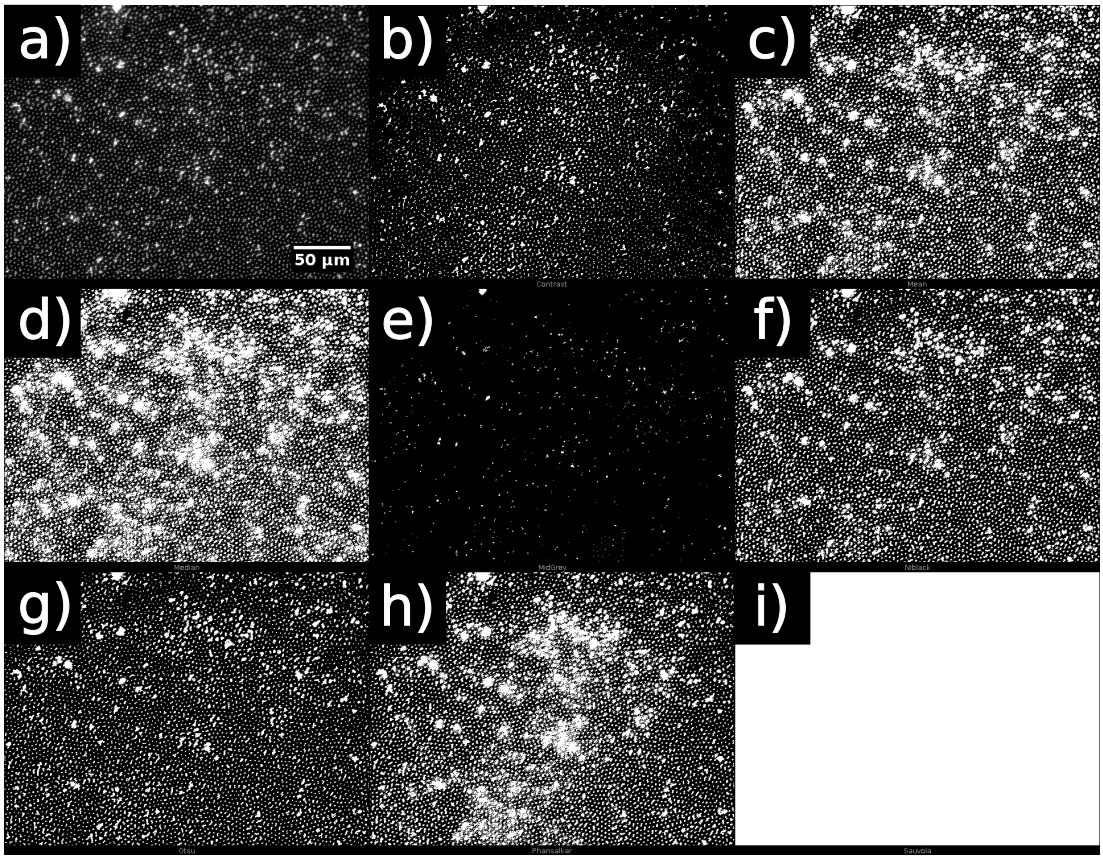

Figure 3.1 *Comparison of threshold methods: a) Original image, b) Contrast, c) Mean, d) Median, e) Mid Grey, f) Niblack, g) Otsu, h) Phansalkar, i) Sauvola. The details of these methods are given in the text.*

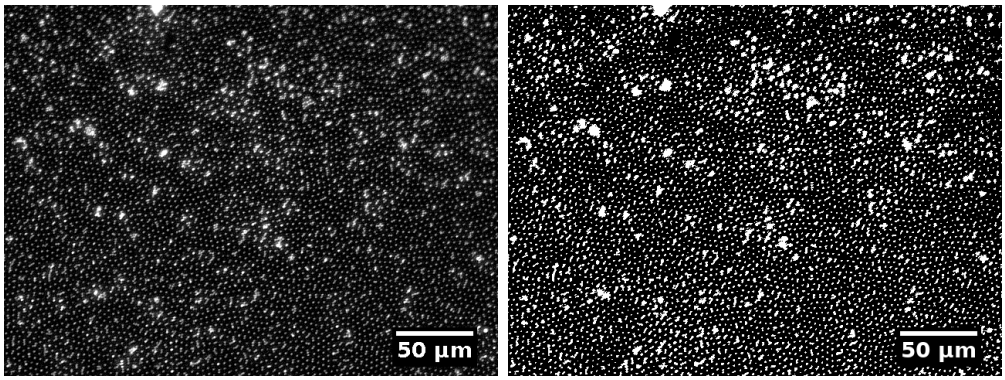

(a) *Fluorescence microscopy image* **(b)** *Binarised image*

Figure 3.2 *A typical image for large particles, and a binarised version of it. The binarisation used the Otsu local threshold method with an r_{local} parameter of 100 pixels or 50 μm.*

aggregates and closely packed particles. With a resolution of $d = 0.59\mu$m (chapter 2) and a pixel width of 0.5μm, we might expect to be able to resolve individual particles for the particle sizes $r = 565$ nm and $r = 1126$ nm if not for $r = 193$ nm. In practice we have found it difficult to consistently resolve individual particles, especially for smaller particles and in surface aggregates.

We now describe the 'Fourier lengthscale' method of estimating the surface fraction. A similar method has been used previously by Planchette *et al.* to estimate the surface fraction [22] of a comparable structure. Each image is first enhanced as described above, but not binarised. The fast Fourier transform is computed using the NumPy package 'fft' [23–25]. Because we have a real image, the Fourier transform has a symmetry: positive and negative Fourier frequencies are equivalent, so we restrict ourselves to positive Fourier frequencies.

The structures we analyse do not show long range orientational order, so the Fourier spectrum shows an angular symmetry. We therefore use this symmetry to reduce the complexity and compute a radial profile of the Fourier power spectrum by averaging over angles from 0 to $\pi/2$. Figure 3.3 illustrates this process as well as the rotational symmetry of the Fourier spectrum. We plot the Fourier spectrum as a function of spatial frequencies ν_x and ν_y in the x and y directions of the image respectively. From the first peak in the radial profile of that spectrum we can identify a characteristic lengthscale as the reciprocal of the peak's position in Fourier space.

We found that for an image where the particles were distinguishable and not motion blurred, the characteristic lengthscale identified from the Fourier transform's radial profile compared well with the typical interparticle spacing

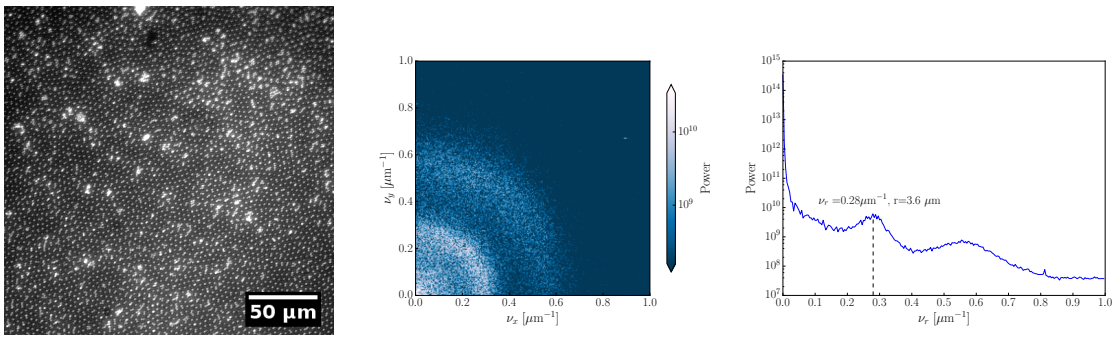

(a) *Fluorescence microscopy image* **(b)** *The Fourier transform* **(c)** *The radial profile of the Fourier tranform*

Figure 3.3 *An illustration of how the Fourier transform of a fluorescence microscopy image of particles at the interface can be used to characterise the length scale. The radial Fourier power profile is plotted as a function of* $\nu_r = \sqrt{\nu_x^2 + \nu_y^2}$.

visible in the image, illustrated by figure 3.4. We thus take this lengthscale L_F to be the mean interparticle separation, and use it to calculate a surface fraction ϕ_F. To do this requires a structural assumption, which we simply take to be a hexagonal lattice and therefore for particles of size r

$$\phi_F = \frac{\pi r^2}{L_F^2 \sin(\pi/3)} \quad \text{(Fourier lengthscale)}. \tag{3.3}$$

This is somewhat justified by the small domains of ordered particles seen in figure 3.5, but a better estimate would account for the more complicated real structure.

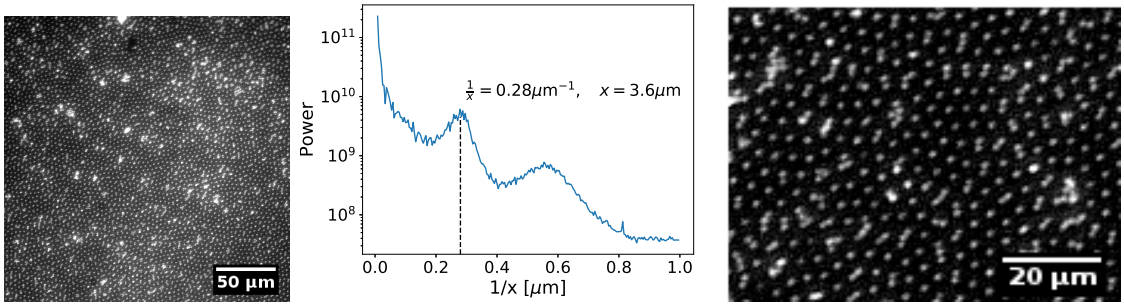

(a) **(b)** **(c)**

Figure 3.4 *Micrograph 3.4a with the radial profile of the Fourier transform of that micrograph 3.4b and a magnified section of the micrograph 3.4c to illustrate how the characteristic Fourier lengthscale corresponds to the interparticle separation.*

It is important to note however, that any micrograph of the particle laden interface is a convolution of the point spread function (PSF) of the microscope with the array of particle centres. By the convolution theorem, the Fourier

transform of the micrograph is then the product of the Fourier transform of the array and the Fourier transform of the PSF. To properly analyse the structure by a Fourier transform we should factor out the Fourier transform of the PSF, but we have left this task for future work.

To explore the effect of the PSF on our surface fraction estimates we consider an idealised image, first without a PSF, then with a Gaussian PSF. To generate our idealised image we built a hexagonal lattice from the lattice vectors, then randomly displaced each particle from its lattice position.

Each particle of radius R at co-ordinates a, b was represented by a disk g_D, or a Gaussian g_G to reflect the point spread function at co-ordinates x, y in the image space:

$$g_D(x, y, a, b) = \begin{cases} 255 & : (x-a)^2 + (y-b)^2 \leq R \\ 0 & : (x-a)^2 + (y-b)^2 > R \end{cases} \tag{3.4}$$

$$g_G(x, y, a, b) = 255 \exp(-((x-a)^2 + (y-b)^2)/2\sigma^2) \tag{3.5}$$

where the factor of 255 enters because in experiments we have an 8-bit image where a pixel with a brightness value of 255 represents the highest possible value, i.e. it is a white pixel. We also disregard the contribution to the brightness from particles more than $\frac{5}{2}R$ or $\frac{5}{2}\sigma$ from the point under consideration to speed up the image generation. We mapped this structure onto a 480×640 pixel image, which is the same size that we acquire in experiments, and applied the methods discussed above to estimate ϕ_p, ϕ_w, and ϕ_F. To do this for particles represented by g_G, we must assume a relationship between the particle radius R and the size of the PSF. For simplicity, we set $R = \sigma$.

For particles without a PSF, and with $R = 1$ μm and $N = 1782$, we found $\phi_p = 7.3\%$, $\phi_w = 7.3\%$, and $\phi_F = 9.6\%$. For particles with the specified PSF we found $\phi_p = 7.3\%$, $\phi_w = 16.0\%$, and $\phi_F = 9.6\%$. Clearly the point spread function has a strong influence on ϕ_w, so we must be careful to treat ϕ_w as an effective surface fraction at best. The Fourier method deviates less from ϕ_p because (like ϕ_p) it measures the spacing between particles, rather than their apparent area.

3.3.2 Cluster Size Distribution

To quantify the degree of aggregation without being able to reliably identify individual particles, we decided to measure the size distribution of isolated regions in the binarised images using ImageJ's 'Analyse Particles' function. Particles of 1 square pixel in size were again excluded to ignore the contribution of noise. For

this method to be accurate, we must assume that the area of a cluster in the binarised image scales with the number of particles in that cluster.

3.3.3 Characterising the Surface Fraction Distribution

So far we have described various image analysis methods for estimating the surface fraction ϕ from one image. However as we later see there is variation in the local value of ϕ across the interface. To account for this variation, we take advantage of the motion of the interfacial structure and simply record a series of images at a known frame rate (usually 0.1 fps) for approximately 10 minutes. We then only keep images which are not visibly motion blurred - the velocity of the motion changes during the observation, so it is possible to capture such images. The images are then processed and measured using the methods described above. We report the results as histograms.

3.4 Results and Discussion

Here we will discuss each particle size in three sections. We describe their qualitative characteristics and present our estimates of the surface fraction by the three methods discussed above, summarising the most important points at the end of each section. We then compare their characteristics in section 3.4.4, which is also where we present a comparison of cluster size distributions and Fourier peak prominences, because these are most insightful relative to each other.

3.4.1 Characterising Deposited Layers of Large Particles

We first discuss the largest and easiest to image particles of radius $r = 1126$ nm. As can be seen in figure 3.5, the particles display a long-range repulsion which leads to very small ordered domains less than 10 particles in size. Amongst these there are small aggregates which repel the surrounding particles and aggregates. The aggregation does not seem to progress significantly over a waiting period of one hour, and aggregates have not been observed to dissociate.

The characteristics of this structure can be explained by the combination of a long-ranged repulsion and a short-ranged attraction. The long-range repulsion causes some order to be formed, while the short-ranged attraction holds aggregates together. These aggregates may have been present before deposition, or may have been formed in the deposition process.

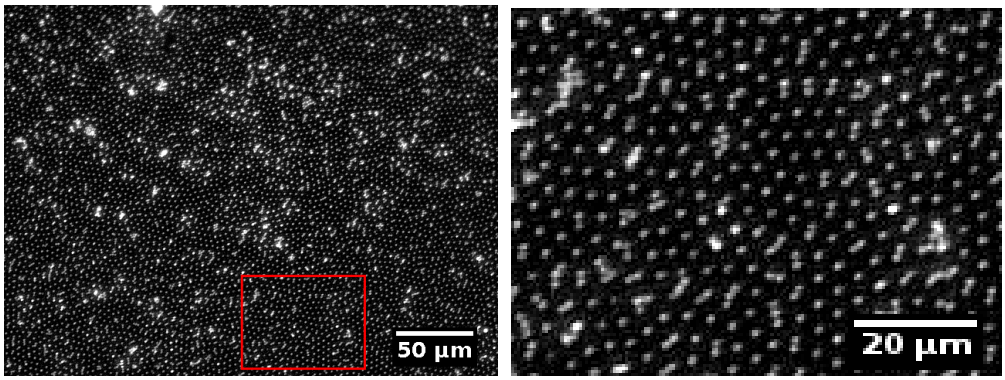

(a) (b)

Figure 3.5 *Fluorescence micrographs showing (a) a typical image of an interfacial layer of $r = 1126$ nm PHSA-PMMA particles at a water/n-dodecane interface, and (b) a magnified section (marked in red) of that image.*

A number of the smallest aggregates formed from two or three particles are linear or chain-like, which is a signature of long range repulsion. The short ranged attraction is likely due to the roughness-induced capillary attraction that Stamou *et al.* observed [26]. However, they could distinguish between van der Waals forces and capillary forces by their large (more than 1 μm) interparticle separation; van der Waals energies are very weak (lower than thermal energy) at separations more than about a μm. In contrast, our particles are not so widely separated in aggregates so it is less clear which attractive force is responsible.

We attribute the long range repulsion to electrostatic repulsion since it is the only known interaction that can explain the range we see in the images. This is surprising for sterically-stabilised particles, and we discuss this problem in more detail in chapter 5 where we quantitatively analyse the interparticle forces through the interfacial rheology. To summarise that discussion, the electrostatic repulsion may arise either from dissociating PHSA groups on the particle surface, or from the charged interface which makes the particles act as holes in a charged plane.

These qualities contrast with charge-stabilised particles which typically display much stronger order. But this is of course highly dependent on the concentrations of any surfactant or salt that is present, as well as the particle hydrophobicity [27–29].

The interfacial particles also move collectively, such that the structure in view is well-preserved, though deformation may be ongoing out of the field of view. The structure also has regions of higher and lower density which often present as bands

(figure 3.6) which are around 100 μm in width and much longer than the field of view. These bands are observed as the interfacial layer moves through the field of view. They are likely formed by the injection of the concentrated dispersion: we have not observed them in interfacial layers formed by sedimentation of a homogeneous, low volume-fraction dispersion.

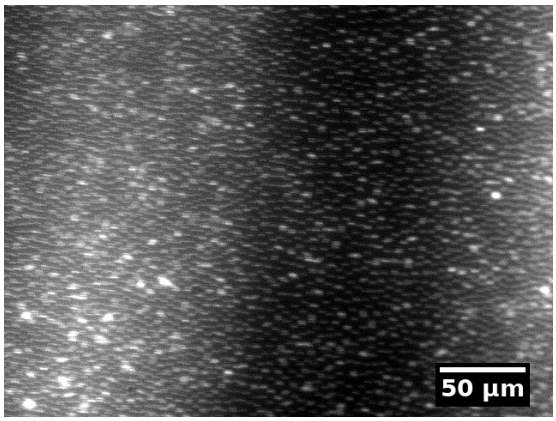

Figure 3.6 *Fluorescence micrograph showing a band-like structure in an interfacial layer of r = 1126 nm PHSA-PMMA particles at a water/n-dodecane interface.*

The extent of this large-scale variation is reflected in the distribution of surface fractions measured. Figure 3.7 compares three methods of surface fraction measurement for a representative sample, while table 3.1 summarises their mean values and standard deviations.

There are two points to be discussed here. First, each method produces a different mean surface fraction ϕ, with the particle counting method (ϕ_p) far lower and narrower than the others. This is because the particle counting fails to identify all of the individual particles within aggregates and thus counts fewer than exist. The white fraction (ϕ_w) and Fourier lengthscale (ϕ_F) methods are less distinguished from each other. While their mean values are separated by more than the error, ϕ_F will vary depending on what structure is used to calculate it from the characteristic lengthscale. We used a simple hexagonal lattice, but a more disordered structure - as in figure 3.5 for example - would give a lower ϕ_F, closer to the value of ϕ_w. Because of the difficulty in particle counting for our system and the small difference between white fraction and Fourier methods, we conclude that our best estimate of the surface fraction is close to ϕ_w and ϕ_F, around 20-25%. This is important, because it is significantly less than the surface fraction expected from the amount of particles added to the system so we cannot trust that all particles adsorb by the time the interface is probed.

The second point concerns the width of the distribution, which is approximated

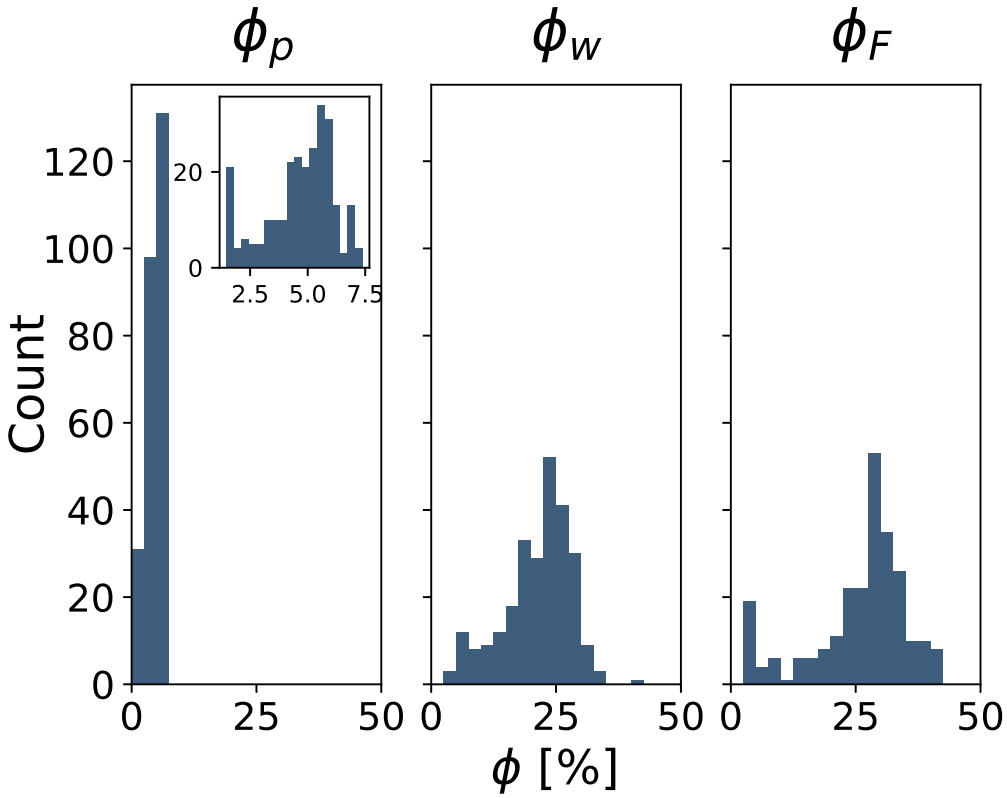

Figure 3.7 *Histogram of surface fractions ϕ measured by three methods over 10 minutes for a sample of $r = 1126$ nm PHSA-PMMA particles at a water/n-dodecane interface. Methods are particle counting ϕ_p, white fraction ϕ_w, and Fourier lengthscale ϕ_F (see text). Bins are 2.5% wide.*

by the standard deviation. From those values it is clear that there is substantial variation in density across the interfacial plane, with the width of each distribution greater than 30% of the mean. We attribute this variation to the particle addition method, which deposits relatively high local concentrations of particles in various spots across the interface.

Method	ϕ [%]	σ [%]	σ/ϕ
Particle Counting, ϕ_p	4.688 ± 0.006	1.5	0.31
White Fraction, ϕ_w	21.33 ± 0.03	7	0.32
Fourier Lengthscale, ϕ_F	25.91 ± 0.04	10	0.37

Table 3.1 *Comparison of surface fraction ϕ, the standard deviation σ, and σ normalised by the mean for three methods of surface fraction measurement for $r = 1126$ nm particles.*

To build a more homogeneous layer we could have instead dispersed the particles in the oil layer above the interface and allowed sedimentation to bring the particles to the interface. However, this requires a longer time to prepare the interface for smaller particles (which sediment more slowly) so interface ages would not be comparable across particle sizes. This method also prevents the calibration of the bare interface, which was discussed in chapter 2.
In summary, we found that large particles produce an interfacial layer with a mixture of individual particles in small ordered domains and small aggregates, that there is significant variation in density across the layer, and that both $\phi_w = 21.33 \pm 0.03$ % and $\phi_F = 25.91 \pm 0.04$ % are reasonable estimates for the mean surface fraction.

3.4.2 Characterising Deposited Layers of Medium-Sized Particles

Having discussed the large ($r = 1126$ nm) particles, we now turn to the medium ($r = 565$ nm) sized particles in this section. In figure 3.8 we present a micrograph of 565 nm particles at an interface. It is characterised by clusters of various sizes which remain well-separated over time, though there is little orientational order. In the magnified section we can see a small number of individual particles, which are much more difficult to identify than the large particles. On larger scales (more than $\mathcal{O}(100)$ μm), there seems to be less variation in density than we observed for large particles. Having outlined the qualities of the structure, we now turn to quantifying the density.

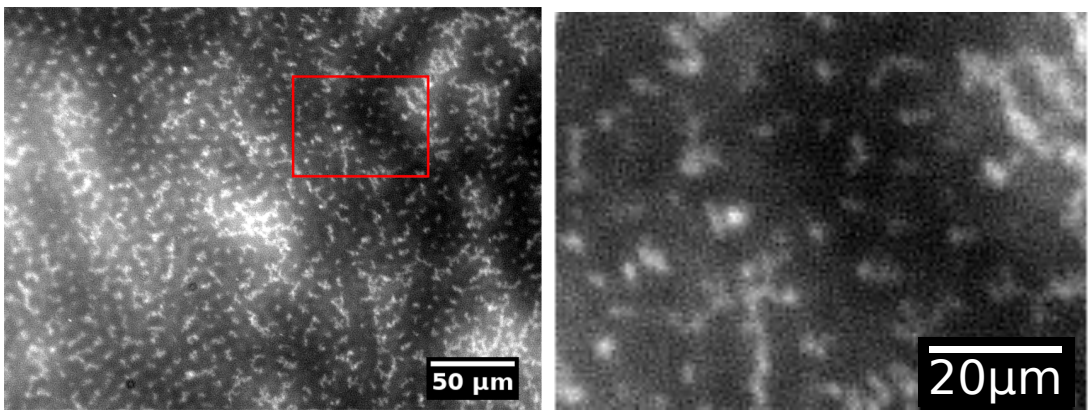

(a) **(b)**

Figure 3.8 *(a) Typical fluorescence micrograph of an interfacial layer of PHSA-PMMA particles of radius $r = 565$ nm at a water/n-dodecane interface, with (b) a magnified section marked in red.*

Figure 3.9 and table 3.2 show the measured surface fractions using the three methods (ϕ_p, ϕ_w, and ϕ_F) described above. The most striking is ϕ_p with a mean value of 0.546 ± 0.001. There are two reasons we should not be surprised by how low this is: first is that individual particles within aggregates are hard to identify in the binarised image, so fewer particles are counted by this method than exist; second is that the particle area has decreased so each particle covers a smaller area. Once we understand that this method fails to capture most particles, we cannot trust ϕ_p for this structure.

Similarly ϕ_F is low, with a mean of $\phi_F = 1.39\%$. This method struggles with this type of interfacial structure because there is a range of lengthscales characterising it - there are different cluster sizes as well as the interparticle separation - so it is more difficult to identify the interparticle separation. This is discussed in more detail when we compare particle sizes in section 3.4.4. Even if we identify the interparticle or inter-cluster separation, we cannot account for the number of particles in each cluster, so we underestimate the number of particles and we cannot trust ϕ_F for this structure.

This leaves us with ϕ_w, which does account for particles in aggregates. While it is subject both to imaging conditions and the binarisation procedure and we have no calibration method, ϕ_w is likely our best estimate of ϕ. With a value of $\phi_p = 33.03$ % it is comparable to our estimate for large particles, which is reasonable given that i) we add the same interfacial area of particles for both and ii) that both particle sizes should have sedimented to the interface by the time of observation, as discussed in chapter 2. The narrower distribution of ϕ_w than large particles supports our earlier observation that there is less large-scale variation in density.

Method	ϕ [%]	σ [%]	σ/ϕ
Particle Counting, ϕ_p	0.546 ± 0.001	0.11	0.21
White Fraction, ϕ_w	33.03 ± 0.03	3	0.082
Fourier Lengthscale, ϕ_F	1.390 ± 0.002	0.2	0.16

Table 3.2 *Comparison of surface fraction ϕ, the root mean squared deviation σ, and σ normalised by the mean for three methods of surface fraction measurement for $r = 565$ nm particles.*

In summary, we found that the structure for medium-sized particles is characterised by a range of small aggregates, that there is little large-scale variation in density across the layer, and that only $\phi_w = 33.03 \pm 0.03$ % offers a reasonable

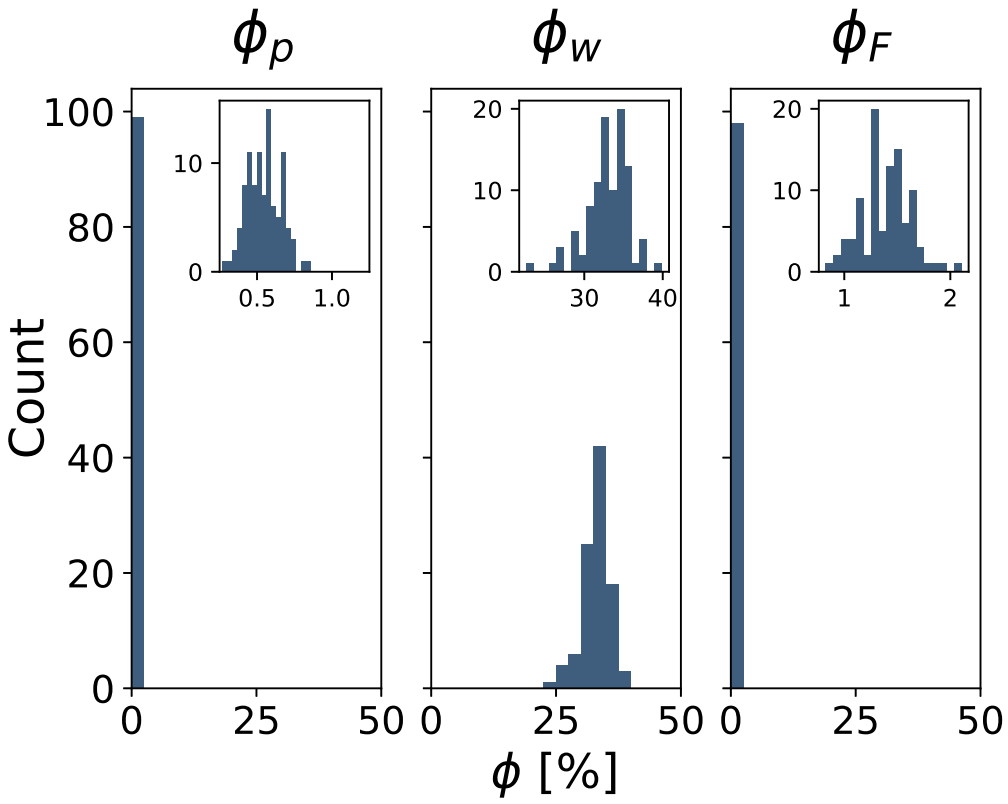

Figure 3.9 *Histogram of surface fractions ϕ measured by three methods over 10 minutes for a sample of $r = 565$ nm PHSA-PMMA particles at a water/n-dodecane interface. Methods are particle counting ϕ_p, white fraction ϕ_w, and Fourier lengthscale ϕ_F (see text). Bins are 2.5% wide.*

estimate of the surface fraction.

3.4.3 Characterising Deposited Layers of Small Particles

We now discuss the micrographs and surface fraction estimates for the smallest particles we considered, $r = 193$ nm. As we can see from figure 3.10, regions of small aggregates or individual particles co-exist with large aggregates which extend far beyond the field of view. It is difficult to distinguish individual particles from small aggregates, and a range of aggregate sizes exist, up to several hundred microns. We have not observed individual particles joining or leaving aggregates, which suggests that there are energy barriers to both processes.

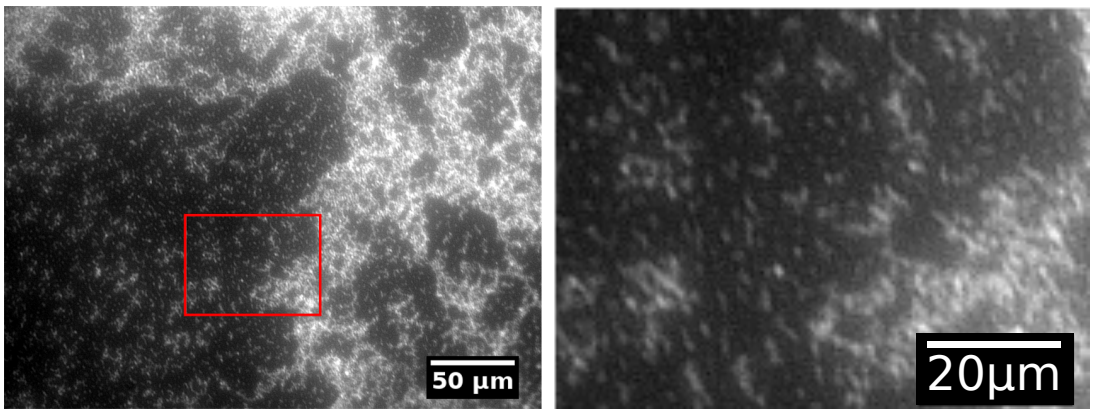

(a) **(b)**

Figure 3.10 *(a) Typical fluorescence micrograph of an interfacial layer of PHSA-PMMA particles of radius $r = 193$ nm at a water/n-dodecane interface, with (b) a magnified section marked in red.*

Measuring the surface fraction for these particles presents more of the same difficulties we found for medium-sized particles. The particle counting and Fourier lengthscale methods both fail to account for aggregates, which are a significant characteristic of this interface, and their very low ϕ noted in table 3.3 and shown in figure 3.11 reflects this. The range of aggregate sizes also means that the Fourier peak is even weaker, as shown in figure 3.14.

The white fraction method is again our best estimate of ϕ. At $\phi = 27.48\%$ it is comparable to the estimates for medium and large sized particles. This might seem surprising given that we added a greater interfacial area of particles (see chapter 2) but it is important to remember that more particles were added to observe a comparable surface pressure response to the larger particles as the area was reduced by a given range. It is therefore not too surprising that the surface fraction is comparable to what we measured for larger particles.

The effect of large aggregates is clear in the distribution of ϕ_w shown in figure 3.11 and parametrised in table 3.3. Its relative width σ/ϕ is large, and the distribution

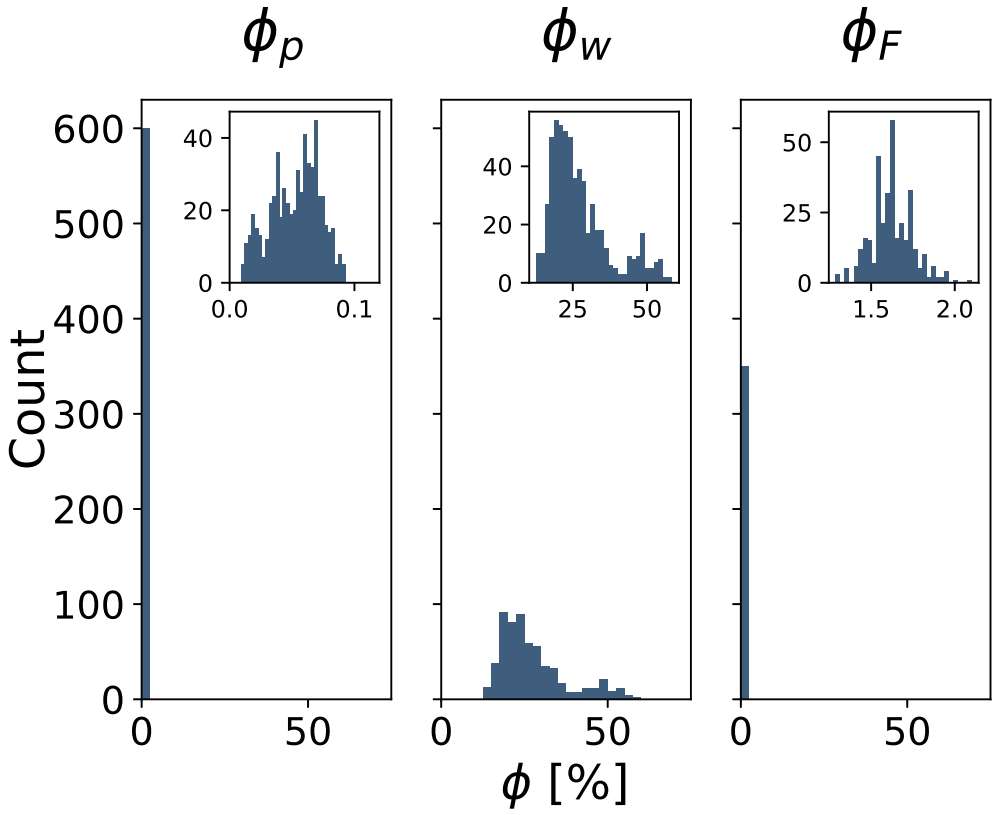

Figure 3.11 *Histogram of surface fractions ϕ measured by three methods over 10 minutes for a sample of $r = 193$ nm particles. Methods are particle counting ϕ_p, white fraction ϕ_w, and Fourier lengthscale ϕ_F. Bins are 2.5% wide.*

is skewed towards higher densities - there is even a secondary peak visible. High densities are recorded when large aggregates fill the field of view as they move across it.

Method	ϕ [%]	σ [%]	σ/ϕ
Particle Counting, ϕ_p	$(5.250 \pm 0.003) \times 10^{-2}$	0.02	0.37
White Fraction, ϕ_w	27.48 ± 0.02	10	0.36
Fourier Lengthscale, ϕ_F	1.6252 ± 0.0003	0.12	0.076

Table 3.3 *Comparison of surface fraction ϕ, the root mean squared deviation σ, and σ normalised by the mean for three methods of surface fraction measurement for $r = 193$ nm PHSA-PMMA particles at a water/n-dodecane interface.*

In summary, the structure for small particles is characterised by the coexistence of a range of small aggregates with large aggregates several hundred microns in

size, and the mean density was best estimated by the white fraction method $\phi_w = 27.48 \pm 0.02$ %, comparable to large and medium-sized particles.

3.4.4 Comparison of Particle Sizes

In this section we first compare the density distributions for three particle sizes using the white fraction method. After that, we will compare the degree of aggregation across particle sizes. We conclude the section with suggestions for why we observe the differences between particle sizes.

As discussed above, the white fraction method proved to be the only one of the considered methods which worked for all three sizes and the variety of structures we studied. Figure 3.12 compares the distributions of this quantity for the three sizes, while table 3.4 summarises their properties.

It is important to note that the measured surface fractions are significantly lower than would be expected from the number of particles added. Recall from chapter 2 that we added enough particles for surface fractions of 77%, 77%, and 11000 % for large, medium, and small particles respectively if all particles added were adsorbed. Yet, we see ϕ_w = 21%, 33%, and 27% respectively. Clearly for all particle sizes, not all of the particles we expected to adsorb have adsorbed by the time of observation. This shows the importance of measuring the surface fraction, especially when particles are not spread at the interface. Particles could be sequestered on other surfaces such as the trough barriers or the pipette tips used for dispensation. It is also known that there are kinetic barriers to adsorption [5]. While we have not observed particle build-up near the interface (as we would expect due to gravity) we have not ruled this possibility out.

However, we have achieved reasonably similar initial densities for each size. We require this so that they can all provide a measurable and therefore comparable surface pressure response when the interface is compressed. In this sense, we have shown the interface preparation method to be suitable for our experiments.

While the mean densities are not dissimilar, the shape of the ϕ_w distribution varies with particle size and reflects the various characteristics we described in their respective sections. Judging by figure 3.12 and the properties in table 3.4, large particles show a wide distribution skewed towards low densities. This matched our observations of large-scale density variation in the form of bands of lower density.

Medium-sized particles have a narrower distribution, reflecting the lack of large-scale density variation. Its skewness is actually stronger than for large particles, but we must remember that skewness is defined relative to the root mean squared

deviation and its absolute skew is lower. The smallest particles present a quite different picture, with a large width and skew towards higher densities due to the presence of large aggregates.

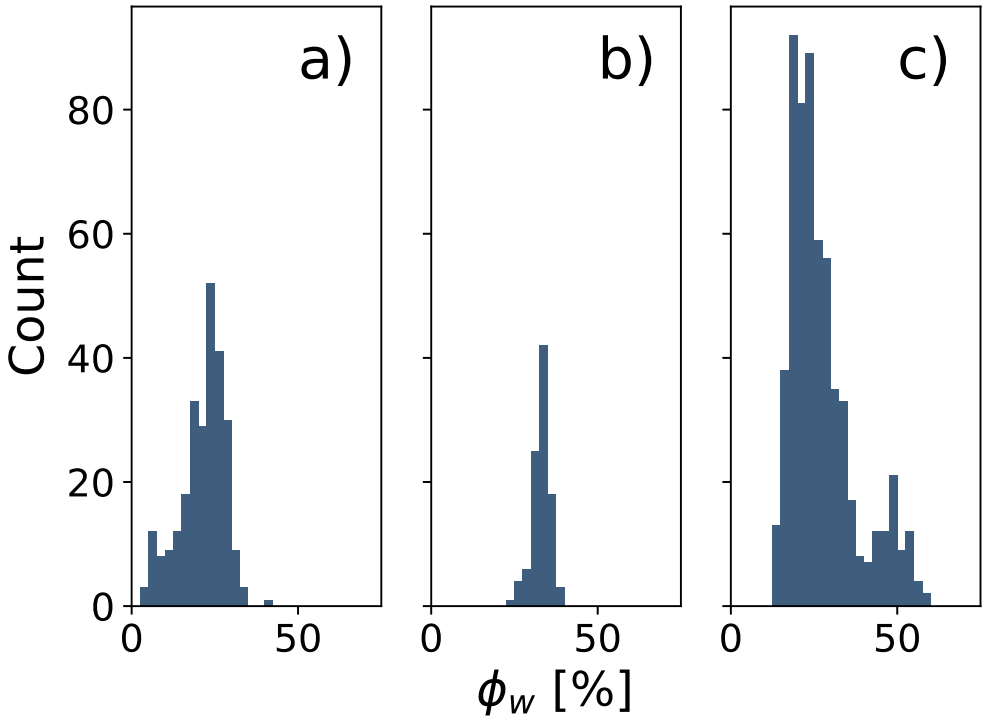

Figure 3.12 *Histogram of surface fractions ϕ_w measured by the white fraction method over 10 minutes for three sizes of PHSA-PMMA particles: a) r = 1126 nm, b) r = 565 nm, and c) r = 193 nm. Bins are 2.5% wide.*

Particle radius [nm]	ϕ_w [%]	σ [%]	σ/ϕ	skewness
1126	21.33 ± 0.03	7	0.32	-0.69
565	33.03 ± 0.03	3	0.082	-0.81
193	27.48 ± 0.02	10	0.36	1.2

Table 3.4 *Comparison of surface fraction ϕ, the root mean squared deviation σ, σ normalised by the mean, and distribution skewness for the white fraction method of surface fraction measurement for three sizes of particles.*

While the ϕ_w distributions do show some important features of the interfacial structure, the change in aggregate size is not clear from them. Petkov *et al.*

[18] showed that aggregation number had a clear effect on surface pressure, so it is important that we try to assess this variation. In figure 3.13 we compare the distribution of continuous regions in binarised images of each size of particle. There it is clear that as particle size decreases, more large aggregates appear.

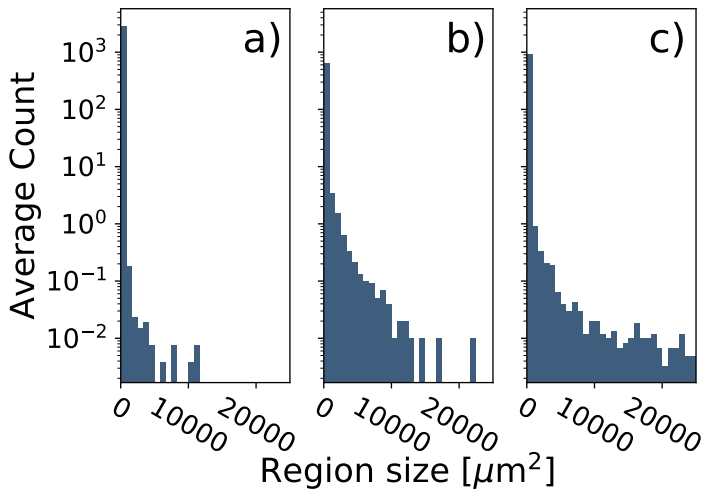

Figure 3.13 *Comparison of region size distributions for three PHSA-PMMA particle sizes: a) $r = 1126$ nm, b) $r = 565$ nm, and c) $r = 193$ nm. Counts for each region size are averaged over all selected images.*

This is also reflected in the Fourier power spectra for the various sizes of particle. Figure 3.14 compares representative power spectra for each size. The prominence of the peak in the spectrum decreases with particle size due to existence of particle aggregates.

From the above, it is clear that as particle size decreases, we observe more large aggregates. As mentioned for each particle size, we have not observed further aggregation at the interface, which suggests that the aggregation occurs before or during deposition.

This variation might be due to changes in particle interaction: the model Aveyard *et al.* proposed for electrostatic repulsion predicted a surface pressure proportional to the particle radius, if the surface fraction is constant (so that particle separation is proportional to radius), and if the contact angle is independent of size (so that the distance perpendicular to the interface is proportional to radius) [30]. If attraction is due to roughness-induced capillary interactions, then Stamou *et al.*'s quadrupole expression for the interaction energy (only valid for long ranges, but we use it here for estimation) $\delta E \propto R^4/L^4$ for particle separation L implies a surface pressure of approximately $Pi \propto 1/R^2$ if

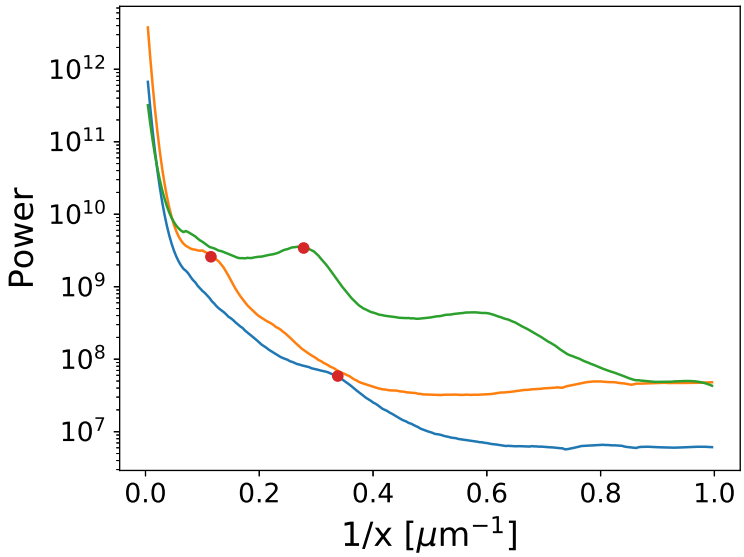

Figure 3.14 *Comparison of characteristic Fourier lengthscales for three PHSA-PMMA particle radii: $r = 1126$ nm (green), $r = 565$ nm (orange), and $r = 193$ nm (blue). Characteristic lengthscales have been marked for each with a red dot.*

the surface fraction is constant. Therefore our estimations suggest that repulsion decreases with particle size while attraction increases, which would explain the observed aggregation.

We might also explain this variation in aggregation simply by sedimentation times. Hydrodynamic drag scales more slowly with increasing size than the force due to gravity: we can see this for viscous flow (which we are likely to encounter in sedimentation) by comparing the Stokes drag for viscosity ν and speed v,

$$F_{\text{Stokes}} = 6\pi\nu R v \tag{3.6}$$

to the force of gravity

$$F_{\text{gravity}} = \frac{4}{3}\pi\rho_p R^3 g \tag{3.7}$$

for particle density ρ_p. Equations 3.6 and 3.7 make it clear that smaller objects are slower to sediment.

Let us model the way we have prepared our colloidal layer as initially being a fixed thickness of colloidal dispersion above the interface, which we observe after some waiting time.

Even if the distribution of cluster sizes for large and small particles are identical in bulk, it will not be the case at the interface. This is because for large particles, all of the particles and clusters reach the interface and the cluster size

distribution is the same as the bulk. But for small particles, individual particles and smaller aggregates may not have time to reach the interface before we make our observations so the distribution at the interface becomes biased towards the larger clusters which reach it in time.
It is worth noting that the bulk cluster size distributions are unlikely to be the same for large and small particles because that would require very large aggregates to exist for large particles at the interface, which we have not observed.
Some studies have used the structure of equilibrated colloidal layers to calculate effective pair-interaction potentials, for example Parolini *et al.* though they used a spreading method and observe very few aggregates [31]. If our goal is to make deductions about particle interactions at the interface from the interfacial structure, future experiments must eliminate this sedimentation bias, as well as other factors such as insufficient dispersion first.

3.5 Conclusions

In this chapter we show that we have prepared comparable surface fractions of particle-laden interfaces for three sterically-stabilised particle sizes at a water-dodecane interface. These densities were found to be less than expected from the number of particles added to the system, especially for small particles. This affirms the importance of measuring the surface density, particularly where comparisons across particle sizes need to be made.
Regarding structure, there are significant changes as particle size varies: decreasing particle size increases the range of aggregate sizes and the number of aggregates, with the smallest particles presenting aggregates several hundreds of microns in size. We have not observed aggregation at the interface, so the difference must originate during deposition or from the bulk phase. We offered explanations as to how interfacial aggregation variation across particle sizes could appear from the bulk phase as a result of different cluster size distributions or as a result of the difference in sedimentation times of large and small clusters.

Bibliography

[1] Armando Maestro, Omkar S Deshmukh, Frieder Mugele, and Dominique Langevin. Interfacial assembly of surfactant-decorated nanoparticles: on the rheological description of a colloidal 2d glass. *Langmuir*, 31(23):6289–6297, 2015.

[2] Job HJ Thijssen and Jan Vermant. Interfacial rheology of model particles at liquid interfaces and its relation to (bicontinuous) pickering emulsions. *Journal of Physics: Condensed Matter*, 30(2):023002, 2017.

[3] Sepideh Razavi, Kathleen D. Cao, Binhua Lin, Ka Yee C Lee, Raymond S. Tu, and Ilona Kretzschmar. Collapse of Particle-Laden Interfaces under Compression: Buckling vs Particle Expulsion. *Langmuir*, 31(28):7764–7775, 2015.

[4] DY Zang, E Rio, D Langevin, B Wei, and BP Binks. Viscoelastic properties of silica nanoparticle monolayers at the air-water interface. *European Physical Journal E*, 31(2):125–134, 2010.

[5] Valeria Garbin, John C. Crocker, and Kathleen J. Stebe. Nanoparticles at fluid interfaces: Exploiting capping ligands to control adsorption, stability and dynamics. *Journal of Colloid and Interface Science*, 387(1):1–11, 2012.

[6] A Maestro, LJ Bonales, H Ritacco, RG Rubio, and F Ortega. Effect of the spreading solvent on the three-phase contact angle of microparticles attached at fluid interfaces. *Physical Chemistry Chemical Physics*, 12(42):14115–14120, 2010.

[7] NID Fenwick, F Bresme, and N Quirke. Computer simulation of a langmuir trough experiment carried out on a nanoparticulate array. *The Journal of Chemical Physics*, 114(16):7274–7282, 2001.

[8] Adrienne Nelson, Dapeng Wang, Kaloian Koynov, and Lucio Isa. A multiscale approach to the adsorption of core–shell nanoparticles at fluid interfaces. *Soft matter*, 11(1):118–129, 2015.

[9] Joe W Tavacoli, Gijs Katgert, E Grace Kim, Michael E Cates, and Paul S Clegg. Size limit for particle-stabilized emulsion droplets under gravity. *Physical review letters*, 108(26):268306, 2012.

[10] Joseph D Berry, Michael J Neeson, Raymond R Dagastine, Derek YC Chan, and Rico F Tabor. Measurement of surface and interfacial tension using pendant drop tensiometry. *Journal of colloid and interface science*, 454:226–237, 2015.

[11] Sebastian Knoche, Dominic Vella, Elodie Aumaitre, Patrick Degen, Heinz Rehage, Pietro Cicuta, and Jan Kierfeld. Elastometry of deflated capsules:

Elastic moduli from shape and wrinkle analysis. *Langmuir*, 29(40):12463–12471, 2013.

[12] Pietro Cicuta, Edward J Stancik, and Gerald G Fuller. Shearing or compressing a soft glass in 2d: time-concentration superposition. *Physical review letters*, 90(23):236101, 2003.

[13] LJ Bonales, JEF Rubio, H Ritacco, C Vega, RG Rubio, and F Ortega. Freezing transition and interaction potential in monolayers of microparticles at fluid interfaces. *Langmuir*, 27(7):3391–3400, 2011.

[14] Valeria Garbin, John C. Crocker, and Kathleen J. Stebe. Forced desorption of nanoparticles from an oil-water interface. *Langmuir*, 28(3):1663–1667, 2012.

[15] S Kutuzov, J He, R Tangirala, T Emrick, TP Russell, and A Böker. On the kinetics of nanoparticle self-assembly at liquid/liquid interfaces. *Physical Chemistry Chemical Physics*, 9(48):6351–6358, 2007.

[16] Francois Reincke, Willem K Kegel, Hao Zhang, Marc Nolte, Dayang Wang, Daniel Vanmaekelbergh, and Helmuth Möhwald. Understanding the self-assembly of charged nanoparticles at the water/oil interface. *Physical Chemistry Chemical Physics*, 8(33):3828–3835, 2006.

[17] Yi Zhang, Songcheng Wang, Jiarun Zhou, Ruiyang Zhao, Gregory Benz, Stephane Tcheimou, J Carson Meredith, and Sven H Behrens. Interfacial activity of nonamphiphilic particles in fluid–fluid interfaces. *Langmuir*, 33(18):4511–4519, 2017.

[18] Plamen V Petkov, Krassimir D Danov, and Peter A Kralchevsky. Monolayers of charged particles in a langmuir trough: Could particle aggregation increase the surface pressure? *Journal of colloid and interface science*, 462:223–234, 2016.

[19] Lennart Bergström. In Bernard P Binks and Tommy S Horozov, editors, *Colloidal particles at liquid interfaces*, chapter 2. Cambridge University Press, 2006.

[20] JC Fernández-Toledano, A Moncho-Jordá, F Martínez-López, and R Hidalgo-Alvarez. Spontaneous formation of mesostructures in colloidal monolayers trapped at the air- water interface: A simple explanation. *Langmuir*, 20(17):6977–6980, 2004.

[21] Nobuyuki Otsu. A threshold selection method from gray-level histograms. *IEEE transactions on systems, man, and cybernetics*, 9(1):62–66, 1979.

[22] Carole Planchette, Elise Lorenceau, and Anne-Laure Biance. Surface wave on a particle raft. *Soft Matter*, 8(8):2444–2451, 2012.

[23] np.fft.fft2 - numpy v1.15 manual. `https://docs.scipy.org/doc/numpy-1.15.0/reference/generated/numpy.fft.fft2.html`. Accessed: 2019-01-03.

[24] James W Cooley and John W Tukey. An algorithm for the machine calculation of complex fourier series. *Mathematics of computation*, 19(90):297–301, 1965.

[25] William H Press, Saul A Teukolsky, William T Vetterling, and Brian P Flannery. *Numerical recipes 3rd edition: The art of scientific computing*. Cambridge university press, 2007.

[26] Dimitris Stamou, Claus Duschl, and Diethelm Johannsmann. Long-range attraction between colloidal spheres at the air-water interface: The consequence of an irregular meniscus. *Physical Review E*, 62(4):5263, 2000.

[27] Robert Aveyard, John H Clint, Dieter Nees, and Nick Quirke. Structure and collapse of particle monolayers under lateral pressure at the octane/aqueous surfactant solution interface. *Langmuir*, 16(23):8820–8828, 2000.

[28] Tommy S Horozov, Robert Aveyard, Bernard P Binks, and John H Clint. Structure and stability of silica particle monolayers at horizontal and vertical octane- water interfaces. *Langmuir*, 21(16):7405–7412, 2005.

[29] Tommy S Horozov, Robert Aveyard, John H Clint, and Bernard P Binks. Order- disorder transition in monolayers of modified monodisperse silica particles at the octane- water interface. *Langmuir*, 19(7):2822–2829, 2003.

[30] Robert Aveyard, John H Clint, Dieter Nees, and Vesselin N Paunov. Compression and structure of monolayers of charged latex particles at air/water and octane/water interfaces. *Langmuir*, 16(4):1969–1979, 2000.

[31] Lucia Parolini, Adam D Law, Armando Maestro, D Martin A Buzza, and Pietro Cicuta. Interaction between colloidal particles on an oil–water interface in dilute and dense phases. *Journal of Physics: Condensed Matter*, 27(19):194119, 2015.

Chapter 4

Surface Pressure Variation with Particle Size

4.1 Abstract

In this chapter we study the effect on interfacial rheology of a basic characteristic of a colloidal particle - its size. We will first discuss the work which has already been done on the subject and identify typical stress-response behaviour for particle-laden interfaces under strain. We then discuss our own experiments, which use a Langmuir-Pockels trough with complementary imaging to study three sizes of sterically-stabilised particles ranging from 0.2 μm to 1.1 μm in radius. We show that while the stress response appears at first to depend on particle size, this is in fact likely due to particle aggregation. Improved dispersion of particles leads to much more comparable structures and a similar stress response for the three sizes considered. This finding is useful for the control of interfacial structure and mechanical response in colloidal monolayers.

4.2 Introduction

Previously in chapter 1 we introduced the principles of interfacial rheology and described our constitutive model for understanding the interfacial stress response of a particle-laden interface. Chapter 2 discussed the practical details and limitations of how we can measure this response using a Langmuir-Pockels trough. In this chapter we study the effect of colloidal particle size on the interfacial rheology of adsorbed layers of particles. We will first discuss the subject background and identify typical stress-response behaviour for particle-laden

interfaces under strain. We then discuss our own experiments on three sizes of particle (ranging from 0.2 μm to 1.1 μm in radius) and show that while the stress response appears at first to depend on particle size, this is in fact likely due to particle aggregation. A different preparation of particles (by sonication immediately before use) leads to much more comparable structures and a very similar stress response for the three sizes considered.

Often, this stress-strain relationship is expressed in terms of the surface pressure Π as a function of the trough area A. The typical shape for a $\Pi(A)$ curve is shown in figure 4.1a. It consists of a very slow increase at large areas (region A) corresponding to long-range 'soft' repulsions. As A decreases this gives way to a faster rise in surface pressure (region B) as particles come into close contact, before the rate of increase drops - the 'knee' in the curve, where the surface pressure reaches the collapse pressure Π_c [1, 2]. Finally, the surface pressure reaches a plateau - region C - because the interface releases additional stress through the collapse mode. This same response is expressed as a function of the more easily generalisable surface fraction ϕ in figure 4.1b.

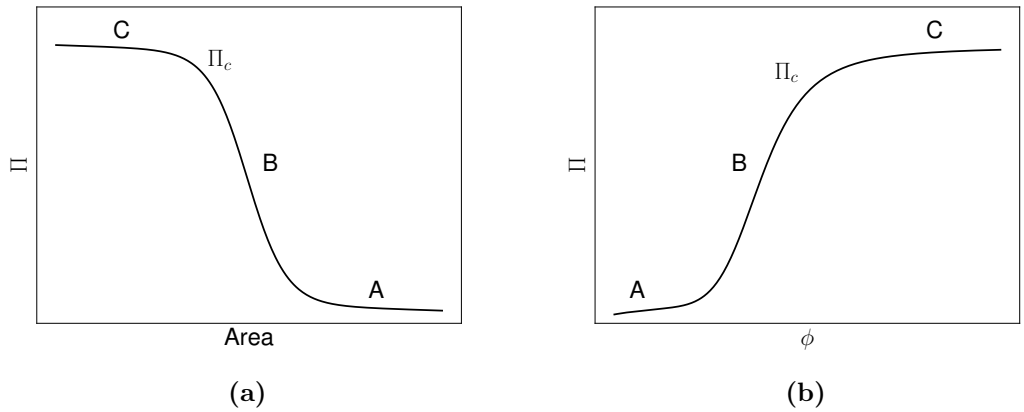

Figure 4.1 *A schematic showing the typical surface pressure of a particle-laden interface under strain in a Langmuir-Pockels trough as a function of (a) area A and (b) surface fraction ϕ.*

A number of models exist to connect the microscopic properties of the colloidal particles to the surface pressure response of the whole particle-laden interface, which we discussed in chapter 1. There is no clearly established model, and different models predict different variation with particle size. For example, the adsorption-only model of Du *et al.* used by Zhang *et al.* [3, 4] predicts that the surface pressure is independent of particle size, and the electrostatic interaction-only model of Aveyard *et al.* predicts the same [5], though a more complete

calculation may introduce a dependence on particle size [6]. Chapters 5 and 6 will make a quantitative comparison with the available models. In this chapter, we focus on the relative changes with particle size.

The 'knee' and plateau are associated with collapse of the monolayer. Different collapse modes such as buckling or particle expulsion exist - see the recent review by Garbin [7] - and we discuss a novel mode in chapter 7. Early work by Horvolgyi *et al.* and Aveyard *et al.* found that buckling consistently occurred when the surface pressure reached the bare interfacial tension i.e. $\Pi_c = \gamma_0$ [8, 9]. But a study using both a Langmuir-Pockels trough and particle covered drop by Monteux *et al.* showed that the 'knee' occurred at surface pressures 5-15 mN/m below γ_0 [10]. And, more recently Razavi *et al.* found that (for particles where buckling occurred) Π_c was 30 mN/m below γ_0 [11]. It may be the case that the apparent Π_c is lower than the true Π_c - for example if the surface pressure is anisotropic or Janssen effects are important [12] as we discussed in chapter 2. Currently it is not clear that $\Pi_c = \gamma_0$ is a general condition for buckling. For particle expulsion we would expect Π_c to vary with particle desorption energy - which is affected by particle size and contact angle [13]. As an example, the apparent collapse pressure was found to be $\Pi_c \approx 20$ mN/m by Razavi *et al.* for hydrophilic silica particles ($\theta \approx 30°$) at the water-air interface, and these particles were thought to be expelled while more hydrophobic ($\theta \approx 120°$) particles were found to collapse by buckling at $\Pi_c \approx 40$ mN/m [11].

Now that we have discussed the surface pressure response illustrated by figure 4.1, we can explore the effect of particle size on this response. Experimentally, only a small number of authors have examined this. Aveyard *et al.* studied particle sizes ranging (in diameter) from 0.21 μm to 2.6 μm, and following on from Kumaki found that only the largest particles produced an isotropic surface pressure i.e. $\Pi(A)$ did not change with plate orientation, so their attention was focused on the larger particles [5, 14].

The electrostatic interaction model Aveyard *et al.* proposed to explain their data predicted a surface pressure proportional to the particle radius, if the surface fraction is constant (so that particle separation is proportional to radius), and if the contact angle is independent of size (so that the distance perpendicular to the interface is proportional to radius) [5]. More recently, Monteux *et al.* considered particle diameters ranging from 1 μm to 9 μm and found similar results up to 5 μm [10]. The largest 9 μm particles presented a significant (20 mN/m) surface pressure at low compression, which was attributed to their more aggregated structure as opposed to the largely hexagonal and ordered structures

of the other particle sizes.

Studies using other experimental methods also suggest that size is not an important parameter. Taccoen *et al.* looked at the collapse of a bubble armoured with colloids ranging from 0.5 μm to 4.5 μm in diameter and found that size did not cause much variation in the collapse pressure, in agreement with their theory and work by Pitois *et al.* [15, 16]. Capillary wave experiments on larger particles ranging (in diameter) from 35 μm to 159 μm showed that the effective surface tension and stretching modulus were size-independent, although the bending stiffness was proportional to the square of the diameter [17].

Moving to much smaller particle sizes, experiments on sterically-stabilised ligand coated gold nanoparticles by Garbin *et al.* have also found the same characteristic $\Pi(A)$ shape [18]. They found that particle desorption began at $\Pi_c = 13$ mN/m, but that the response was reversible up to that point. Two sizes of nanoparticle core - 4.6 nm and 10nm diameter - were considered, with ligand size around 2.5 nm. The larger nanoparticles showed more diverse collapse phenomena, including interfacial aggregation and microphase separation - it appears particle size does make a difference here.

To summarise the effect of particle size, it has been found to make little difference to the surface pressure response of charge-stabilised particles down to around 1 μm. Although the bending stiffness has been found to increase with size for larger ($d > 35$ μm) particles, the collapse pressure of the interface seems insensitive to size in the 1-10 μm range. Smaller sizes have been found to produce anisotropic surface pressures, and there may be some effects in the nanoparticle size range.

We will now describe and present our own experiments on sterically-stabilised particles in contrast to the mostly charge-stabilised particles discussed above. We will show that while there initially seems to be a variation with sizes ranging from 0.4 μm to 2.2 μm in diameter, variation in interfacial structure is a more likely cause. We conclude that like charge-stabilised particles, size is not an important parameter over our range.

4.3 Method

Previously, in chapter 2 we described the Langmuir-Pockels trough technique and our particular apparatus, our calibration procedures, and our preparation of a particle laden interface. In chapter 3 we discussed the initial interfacial structure of the particle layer and described how we can estimate the apparent surface fraction ϕ, which we will use in this chapter. This section briefly repeats

the description of the trough experiment, then explains the details of the data processing employed here.

Langmuir-Pockels trough experiments began with initial calibration of the water-air and water-oil interfaces. Particles would then be added to the interface by pipetting a dispersion of volume fraction $\phi_v = 0.2$ % near the interface. Dispersions were either prepared for use by shaking or sonication in cold water for two 30 minute sessions at a frequency of 45kHz and a power of 80 W. The volume of dispersion added was chosen such that the particles were expected to occupy 130 cm^2 of the available 170 cm^2, corresponding to a surface fraction below that of random or ordered close packing, except for $r = 193$ nm particles where ca. 740 cm^2 of particle area was added. This was necessary to observe a surface pressure response after the given waiting period.

A waiting period of one hour was allowed, during which time the surface pressure was measured and images recorded to study the structure and estimate the surface fraction. The interface was then compressed and expanded at a constant barrier speed of 5 mm/min while imaging, and measuring the surface pressure.

The recorded surface pressure was then adjusted in two ways. First the calibration data for the bare water-dodecane was subtracted from the particle layer data. This was done with sensitivity to whether the barriers were compressing or expanding the interface - bare interface data for compression would only be subtracted from particle layer data for compression and similarly for expansion.

The final surface pressure was plotted as a function of particle surface fraction ϕ. For each interfacial area A the surface fraction was calculated from the initial surface fraction ϕ_0 by assuming that no particles desorb from the interface during compression, and that the interface remains flat. We do not use the images obtained during compression to calculate the surface fraction because the variance of the estimate from a single image is high. Given the no-desorption assumption the surface fraction follows

$$\phi_{app} = \frac{A_0}{A}\phi_0. \tag{4.1}$$

The initial surface fraction ϕ_0 was calculated by the white fraction method discussed in chapter 3. We call the surface fraction calculated from this ϕ_{app} because it is an apparent surface fraction based on the imaging. From equation 4.1 we can see that if we overestimate ϕ_0 or compress the interface to a large extent we may find that ϕ_{app} exceeds the close packing fraction or even $\phi_{app} > 1$. This situation occurs in our data and should be considered the result of our likely overestimated ϕ_0 due to the point spread function of the apparatus: see our discussion in chapter 3.

In some cases we also normalise this surface fraction to better see whether $\Pi(\phi)$ data agree. We normalise by the surface fraction ϕ_t at the initial takeoff in surface pressure - the transition between regions A and B in figure 4.1. We identify this by the point where the surface pressure exceeds a threshold value of 0.5 mN/m. Based on a peak fluctuation of 0.21 mN/m and standard deviation of 0.06 mN/m for the bare water-oil interface (see figure 2.9 in chapter 2), this is a reasonable threshold.

We also calculated the dilational elastic storage modulus from the surface pressure data. Recall that equation 1.11 from chapter 1 defined the complex modulus E^* in terms of the surface stress σ. If we assume that the surface stress σ is equal to the surface tension γ and express this equation in terms of surface pressure $\Pi = \gamma_0 - \gamma$ (where γ_0 is the bare interfacial tension) we find

$$E^* = -\frac{\mathrm{d}\Pi}{\mathrm{d}(\ln(A))}. \tag{4.2}$$

For a quasi-static compression where the strain rate is very low, the viscous response will be negligible compared to the elastic response and we will have $E^* = E'$. We assume this to be the case in our analysis of the dilational modulus. For discrete data, given the ith and $i+1$th data points, we can calculate the dilational elastic storage modulus by

$$E'_i = -\frac{\Pi_{i+1} - \Pi_i}{\ln(A_{i+1}) - \ln(A_i)}. \tag{4.3}$$

this is the dilational elastic storage modulus at a surface pressure of $\frac{1}{2}(\Pi_i + \Pi_{i+1})$ and an area of $\frac{1}{2}(A_i + A_{i+1})$. Different compression-expansion cycles are considered separately, as are compression and expansion themselves.

4.4 Results and Discussion

In this section we present the results of our Langmuir-Pockels trough measurements for three particle sizes. Having previously discussed the measurement of ϕ_{app} in chapter 3, we compare this to the use of ϕ_{app} normalised by ϕ_t in figure 4.2 to justify our use of ϕ_{app} when we present surface pressure Π as a function of ϕ_{app} for large, medium, and small particles in figures 4.4, 4.5, and 4.6 respectively. Once we have discussed the $\Pi(\phi_{app})$ of each particle size individually, we compare them in figures 4.7 and 4.8. Finally we will compare the different sizes in terms of the dilational elastic modulus E as a function of surface pressure.

Figure 4.2 compares the $\Pi(\phi)$ behaviour of three interfaces laden with the medium-sized particles after multiple compression-expansion cycles, for two methods of determining ϕ. Figure 4.2a uses an imaging method (white fraction) which was discussed in detail in chapter 3, while figure 4.2b normalises this surface fraction by the surface fraction ϕ_t where the surface pressure begins to rise.

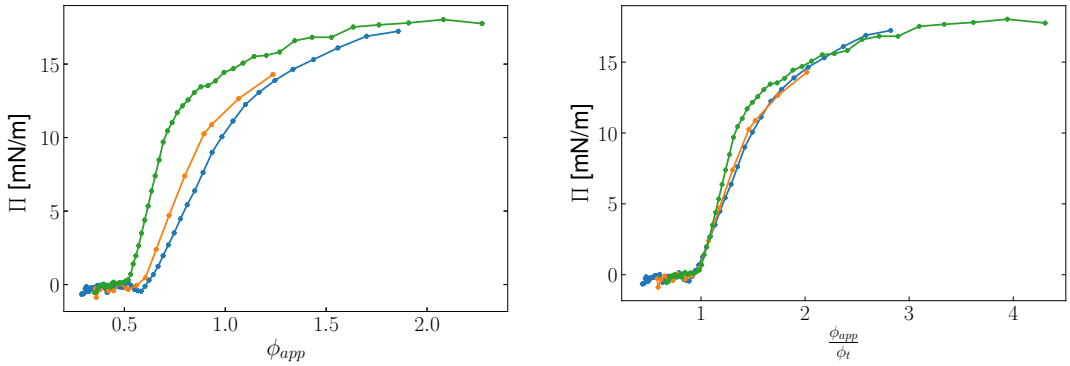

(a) **(b)**

Figure 4.2 *Surface pressure* Π *as a function of surface fraction* ϕ *for medium-sized particles in compression after several cycles of compression and expansion, with three repeats shown. The data are shown as functions of apparent surface fraction* ϕ_{app} *derived from interfacial imaging, and* ϕ_{app} *normalised by the takeoff surface fraction* ϕ_t*.*

While the agreement between samples for ϕ_{app} is not poor, it is more easily seen when normalised by ϕ_t, the surface fraction where Π begins to rise sharply. This suggests both that our measurements of ϕ_{app} could be improved, and that the reproducibility of the surface pressure response is good. Though it is useful to know that samples can be aligned by normalisation, for comparison with physical expectations we continue to use ϕ_{app} when we present the data for individual particle sizes.

4.4.1 Large Particles

We begin with the largest size, whose $\Pi(\phi_{app})$ response is shown in figure 4.4 for a number of compression cycles. As compression proceeds, particle surface fraction increases and this can be seen in figures 4.4a,4.4b and 4.4c. The typical shape for a $\Pi(\phi)$ curve is a slow increase at low ϕ (region A), giving way to a faster rise in surface pressure at higher ϕ (region B), before reaching a 'knee' in the curve (region C) and a plateau as the monolayer collapses.

Here, we observe regions A and B, but not region C because our limited

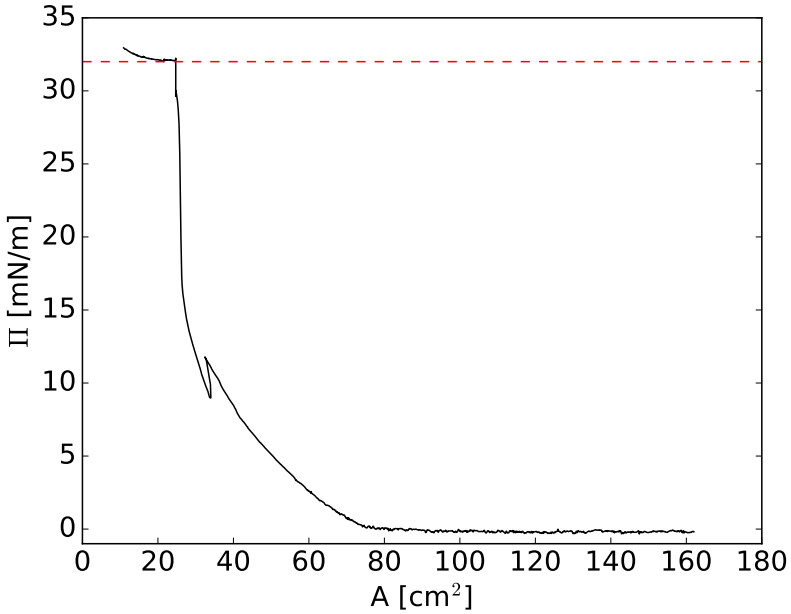

Figure 4.3 *Surface pressure* Π *as a function of trough area A for large particles in compression. The sharp feature around 30 cm*^{2} *is due to a pause in compression. The red dashed line shows the collapse pressure of 32 mN/m.*

observation window cannot access it - the trough barriers become too close and capillary effects interfere with the measurement. In other trough experiments, an example of which is shown in figure 4.3, we have observed region C to exist for large particles, with a collapse pressure of $\Pi_c = 32$ mN/m and wrinkle formation at that pressure. Wrinkles tend to form near the trough barriers, rather than uniformly across the trough, which suggests that there may be a non-uniform distribution of stress across the interface - a Janssen effect [12]. Figure 4.3 also shows that when the compression is paused the surface pressure relaxes, despite our barrier speed being as low as possible while still being practical.

Throughout the cycle of compression and expansion particles move across the field of view as a sheet or plate, until high compressions near the sharp rise in surface pressure where the motion becomes arrested. This strongly suggests that the sharp rise in surface pressure corresponds to percolation. The largest difference between cycles is between the first and second compression, with otherwise good agreement between cycles - similar to Van Hooghten *et al.* [19]. This suggests that net particle expulsion over the course of the compression/expansion is negligible [11]. It is clear from figure 4.4 that the $\Pi(\phi)$ is reproduced well with each cycle after the first.

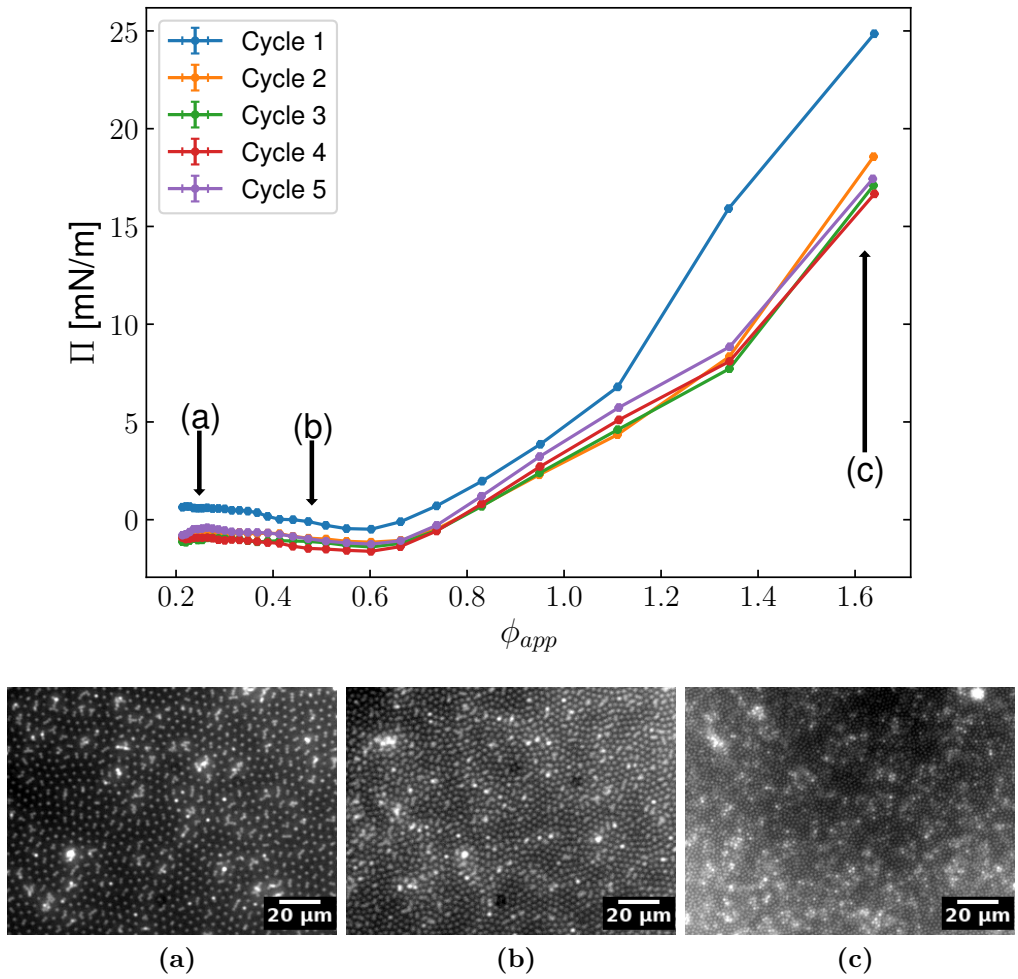

Figure 4.4 *Surface pressure* Π *as a function of apparent surface fraction* ϕ_{app} *for large particles in compression for several compression cycles. Panels (a-c) show fluorescent micrographs of the interface during the first compression at* ϕ_{app}*=0.25, 0.48, and 1.6 respectively.*

4.4.2 Medium-Sized Particles

Figure 4.5 shows the surface pressure response of the medium-sized particles, which shows regions A, B and C. Interfacial imaging in figure 4.5a shows that the initial structure is more aggregated than for large particles, as discussed in detail in chapter 3. Under compression, the particle surface fraction increases. As for large particles the surface moves, but as compression proceeds this motion slows, and this coincides with the rise in surface pressure - the beginning of region B. This is consistent with the view that region B is where particles are pushed into close contact and have limited free space to move into. Therefore the slowing of surface motion gives us an indication of when particles percolate, and that percolation coincides with a rise in surface pressure.

Moving to even higher surface fractions the 'knee' in surface pressure occurs at $\Pi_c = 12$ mN/m, far below γ_0, and we do not observe wrinkling. This suggests that another mode of pressure relief is acting to slow the rate of Π increase, for example particle expulsion or multilayer formation. The reproducibility of cycles suggests that if expulsion is the cause of the 'knee', then particles are reabsorbed during expansion. If multilayer formation was the cause, we would expect a substantial shift in the point where particles interact, and we would not expect reproducibility. Therefore, currently the mode of yielding which causes the 'knee' to occur at $\Pi_c = 12$ mN/m is unclear.

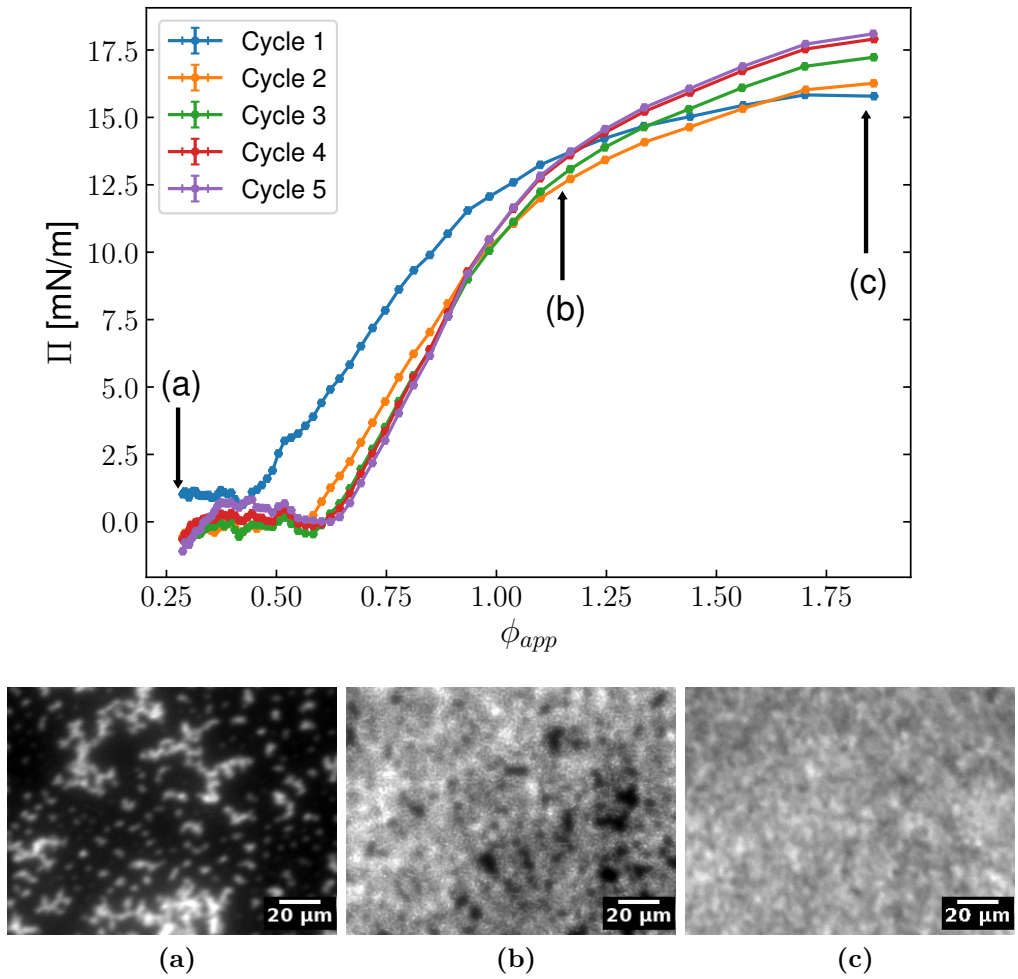

Figure 4.5 *Surface pressure* Π *as a function of apparent surface fraction* ϕ_{app} *for medium-sized particles in compression for several compression cycles. Panels (a-c) show fluorescent micrographs of the interface during the first compression at* ϕ_{app}*=0.28, 1.2, and 1.8 respectively.*

4.4.3 Small Particles

The surface pressure response of the smallest particles is shown in figure 4.6, and images at various stages of the compression are given in figures 4.6a, 4.6b and 4.6c. In the $\Pi(\phi_{app})$ plot we can see regions A, B and C, but also a curious dip in surface pressure between A and B. This dip is most pronounced for our smallest particle size, but it is also visible in figure 4.4 and 4.5 around $\phi_{app} = 0.6$. The source of the dip is not clear and does not coincide with any visible changes. One possible explanation is that as particles approach they experience weak attraction, before further compression causes them to repel each other and increase the surface pressure. As the surface pressure rises surface motion does not visibly slow, unlike medium-sized particles. This is surprising, because we expected percolation to occur and to force particles into strong interaction before the surface pressure could rise. One explanation could be the limited view of the interface: loose percolation could mean that the interface is only locally mobile.

The curves become very similar after a number of cycles, and the 'knee' for the last few cycles occurs at Π_c =8 mN/m. No wrinkling was observed, so we must consider whether particles are expelled during compression. As for medium-sized particles, the last few cycles agree well so there is unlikely to be significant net particle expulsion. Again, the mode of yielding is unclear.

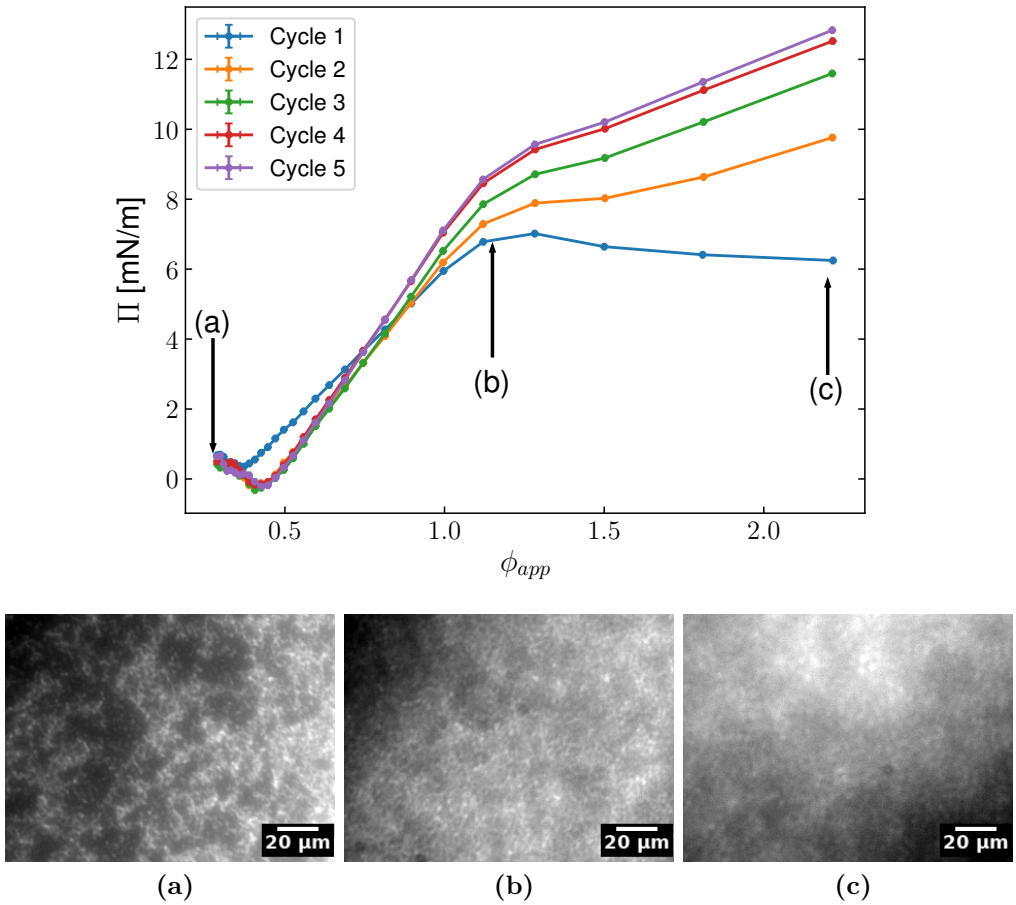

Figure 4.6 *Surface pressure* Π *as a function of apparent surface fraction* ϕ_{app} *for small particles in compression for several compression cycles. Panels (a-c) show fluorescent micrographs of the interface during the first compression at* ϕ_{app}*=0.27, 1.2, and 2.2 respectively.*

4.4.4 Comparison of Particle Sizes

We compare the last compression for the three particles sizes as a function of ϕ_{app} in figure 4.7. The trend with particle size is not immediately clear. Medium sized particles transition to region B first, followed by the smallest particles, then the largest. Although the limited observation window obscures region C for the largest particles the collapse pressure was found in other experiments to be $\Pi_c = 32$ mN/m. Table 4.1 summarises the collapse pressures for each particle size. This clearly shows a decrease in collapse pressure as size decreases. This trend is consistent with expectations for either particle desorption or multilayer formation: particle desorption energy scales as r^2 (see chapter 1) and the energy cost of interfacial deformation required to form multilayers will also decrease with particle size.

Further, because Π only rises slowly after the collapse, this means that the maximum surface pressure generated by particles decreases significantly with decreasing particle size. This may have consequences for the ease of formation of Pickering emulsions: smaller particles cannot lower the interfacial tension as much as larger particles, and so it would take more work to generate a Pickering emulsion with small particles. As discussed in the introduction, the literature on charge-stabilised particles shows little variation with particle size, so this result is surprising. Given that desorption energy decreases with the square of the particle diameter, we might be tempted to explain the decreasing collapse pressure with particle size by the increasing ease of expulsion. However, the collapse pressure decreases more slowly than one would expect if that were the driving factor.

As discussed above and shown in figure 4.2, instead of calculating ϕ_{app} we can plot the surface pressure as a function of ϕ_{app}/ϕ_t to understand whether different samples agree. Figure 4.8 shows $\Pi(\phi_{app}/\phi_t)$. We can see that the agreement between samples is good by the narrow error bars, so our results are reproducible. Instead of concerning ourselves with the surface fraction, we can plot the

Particle size	Collapse Pressure Π_c [mN/m]
Large, $r = 1260$ nm	32
Medium, $r = 450$ nm	12
Small, $r = 193$ nm	8

Table 4.1 *Collapse pressures for different particle radii r, measured by static light scattering.*

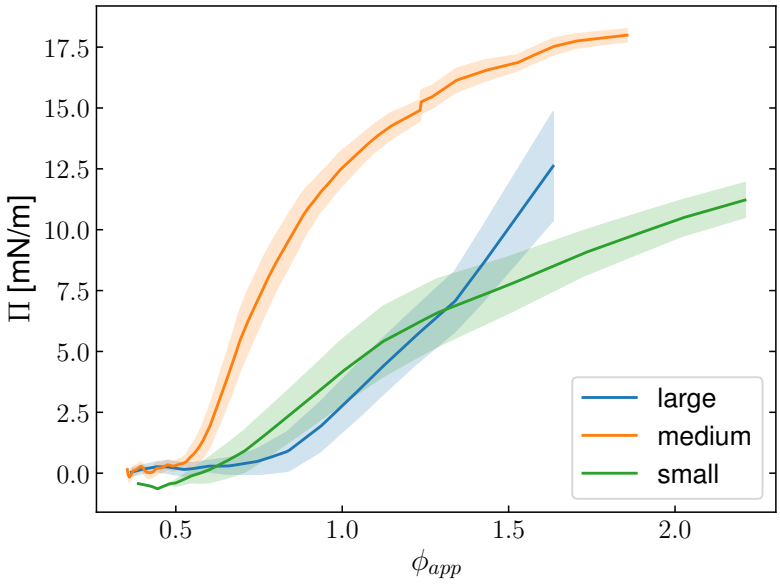

Figure 4.7 *Surface pressure* Π *as a function of apparent surface fraction* ϕ_{app} *for three particle sizes in compression after several compression and expansion cycles. Error bars are indicated by the shaded region of each curve.*

dilational elastic storage modulus E' as a function of surface pressure. If there is a one-to-one relationship between surface pressure and surface fraction, each sample should reproduce the same $E'(\Pi)$ curve and allow us to compare the measurements without concerning ourselves with the accuracy of the measured surface fraction. Figure 4.9 shows this for the three particle sizes, and shows that each particle size is producing a different response - the differences are not an artefact of the surface fraction measurement.

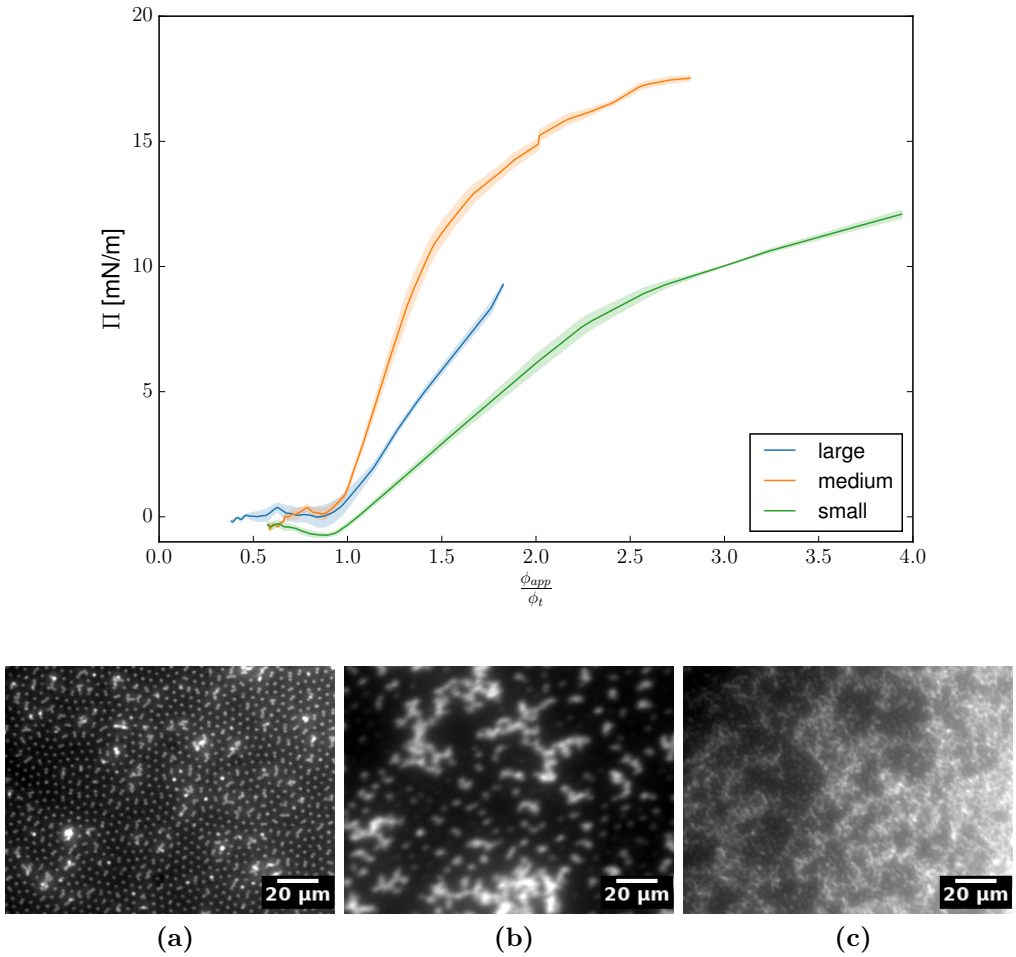

Figure 4.8 *Surface pressure* Π *as a function of apparent surface fraction* ϕ_{app} *normalised by the surface fraction at takeoff* ϕ_t *for three particle sizes in compression after several compression and expansion cycles, and initial micrographs at* $\phi_{app} = \phi_0$ *for a) large, b) medium, and c) small particles. Error bars are indicated by the shaded region of each curve.*

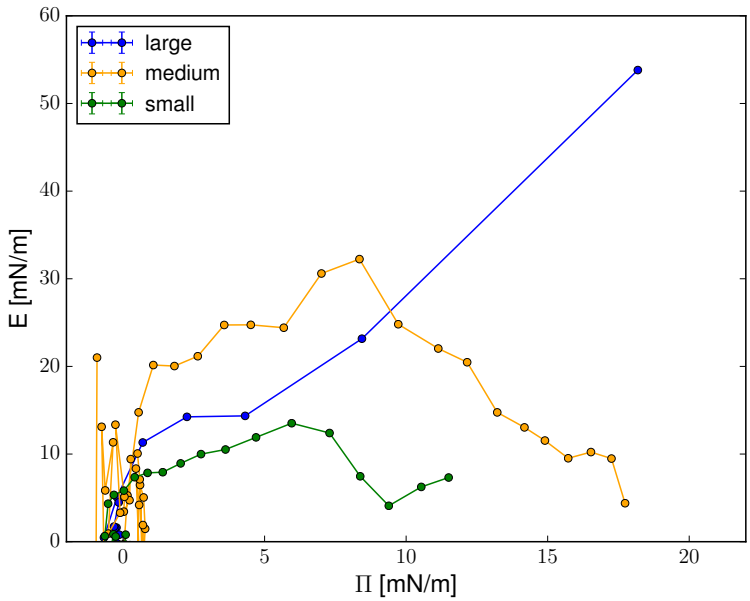

Figure 4.9 *Dilational elastic storage modulus E' as a function of surface pressure Π for three particle sizes in compression after several compression and expansion cycles.*

4.4.5 The Effect of Sonication

Having discussed the variation with particle size for dispersions prepared without sonication immediately prior to addition to the interface, we now turn to the sonicated dispersions. Figure 4.10 shows the first compression for the three particle sizes as $\Pi(\phi_{app}/\phi_t)$, along with the initial structure for each size. Comparing these data to figure 4.8 we see that the surface pressure response is much more similar for all particle sizes, in agreement with the literature on charge-stabilised particles. Also, we can again avoid the problem of determining the surface fraction ϕ by plotting the dilational storage modulus E' as a function of Π in figure 4.11. Comparison with figure 4.9 again shows that the response for all particle sizes are much more similar.

To understand the difference between sonicated and unsonicated dispersions, we should consider the initial interfacial structures. Figure 4.8 shows snapshots of the initial structures for each size for sonicated dispersions. It is difficult in this case to find images which are not motion blurred but even so, comparing these to figure 4.8 we can see that they are much more homogeneous. In chapter 3 we saw that structure and size were not independent for unsonicated dispersions, with smaller particles aggregating more. Now that size and structure are less dependant, we observe much more similar surface pressure responses up to the

'knee'. This suggests that the differences in aggregation state are the primary cause of the variation with size we saw in figures 4.8 and 4.9.

This result aligns with previous observations - Reynaert *et al.* explored the effect of aggregation on charge-stabilised particles by adding electrolyte. They found that decreased repulsion led to aggregation and reduced surface pressure and collapse pressures [20], in agreement with our results. However as Petkov *et al.* point out, although electrolytes reduce surface charge, aggregates have a higher charge and repel each other more strongly. For their system this lead to a net increase in surface pressure with aggregation [21]. In our case, it is unclear whether sonication modulates the repulsion between particles, through charging the particles by the triboelectric effect for example, or instead breaks up aggregates which are slow to form. Triboelectric effects are hypothesised to be the cause of residual charges formed when spreading polystyrene particles at an oil/water interface, and these charges were only compensated over a matter of several hours, so it is not inconceivable that this could occur here [22, 23].

Whatever the cause, it is clear that sonication has a strong effect on the structure and surface pressure response for this system. This result may find application in microstructural control - vital for applications of particle assembly at interfaces [2, 24] - where other methods of control such as added electrolytes may be undesirable.

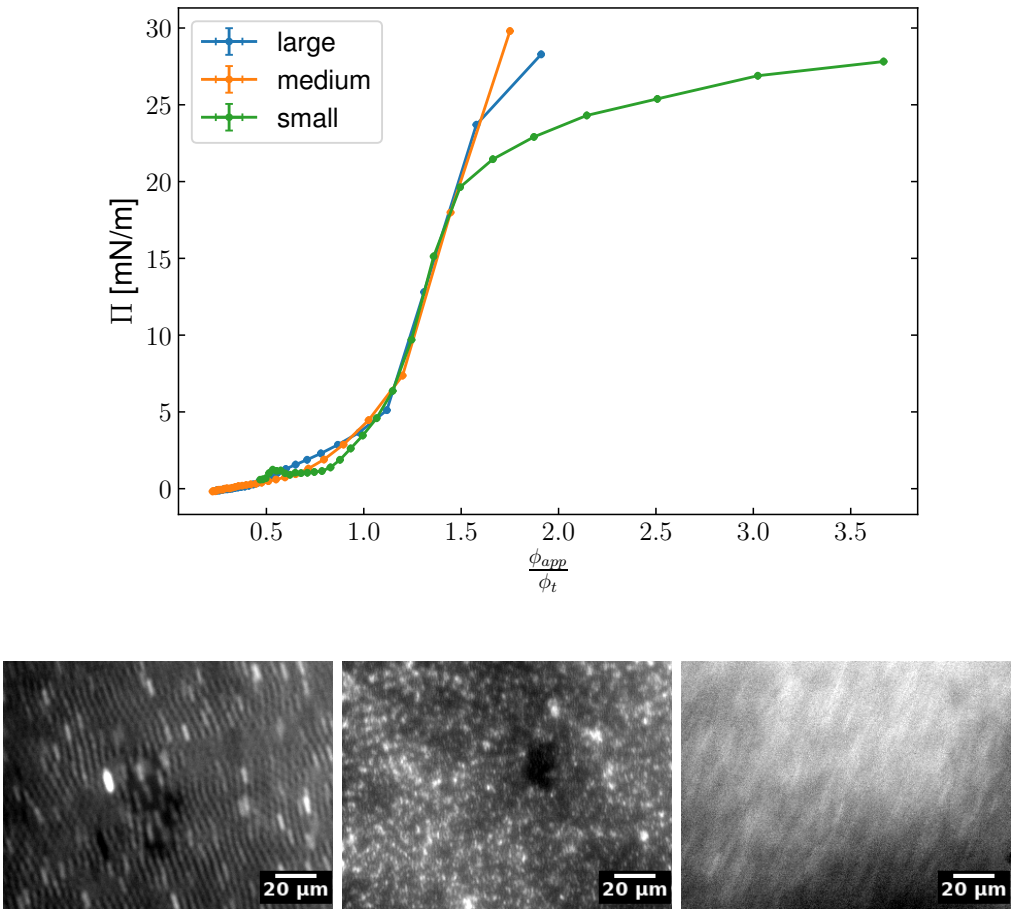

Figure 4.10 *Surface pressure* Π *as a function of apparent surface fraction* ϕ_{app} *normalised by the surface fraction at takeoff* ϕ_t *for three particle sizes for the first compression, and initial micrographs at* $\phi_{app} = \phi_0$ *for a) large, b) medium, and c) small particles. Particles were dispersed by sonication immediately before use.*

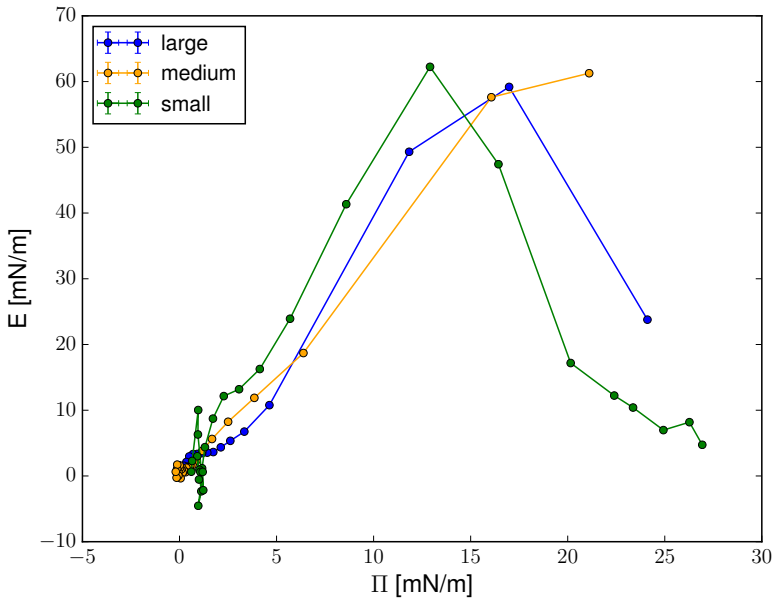

Figure 4.11 *Dilational elasticity E as a function of surface pressure Π for three particle sizes under the first compression. Particles were dispersed by sonication immediately before use.*

4.5 Conclusions

In this chapter we have explored the surface pressure response $\Pi(\phi)$ for three different sizes of sterically-stabilised particles in a Langmuir trough. Dispersions were prepared either by simply shaking the dispersion, or by sonication. We found that the characteristic response of each case was similar to what other authors have observed for charge-stabilised particles. While $\Pi(\phi)$ initially appeared to change with particle size, by comparing this variation with the lack of variation seen in sonicated samples, it seems that aggregation state is a much more important factor - a potentially useful finding for the control of particle assembly. For the sonicated samples where the interfacial structures were more homogeneous and comparable, particle size was found to be unimportant over the diameter range 0.4 μm to 2.2 μm, consistent with previous reports on charge-stabilised particles.

Bibliography

[1] Job HJ Thijssen and Jan Vermant. Interfacial rheology of model particles at liquid interfaces and its relation to (bicontinuous) pickering emulsions.

Journal of Physics: Condensed Matter, 30(2):023002, 2017.

[2] Nicolas Vogel, Markus Retsch, Charles-Andre Fustin, Aranzazu del Campo, and Ulrich Jonas. Advances in colloidal assembly: the design of structure and hierarchy in two and three dimensions. *Chemical reviews*, 115(13):6265–6311, 2015.

[3] Kan Du, Elizabeth Glogowski, Todd Emrick, Thomas P Russell, and Anthony D Dinsmore. Adsorption energy of nano-and microparticles at liquid- liquid interfaces. *Langmuir*, 26(15):12518–12522, 2010.

[4] Yi Zhang, Songcheng Wang, Jiarun Zhou, Ruiyang Zhao, Gregory Benz, Stephane Tcheimou, J Carson Meredith, and Sven H Behrens. Interfacial activity of nonamphiphilic particles in fluid–fluid interfaces. *Langmuir*, 33(18):4511–4519, 2017.

[5] Robert Aveyard, John H Clint, Dieter Nees, and Vesselin N Paunov. Compression and structure of monolayers of charged latex particles at air/water and octane/water interfaces. *Langmuir*, 16(4):1969–1979, 2000.

[6] Sebastian Uppapalli and Hui Zhao. The influence of particle size and residual charge on electrostatic interactions between charged colloidal particles at an oil–water interface. *Soft Matter*, 10(25):4555–4560, 2014.

[7] Valeria Garbin. Collapse mechanisms and extreme deformation of particle-laden interfaces. *Current opinion in colloid & interface science*, 39:202–211, 2019.

[8] Robert Aveyard, John H Clint, Dieter Nees, and Nick Quirke. Structure and collapse of particle monolayers under lateral pressure at the octane/aqueous surfactant solution interface. *Langmuir*, 16(23):8820–8828, 2000.

[9] Zoltán Hórvölgyi, Sándor Németh, and Janos H Fendler. Monoparticulate layers of silanized glass spheres at the water- air interface: particle- particle and particle- subphase interactions. *Langmuir*, 12(4):997–1004, 1996.

[10] Cécile Monteux, John Kirkwood, Hui Xu, Eric Jung, and Gerald G Fuller. Determining the mechanical response of particle-laden fluid interfaces using surface pressure isotherms and bulk pressure measurements of droplets. *Physical Chemistry Chemical Physics*, 9(48):6344–6350, 2007.

[11] Sepideh Razavi, Kathleen D Cao, Binhua Lin, Ka Yee C Lee, Raymond S Tu, and Ilona Kretzschmar. Collapse of particle-laden interfaces under compression: buckling vs particle expulsion. *Langmuir*, 31(28):7764–7775, 2015.

[12] Pietro Cicuta and Dominic Vella. Granular character of particle rafts. *Physical review letters*, 102(13):138302, 2009.

[13] John H Clint and Spencer E Taylor. Particle size and interparticle forces of overbased detergents: a langmuir trough study. *Colloids and surfaces*, 65(1):61–67, 1992.

[14] Jiro Kumaki. Monolayer of polystyrene monomolecular particles on a water surface studied by langmuir-type film balance and transmission electron microscopy. *Macromolecules*, 21(3):749–755, 1988.

[15] Nicolas Taccoen, François Lequeux, Deniz Z Gunes, and Charles N Baroud. Probing the mechanical strength of an armored bubble and its implication to particle-stabilized foams. *Physical Review X*, 6(1):011010, 2016.

[16] Olivier Pitois, Matthieu Buisson, and Xavier Chateau. On the collapse pressure of armored bubbles and drops. *The European Physical Journal E*, 38(5):48, 2015.

[17] Carole Planchette, Elise Lorenceau, and Anne-Laure Biance. Surface wave on a particle raft. *Soft Matter*, 8(8):2444–2451, 2012.

[18] Valeria Garbin, John C Crocker, and Kathleen J Stebe. Forced desorption of nanoparticles from an oil–water interface. *Langmuir*, 28(3):1663–1667, 2011.

[19] Rob Van Hooghten, Victoria E Blair, Anja Vananroye, Andrew B Schofield, Jan Vermant, and Job HJ Thijssen. Interfacial rheology of sterically stabilized colloids at liquid interfaces and its effect on the stability of pickering emulsions. *Langmuir*, 33(17):4107–4118, 2017.

[20] Sven Reynaert, Paula Moldenaers, and Jan Vermant. Control over colloidal aggregation in monolayers of latex particles at the oil- water interface. *Langmuir*, 22(11):4936–4945, 2006.

[21] Plamen V Petkov, Krassimir D Danov, and Peter A Kralchevsky. Monolayers of charged particles in a langmuir trough: Could particle aggregation increase the surface pressure? *Journal of colloid and interface science*, 462:223–234, 2016.

[22] Peng Gao, Zonglin Yi, Xiaochen Xing, To Ngai, and Fan Jin. Influence of an additive-free particle spreading method on interactions between charged colloidal particles at an oil/water interface. *Langmuir*, 32(19):4909–4916, 2016.

[23] Peng Gao, XiaoChen Xing, Ye Li, To Ngai, and Fan Jin. Charging and discharging of single colloidal particles at oil/water interfaces. *Scientific reports*, 4:4778, 2014.

[24] Valeria Garbin, John C Crocker, and Kathleen J Stebe. Nanoparticles at fluid interfaces: Exploiting capping ligands to control adsorption, stability and dynamics. *Journal of colloid and interface science*, 387(1):1–11, 2012.

Chapter 5

Dilational Interfacial Rheology by Oscillating Pendant Drop Measurements

5.1 Abstract

In the previous chapter we explored the dilational rheology of three sizes of particle at the water-dodecane interface by using the Langmuir-Pockels trough. We found that size made little difference if particle dispersions were sonicated immediately before use. In this chapter, we use the oscillating pendant drop method to explore the dilational rheology of our smallest particles. We find that the rheology is dominated by the elasticity, and that the dilational elastic modulus is proportional to the surface pressure. Application of the theory we developed in chapter 1 suggests that our sterically-stabilised particles interact as charged particles do, and that screened monopole behaviour is a likely explanation.

5.2 Introduction

Previously, in chapter 1 we described a thermodynamic approach to model the effect of colloid adsorption and interaction on the surface pressure. In chapter 4 we described the experimental literature on colloid surface pressure and showed that size (over our range) is not an important parameter for the mechanical response, but we refrained from a more quantitative discussion of the data. In this chapter we conduct oscillating pendant drop experiments and compare the results in detail to the literature. In the next chapter, we will compare our

oscillating pendant drop and Langmuir-Pockels trough results.

A few studies have attempted a quantitative explanation of surface pressure in terms of particle interactions. Aveyard *et al.* modelled the interaction of charged particles and their image charges to explain the initial increase in surface pressure at large area [1], predicting that Π should scale with the area fraction $\phi = A_p/A$ (with $A_p = Na_p$ for N particles of cross-sectional area a_p at the interface) as $\Pi \propto \phi^{5/2}$. More recently, Kralchevsky *et al.* [2] found that their surface pressure asymptotically scaled as $\Pi \propto \phi^{3/2}$, and explained this by expanding the model used by Aveyard *et al.* to include collective effects. Garbin *et al.* used Brownian dynamics simulations with steric interactions (modelled by an exponentially decaying repulsive potential) to analyse their pendant drop measurements on ligand-grafted gold nanoparticles [3]. While they did not express the ϕ dependence of the surface pressure analytically, we argue later in section 5.4.1 that this can be predicted from the interaction potential and by this method we would find $\Pi \propto \exp\left((\phi^{-1/2} - 2R)/L_G\right)$ for particle radius R and interaction decay length L_G.

However, Du *et al.* [4] modelled the surface pressure changes as caused by adsorption (wetting) alone, and this model was found to agree with data for a range of different colloid systems by Zhang *et al.* [5], though the agreement is somewhat surprising given the high surface fractions of around $\phi = 0.9$ they achieved. Yet Hua *et al.* also found that an adsorption-only model was sufficient to describe the effect of nanoparticles on the surface pressure [6, 7]. In the adsorption only model, a scaling of $\Pi \propto \phi$ is expected.

These models, which each agree with their own data, produce different scalings with area fraction ϕ (or equivalently, surface concentration or adsorption Γ), and are compared in table 5.1. Typically, trough measurements are modelled with interactions alone, while pendant drop measurements are modelled with adsorption alone. An exception to this is [3]. In that case the pendant drop was compressed with a constant number of adsorbed particles - as occurs in a Langmuir-Pockels trough - in contrast to references [4–7] where the interfacial tension was observed at a given drop volume, after some equilibration time. Thus the trend appears to be that for fixed particle number we observe only the effect of interactions, while when allowing the particle number to vary and equilibrate we observe only the effect of adsorption. This is consistent with our discussion in chapter 1, and shows how different aspects of interfacial behaviour may be measured depending on the experimental conditions.

Given the suspected dependence on conditions, specifically the timescale of

Reference	System and Method	Model Type	Π scaling
Aveyard *et al.*[1]	Polystyrene at air/water and octane/water interfaces, Langmuir-Pockels trough.	Interactions between charged particles at an interface only.	$\phi^{5/2}$
Kralchevsky *et al.*[2]	Silica at air/water, Langmuir-Pockels trough.	Interactions + collective effects only.	$\phi^{3/2}$
Garbin *et al.* [3]	Ligand-grafted gold nanoparticles, pendant drop.	Interactions only.	N/A
Du *et al.*[4]	Gold nanoparticles and polystyrene particles at OFPA/water and fluorohexane/water, pendant drop tensiometry.	Adsorption only.	ϕ
Zhang *et al.*[5]	Silica at air/water, ethyl cellulose at hexadecane/water and TMPTMA/water, pendant drop tensiometry.	Adsorption only.	ϕ
Hua *et al.*[6, 7]	Gold nanoparticles at toluene/water, pendant drop tensiometry.	Adsorption only.	ϕ

Table 5.1 *Comparison of area fraction ϕ scalings of different models for the effect of colloidal particles on surface pressure* Π.

measurement and whether the number of particles adsorbed changes over that timescale, we sought to investigate the frequency response of the system.

The frequency response of interfacial systems can provide insight into the relaxation processes at the interface. Liggieri *et al.* used several experimental methods to probe silica particles (diameter around 30nm[1]) and a cationic surfactant (hexadecyltrimethylammonium bromide, CTAB) which adsorbed to the particle surface. They measured the dilational modulus for a wide range of frequencies from 10^{-3} Hz 10^{3} Hz [8], and attributed a process with a characteristic frequency of around 0.1 Hz to particle behaviour. Bykov *et al.* also concluded that their charge-stabilised 1μm particles adsorbed to the water-air interface demonstrated a characteristic time around 10s (so a frequency of 0.1 Hz) [9]. They note that reversible 2D aggregation is one possible explanation and that a similar model was used for the globular hydrophobin HFBII [10]. Here, we use the frequency response to compare our system to these earlier studies and to explore the relaxation processes present.

While Liggieri *et al.* and Bykov *et al.* found that the interface was predominantly elastic ($E' \gg E''$), Kobayashi and Kawaguchi focused on frequencies around 10^{-3} Hz and found that the dilational storage modulus overtook the dilational loss modulus above a frequency of 0.01 Hz, for larger particles with diameters around 400nm at the water-air interface [11] which were sterically-stabilised with diacetone acrylamide (DAAM). For higher frequencies, the elastic modulus seemed to reach a plateau around 50 mN/m, while the loss modulus approached 14 mN/m.

Particles at the water-oil interface were found to demonstrate a lower elasticity and lower sensitivity to salt than at the water-air interface, which was attributed to a difference in contact angle or particle surface charge on the oil side [12].

5.3 Method

5.3.1 Elasticity Changes over Time

This section describes the procedures used to collect elasticity and surface pressure data as particles adsorb to a pendant drop. We previously introduced the technique, described the apparatus and its calibration in chapter 2.

The particles (batch ASM530, r = 193nm) are first dispersed in n-dodecane (Acros Organics, 99% pure) to a volume fraction of 0.2% measured by drying

[1] It is unclear whether aggregates were present.

samples, which is sufficient for our purposes [13]. The mixture is shaken, then sonicated for at least 30 minutes at 45 kHz and 80 W to ensure good dispersion. The n-dodecane was purified before use by filtration of a 1 L batch through a 25 cm×4 cm alumina (Honeywell, Aluminium Oxide, activated, basic, Brockmann I) column three times. Water was distilled, then deionised to a resistivity of 18 MΩ.cm and degassed by heating and stirring under reduced pressure for one hour. This eliminates bubbles which may disrupt volume oscillations.

To clean the system, glassware was first soaked overnight in 1 M NaOH, rinsed thoroughly with distilled water and ethanol, then dried and put to use. Between experiments the glass cuvette and the needle tip were sonicated for 15 minutes in toluene (Fisher, Analytical Reagent Grade) at 30 kHz and 80 W to dissolve the PHSA/PMMA particles, then rinsed thoroughly with ethanol (Fisher, Analytical Reagent Grade) and dried before use.

To measure the elastic modulus and surface pressure as a function of time for a particle-laden interface, we first formed a water drop in the 0.2% volume fraction dispersion of particles, then immediately applied 10s period oscillations at amplitude of 4% area strain continuously throughout the experiment. Approximately every 10 minutes, we recorded 100s of video with a sampling frequency of 10 frames per second. We took the mean surface pressure in each video to be the surface pressure at the time the recording began.

The elastic modulus was calculated from the interfacial tension $\gamma(t)$ and surface tension $A(t)$ data using an approximation valid to first order in $\Delta A/A_m$, which was described in chapter 2.

Finally, the presence of a particle film was demonstrated by withdrawal of water from the drop until the surface showed wrinkles.

5.3.2 Frequency Response

For oscillating drop experiments where the frequency was varied to explore the dilational elasticity response, some droplets were prepared as described above in §5.3.1 and probed one day after formation. Alternatively they were prepared using particles of batch ASM261, $r = 208$nm (to explore batch to batch variation) dispersed in hexane and added near the base of the drop. The volume fraction dispersion of the hexane dispersion was 13%, and the drops were allowed to equilibrate for two days before measurement.

The frequency was varied in a range from 0.010Hz to 0.34Hz, with multiple measurements being taken at each point to gauge variation.

5.4 Results and Discussion

5.4.1 Elasticity Changes over Time

Over a timescale of several hours both the surface pressure Π and storage modulus E' increase, while the loss modulus E'' remains low, as shown in figures 5.1 and 5.2. The dominant storage modulus is typical for colloids at interfaces [14], though previous investigations most often use charge-stabilised colloids. Both Π and E show a clear transition from a fast regime to a slower regime. The surface pressure transition occurs around $\Pi = 7.5$ mN/m and a time $t = 250$ min after drop formation, while the transition in the storage modulus occurs around $E' = 22$ mN/m, $t = 300$ min. The long timescales involved are necessary to ensure that no significant E or Π changes occur over the oscillation timescale. Changes in E or Π over the measurement time of one data point are typically smaller than 0.1 mN/m, and are considered insignificant.

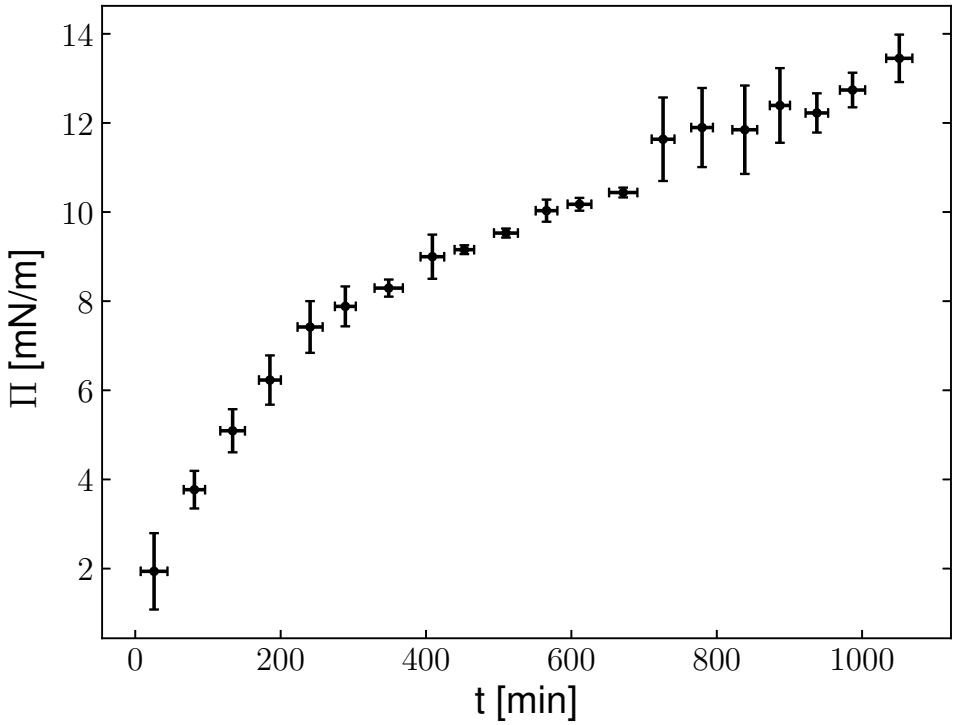

Figure 5.1 *Surface pressure* Π *during the adsorption of ASM530,* $R = 193nm$ *particles to a water/n-dodecane interface as a function of time t after drop formation.* Π *error bars are estimated from sample-to-sample variation, which dominates the instrument error of around 0.1 mN/m. Time error bars arise from the binning of samples.*

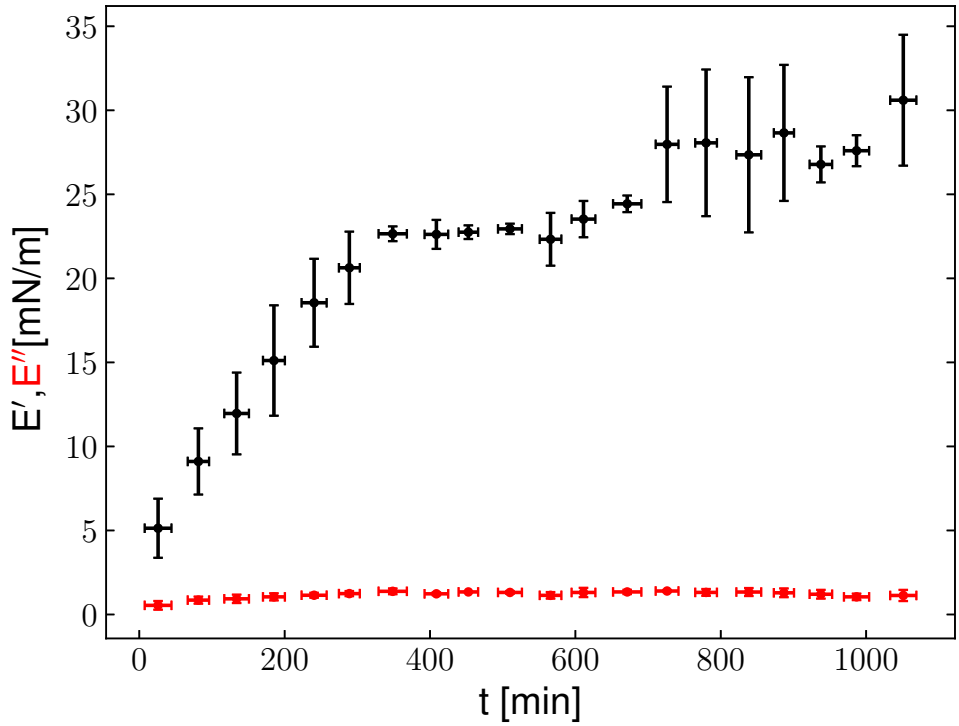

Figure 5.2 *Dilational storage modulus E' and loss modulus E'' during the adsorption of ASM530, $R = 193nm$ particles to a water/n-dodecane interface as a function of time t after drop formation. E error bars are estimated from the sample-to-sample variation. Time error bars arise from the binning of samples.*

Figure 5.3 shows the measured storage modulus E' as a function of surface pressure Π. The data form an approximately linear relationship with a gradient of 2.36±0.17. However there is a small but visible sharp change around $\Pi = 8$ mN/m, the point in time where a transition in both E and Π occurs, which we do not fully understand. A plausible explanation is that particle adsorption has been slowed by the blocking effect of already adsorbed particles.

This differs from the simple model introduced by Du *et al.* [4] where $\Pi \propto \phi$, which yields the same result as the grand canonical ensemble approach we described in chapter 1 if we take the adsorption energy of a single particle to be defined from equation (1.13). From equation (1.11), assuming the elastic modulus is dominant we have

$$E' = \frac{\mathrm{d}\gamma}{\mathrm{d}(\ln(A))}. \tag{5.1}$$

Assuming no desorption over the measurement timescale allows us to say $\mathrm{d}\ln(A) = -\mathrm{d}\ln(\phi)$. Also using the definition of surface pressure $\Pi = \gamma_0 - \gamma$

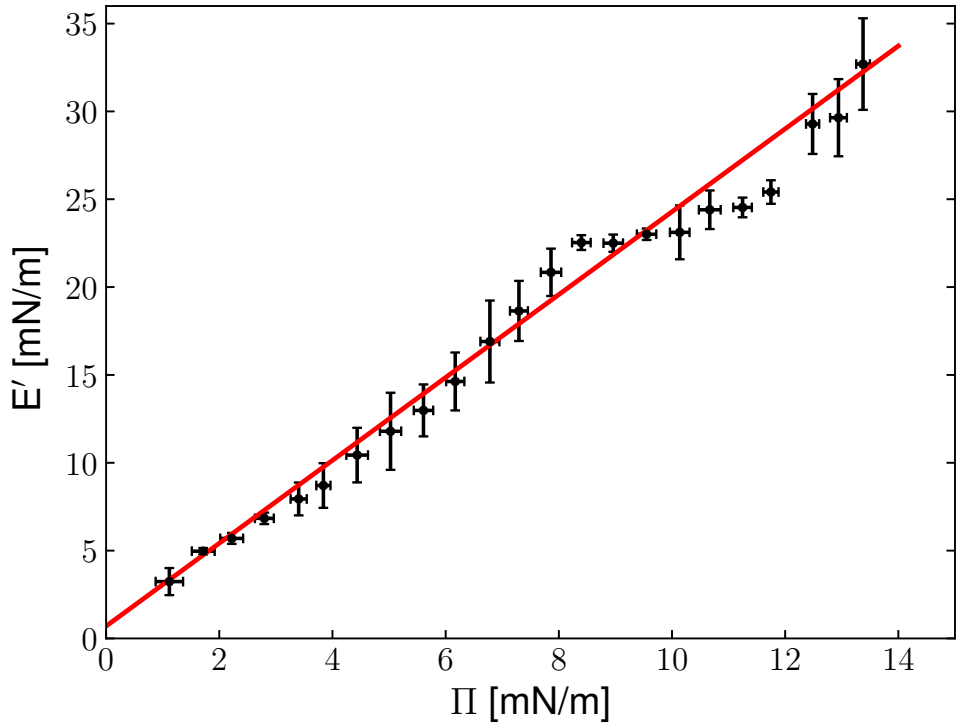

Figure 5.3 *Plot of the storage modulus E' vs surface pressure Π obtained during the adsorption of ASM530, $R = 193nm$ particles to a water/n-dodecane interface.*

gives

$$E' = \frac{\mathrm{d}\Pi}{\mathrm{d}(\ln(\phi))}. \tag{5.2}$$

Substitution of $\Pi \propto \phi$ into equation yields $E' = \Pi$ i.e. the adsorption model of Du *et al.* predicts a gradient of 1 for the $E(\Pi)$ plot, while our gradient is 2.36±0.17. Given that adsorption energies for this system are $\mathcal{O}(10^5)$kT compared to interaction energies of $\mathcal{O}(10^3)$kT (using equation (1) of [15] for a few microns of separation) without our discussion in chapter 1 we might have expected adsorption to dominate, and the gradient to be close to 1. But as we noted in section 1.4.5, adsorption will not contribute to the surface pressure if the system can be modelled by the canonical ensemble i.e. when particle number is constant over the timescale of measurement. The authors using pendant drop tensiometry, summarised in table 5.1, measured the surface pressure after particles had adsorbed so particle number could not be constant.

We can now apply the canonical ensemble approach to understand our results in terms of interparticle interaction pair potentials, which we discussed in section

1.4.2. Expressing equation (1.40) in terms of the surface fraction $\phi = a_p\rho$ of particles of cross sectional area a_p gives

$$\Pi_F = \frac{\phi^2}{a_p}\left(\frac{\partial \bar{u}_p}{\partial \phi}\right)_{A,T}. \tag{5.3}$$

To connect the mean internal energy per particle to the pair potential $U(r)$ for a separation r, we assume an interfacial structural arrangement. For simplicity we use a hexagonal lattice. Then the surface fraction ϕ scales as $\phi \propto r^{-2}$. Further, since a number of important potentials discussed in section 1.4.2 follow a power law, let us say that $U(r) \propto r^{-2\lambda}$ so that $U(\phi) \propto \phi^{\lambda}$. Considering only the Q nearest neighbour pair interactions, the mean internal energy per particle is then

$$\bar{u}_p = \frac{Q}{2}U(\phi) \propto \phi^{\lambda}. \tag{5.4}$$

Using equations 5.4, 5.3, and 5.2 we find that

$$E = (1+\lambda)\Pi \tag{5.5}$$

so the gradient of the $E(\Pi)$ plot reflects the density scaling of the pair interaction potential. As an example, the dipole interaction term in equation 1.16 scales as r^{-3} and therefore gives $(1+\lambda) = 2.5$. We see that a linear relationship with a gradient of 2.36±0.17 can be explained by a power law relationship for the particle-particle interaction energy $\epsilon_i(\phi) \propto \phi^{1.36\pm0.17}$. As discussed above, what this means for the scaling of interparticle potential energies with interparticle distance r depends on the structural arrangement of the particles at the interface. Assuming a hexagonal packing of particles, we find $\epsilon_i(r) \propto 1/r^{2.8\pm0.3}$, which is consistent with a dipolar interaction.

However, from the work of Muntz *et al.* we will see that a screened monopole term can also explain our data. Muntz *et al.* recently studied the interfacial interaction of $R \approx 1$ μm PHSA-PMMA particles by using a blinking optical trap and the radial distribution function extracted from fluorescence microscopy images [15]. They found that the screened monopole term of equation 1.16 (with a fitted screening length) was sufficient to explain their data, and that the dipole term was negligible. Using only the monopole term in equation 1.16 with the parameters used by Muntz *et al.* of $a_1 = 4136$ and inverse screening length $\kappa = 0.35$ μm^{-1}, we find that the resulting E' vs Π plot shown in figure 5.4 appears surprisingly linear given the exponential decay of the screening effect. The gradient of 2.66 is slightly outside error of our measured 2.36±0.17, but is plausible if we allow

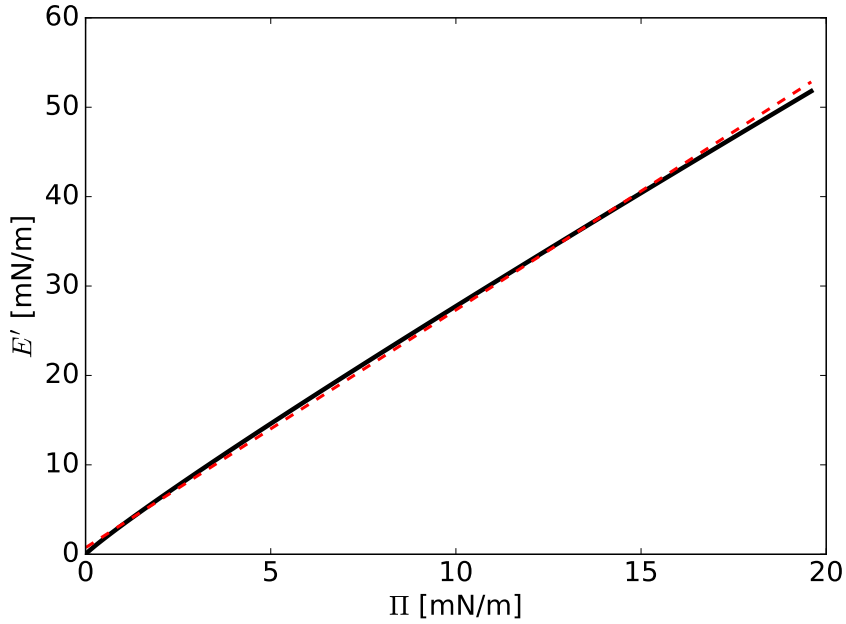

Figure 5.4 *Calculated dilational storage modulue E' and surface pressure Π calculated using only a screened monopole term, using the parameters reported by Muntz et al. described in the text, for a range of surface fractions from $\phi = 0$ to $\phi = 0.1$. The red dashed straight line fit to the data has a gradient of 2.66.*

even small variations for particle size and batch. We calculated E' and Π for ϕ values ranging from zero to $\phi = 0.1$, assuming a hexagonal lattice. At the highest surface fraction of $\phi = 0.1$, the interparticle distance $D \approx 6R$, so since the screening length is $1/\kappa \approx 3R$ particles are outside the screening length for all considered densities.

From the above we can say only that the interaction is not inconsistent with a interfacial charged particles. These sterically-stabilised particles are not expected to be charged, yet they interact as charged particles do at the interface. However, connecting particle pair potentials to the average particle interaction energy ϵ_i is not straightforward, as illustrated by Kralchevsky *et al.*[16].

Because E can be defined in terms of Π and ϕ (by equation (5.5)), we are effectively probing the $\Pi(\phi)$ relationship by measuring the $E(\phi)$ relationship. This circumvents the need to measure ϕ, which can be practically difficult, particularly on the curved interface of a droplet.

We can make a comparison with previous work on charge-stabilised particles by considering the scaling of Π: using equation (5.3) we can say $\Pi = \alpha\phi^{2.36}$ and $E = 2.36\alpha\phi^{2.36}$, or in terms of interfacial area A then $\Pi = \alpha' A^{-2.36}$ and $E = 2.36\alpha' A^{-2.36}$, where α and α' are constants. These are qualitatively consistent

with the high area, low surface concentration region in figure 4.1.
However, while the Π scaling with ϕ is consistent with the model of Aveyard *et al.* [1](measured by Langmuir-Pockels trough), it is not consistent with previous pendant drop measurements on charge-stabilised particles, which have found $\Pi \propto \phi$. Prior to this work, pendant drop experiments had found adsorption models sufficient, while Langmuir-Pockels trough experiments had found interaction models sufficient (see table 5.1). Here, we have found that interactions are necessary to explain the results of our pendant drop experiment.

5.4.2 Frequency Response

Figure 5.5 shows the elastic modulus E' increasing with frequency f, with the most rapid increase for $f < 0.1$ Hz and a more gradual increase above this. This justifies our choice of a standard frequency of 0.1Hz by the small variation in E' with frequency around this point becuase this shows there is little sensitivity to dynamic effects around this frequency. At high frequencies, bulk flow effects can disrupt the measurement [17].
The shape of the $E'(f)$ and $E''(f)$ data is similar to Kobayashi and Kawaguchi's results (figure 4 in [11]), but the loss modulus is significantly lower, with typical values of $E'' < 7$ mN/m compared to their > 14 mN/m. Our elastic modulus is also lower, around 40mN/m at most.
However, measurements were taken at various surface pressures, which makes comparison difficult. In figure 5.6 we plot the dilational modulus normalised by the surface pressure. It is apparent that the fluorescently-labelled ASM530, $r = 193nm$ particles provide a much higher elasticity for a given surface pressure, and that the loss modulus is lower.
The most likely explanation is a non-linear relationship between E' and Π at higher surface pressures since the ASM261, $r = 208$nm particles were probed around $\Pi = 30$mN/m while the ASM530, $r = 193$nm particles were probed around $\Pi = 13$mN/m. It is not clear that the linear region identified in figure 5.3 would extend to higher surface pressures.
An effect due to the fluorescent dye would be surprising, given that it is chemically incorporated into the particle core. Higher charge on labelled particles could explain the higher elasticity and lower loss modulus: electrostatic interactions would increase the E'/Π ratio.
The E'/Π values in figure 5.6 vary less significantly over the measured frequencies than Kobayashi's results. They find a wide range of E'/Π values from around 1.7 to 4.8.

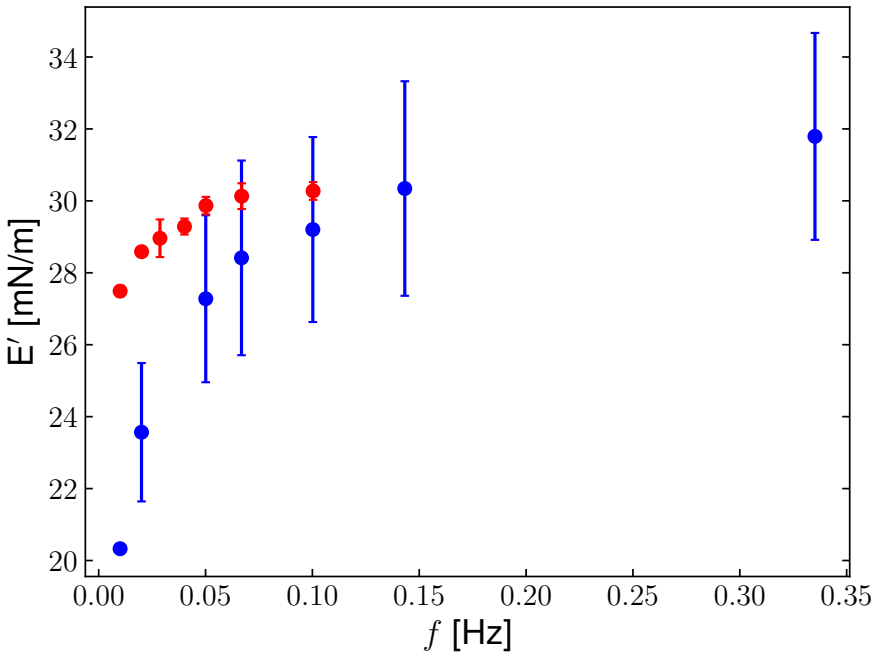

(a)

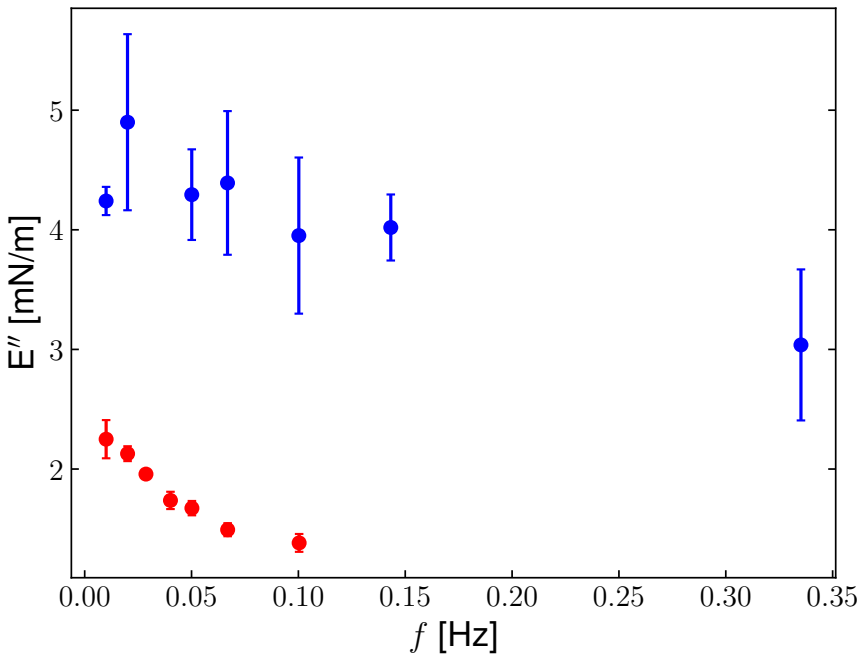

(b)

Figure 5.5 *Frequency response of the dilational storage (E') and loss (E'') moduli for a water drop in n-dodecane with adsorbed $R = 208$ nm PHSA-PMMA particles (blue hues) and $R = 193$ nm fluorescent PHSA-PMMA particles (red).*

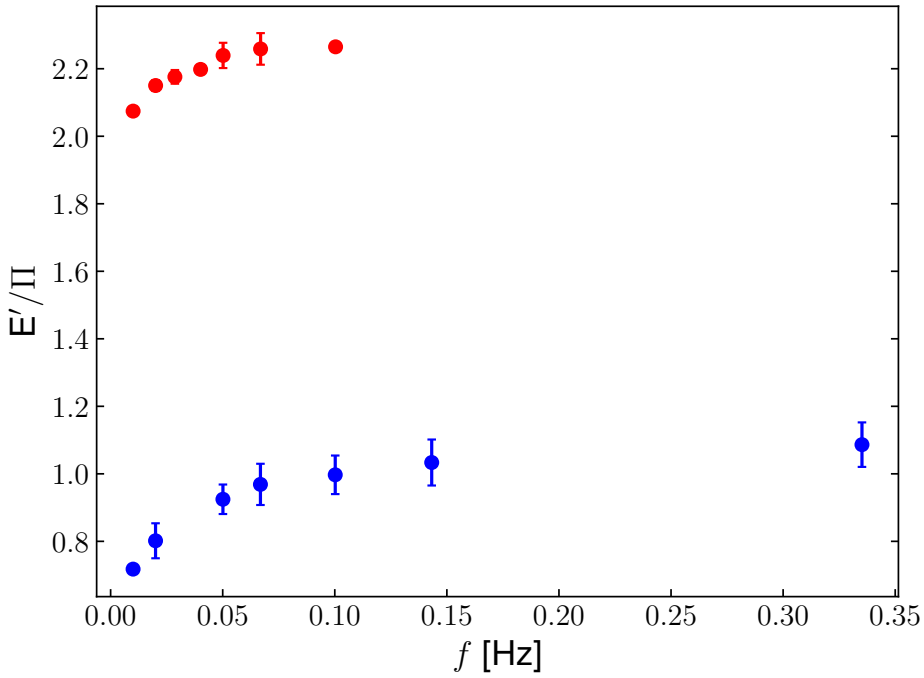

(a)

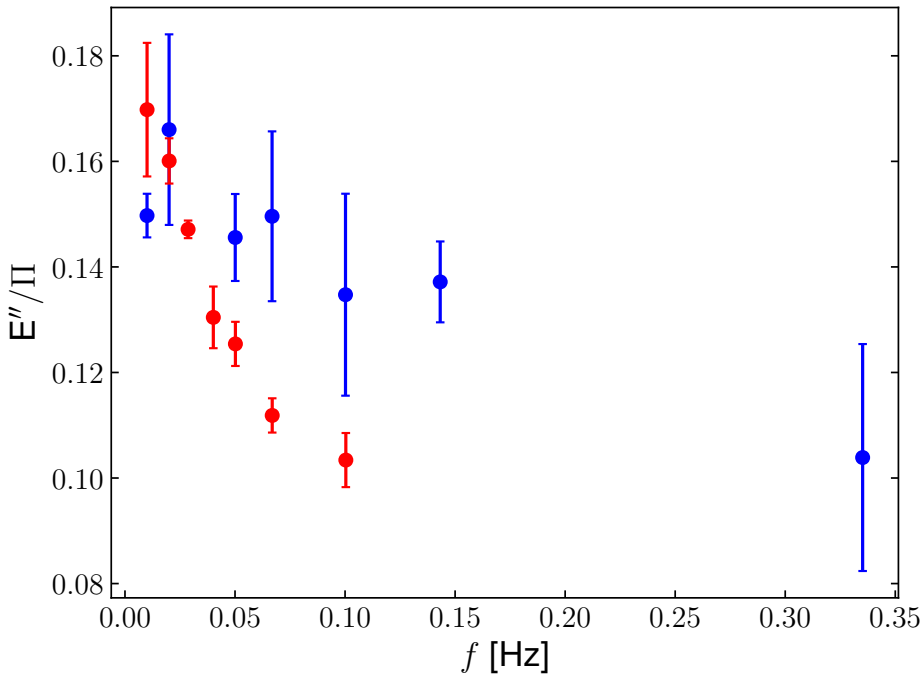

(b)

Figure 5.6 *Frequency response of the dilational storage (E') and loss (E'') moduli normalised by the surface pressure Π for a water drop in n-dodecane with adsorbed $R = 208$ nm PHSA-PMMA particles (blue hues) and $R = 193$ nm fluorescent PHSA-PMMA particles (red).*

5.5 Conclusions

In this chapter we explored the dilational elasticity of small ($R = 193$nm) sterically-stabilised particles adsorbed to a water-dodecane interface. We found that the elasticity and surface pressure gradually increase with particle adsorption. By plotting the elasticity as a function of surface pressure we determined that an adsorption-only model is insufficient to describe our oscillating pendant drop experiments, and that an interaction term is required. This interaction term can be satisfied with dipolar or screened monopole interactions. A screened monopole interaction seems more likely due to the independent findings of Muntz *et al.*, though connecting average interaction potential per particle to interparticle pair potentials is not trivial.

We also probed the frequency response of the dilational elasticity for the small sized particles. We found a modest increase in the elastic modulus with frequency, and a modest decrease in loss modulus with increasing frequency. We also compared two batches of very similar size ($R = 193$nm and $R = 208$nm) and found a significant difference in terms of how much elasticity they produced for a given surface pressure, which we attribute to the non-linearity of the elasticity as a function of surface pressure, though synthesis batch-batch variation is also a possible cause.

Bibliography

[1] Robert Aveyard, John H Clint, Dieter Nees, and Vesselin N Paunov. Compression and structure of monolayers of charged latex particles at air/water and octane/water interfaces. *Langmuir*, 16(4):1969–1979, 2000.

[2] Peter A Kralchevsky, Krassimir D Danov, and Plamen V Petkov. Soft electrostatic repulsion in particle monolayers at liquid interfaces: surface pressure and effect of aggregation. *Phil. Trans. R. Soc. A*, 374(2072):20150130, 2016.

[3] Valeria Garbin, Ian Jenkins, Talid Sinno, John C Crocker, and Kathleen J Stebe. Interactions and stress relaxation in monolayers of soft nanoparticles at fluid-fluid interfaces. *Physical review letters*, 114(10):108301, 2015.

[4] Kan Du, Elizabeth Glogowski, Todd Emrick, Thomas P Russell, and Anthony D Dinsmore. Adsorption energy of nano-and microparticles at liquid- liquid interfaces. *Langmuir*, 26(15):12518–12522, 2010.

[5] Yi Zhang, Songcheng Wang, Jiarun Zhou, Ruiyang Zhao, Gregory Benz, Stephane Tcheimou, J Carson Meredith, and Sven H Behrens. Interfacial activity of nonamphiphilic particles in fluid–fluid interfaces. *Langmuir*, 33(18):4511–4519, 2017.

[6] Xiaoqing Hua, Michael A Bevan, and Joelle Frechette. Reversible partitioning of nanoparticles at an oil–water interface. *Langmuir*, 32(44):11341–11352, 2016.

[7] Xiaoqing Hua, Michael A Bevan, and Joelle Frechette. Competitive adsorption between nanoparticles and surface active ions for the oil–water interface. *Langmuir*, 34(16):4830–4842, 2018.

[8] L Liggieri, E Santini, E Guzmán, A Maestro, and F Ravera. Wide-frequency dilational rheology investigation of mixed silica nanoparticle–ctab interfacial layers. *Soft Matter*, 7(17):7699–7709, 2011.

[9] AG Bykov, BA Noskov, G Loglio, VV Lyadinskaya, and R Miller. Dilational surface elasticity of spread monolayers of polystyrene microparticles. *Soft Matter*, 10(34):6499–6505, 2014.

[10] Nikola A Alexandrov, Krastanka G Marinova, Theodor D Gurkov, Krassimir D Danov, Peter A Kralchevsky, Simeon D Stoyanov, Theodorus BJ Blijdenstein, Luben N Arnaudov, Eddie G Pelan, and Alex Lips. Interfacial layers from the protein hfbii hydrophobin: Dynamic surface tension, dilatational elasticity and relaxation times. *Journal of colloid and interface science*, 376(1):296–306, 2012.

[11] Toshio Kobayashi and Masami Kawaguchi. Surface dilational moduli of latex-particle monolayers spread at air–water interface. *Journal of colloid and interface science*, 390(1):147–150, 2013.

[12] AG Bykov, G Loglio, R Miller, and BA Noskov. Dilational surface elasticity of monolayers of charged polystyrene nano-and microparticles at liquid/fluid interfaces. *Colloids and Surfaces A: Physicochemical and Engineering Aspects*, 485:42–48, 2015.

[13] Wilson CK Poon, Eric R Weeks, and C Patrick Royall. On measuring colloidal volume fractions. *Soft Matter*, 8(1):21–30, 2012.

[14] Valeria Garbin, John C Crocker, and Kathleen J Stebe. Nanoparticles at fluid interfaces: Exploiting capping ligands to control adsorption, stability and dynamics. *Journal of colloid and interface science*, 387(1):1–11, 2012.

[15] Iain Muntz, Franceska Waggett, Michael Hunter, Andrew B Schofield, Paul Bartlett, Davide Marenduzzo, and Job HJ Thijssen. Interaction between nearly hard colloidal spheres at an oil-water interface. *arXiv preprint arXiv:1812.10299*, 2018.

[16] P Kralchevsky and Kuniaki Nagayama. *Particles at fluid interfaces and membranes: attachment of colloid particles and proteins to interfaces and formation of two-dimensional arrays*, volume 10. Elsevier, 2001.

[17] Erik M Freer, Kang Sub Yim, Gerald G Fuller, and Clayton J Radke. Shear and dilatational relaxation mechanisms of globular and flexible proteins at the hexadecane/water interface. *Langmuir*, 20(23):10159–10167, 2004.

Chapter 6

Langmuir-Pockels Trough Measurements of Sub-Micron Particles

6.1 Abstract

In the previous chapter we described a discrepancy in the models used to explain Langmuir-Pockels trough and pendant drop experiments, and reported our own pendant drop measurements. In this chapter we present our Langmuir-Pockels trough experiments on the same system to verify our earlier results. We find good agreement between our pendant drop and trough data when compressing the interface and less good agreement when expanding, so long as trough experiments use sonicated dispersions as the pendant drop experiments do. Examination of the trough results in their own light with accompanying fluorescent imaging shows that compression and expansion cycles compact the interfacial structure and change the interfacial rheology.

6.2 Introduction

In chapter 4 we discussed previous studies on the dilational rheology of colloidal particles at liquid interfaces, which mostly studied charge-stabilised particles in contrast to the sterically-stabilised particles we focus on. Langmuir-Pockels trough measurements showed a characteristic sigmoidal shape in surface pressure as a function of area, illustrated by figure 4.1. The plateau after the sharp rise in surface pressure was attributed to buckling, particle ejection or multilayer

formation that partially relieved the interfacial stress.

In chapter 5 we described an apparent discrepancy between Langmuir-Pockels trough and pendant drop measurements in the literature, where Langmuir-Pockels trough measurements did not require an adsorption energy contribution to their models of the surface pressure while pendant drop measurements did not require an interaction energy term for theirs. We would expect both to have some effect, though we also expected adsorption energies to be dominant from a theoretical estimate. However, for our sterically-stabilised system we found that our pendant drop measurements required an interaction energy to be taken into account.

In this chapter we present Langmuir-Pockels trough measurements on the same system as in chapter 5 to verify our earlier pendant drop measurements. First examining the Langmuir-Pockels trough data, we find that repeated compression and expansion does change the interfacial rheological properties and offer an explanation based on the structural changes we observe. Regarding the comparison of compression and expansion, we find that there is hysteresis, which we attribute to the differences in the interfacial structure between compression and expansion.

Comparing the Langmuir-Pockels trough and oscillating pendant drop data directly on a dilational elasticity vs. surface pressure plot we find good agreement with the compression phase of the trough data, when trough experiments use sonicated dispersions as the pendant drop experiments do.

6.3 Method

This section describes the Langmuir-Pockels trough experiments used to measure elasticity and surface pressure as the interfacial area is varied. For the Langmuir-Pockels trough measurements we used the apparatus and calibration method described in chapter 2.

After filling and calibrating the trough as described in chapter 2, particles would then be added to the interface by pipetting a dispersion of volume fraction $\phi = 0.2\%$ at a number of points near the interface. Here we use the same dispersion as in chapter 5 - ASM530, $R = 193$nm in n-dodecane.

The volume added was originally chosen such that the particles were expected to occupy 130 cm^2 of the available 170 cm^2, corresponding to an expected area fraction of $\phi = 76\%$ below that of ordered close packing. However, for these $R = 193$ nm particles ca. 740 cm^2 of particle area was added, which was necessary to observe an increase in surface pressure. A waiting period of one hour and 15

minutes was allowed. The interface was then compressed and expanded at a barrier speed of 5 mm/min for seven cycles.

After the data was collected, the surface pressure as a function of area was sorted into bins, and the surface pressure of the bare water-dodecane interface was subtracted to isolate the effect of the particles. The dilational elastic modulus was then calculated using the surface pressure and area data and equation (1.11), which was discussed in chapter 1. Finally the modulus, surface pressure and area data were averaged over all samples, with the standard deviation of the points used to estimate the error for each point. This estimated error was much larger than the resolution of the instrument (0.01 mN/m). Each compression and expansion was analysed separately.

Fluorescent imaging used the imaging module described in chapter 2. The objective lens was focused at the interface and the development of the interface over one hour of the waiting period was observed. The lens was re-focused and imaging conditions such as intensity and exposure time were adjusted for good focus and contrast then another observation of around 15 minutes was made to measure the surface density. When compressions were begun, image recording was begun simultaneously to observe the changes under compression for fixed imaging conditions.

Surface coverage estimates were made using the process described in chapter 3. Images for presentation in this chapter were post-processed by background subtraction using the background subtraction routine of ImageJ with a rolling ball radius of 100 pixels (compared to an image size of 640×480 pixels) and the image was sharpened and the contrast enhanced.

6.4 Results and Discussion

6.4.1 Effects of Compression Cycles

We begin by examining the effect of cyclic compression and expansion on the surface pressure Π and structure of the particle-laden interfaces. As introduced in chapter 3, we plot Π as a function of the apparent surface fraction ϕ_{app} from imaging (white-fraction method), normalised by the value of ϕ_{app} when the surface pressure begins to rise for the first compression cycle.

Figure 6.1 shows the surface pressure and elastic modulus data for three compressions while 6.2 shows the same for expansion. Other cycles have been omitted for clarity since they essentially align with the seventh and final cycle.

In figure 6.1 we can see that the surface pressure Π of the last cycle increases at a higher surface fraction, and reaches a higher value at maximum compression. This is in contrast to the first compression, where Π begins increasing sooner, but reaches a plateau around 5 mN/m.

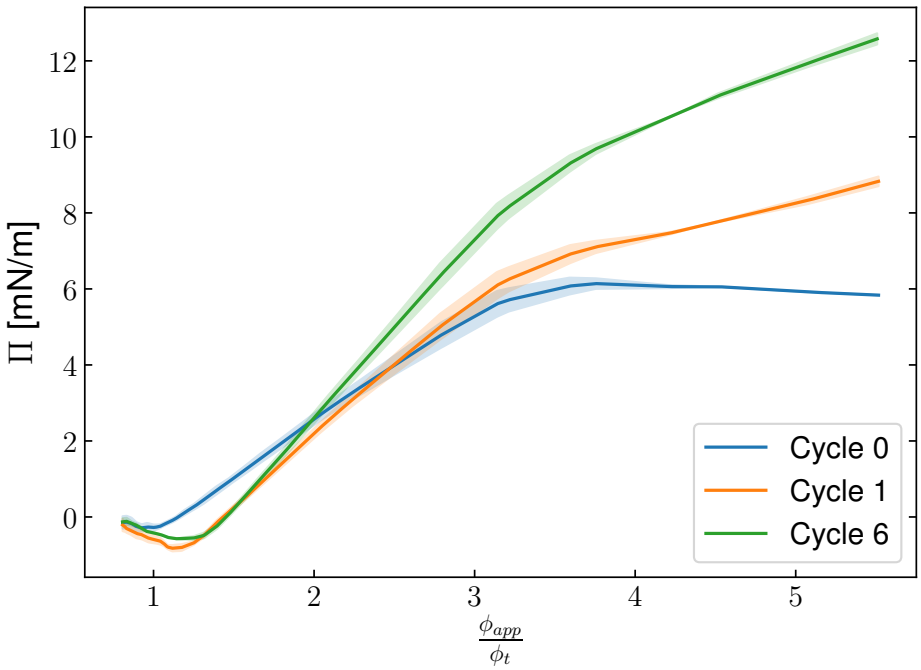

Figure 6.1 *Surface pressure* Π *as a function of normalised surface fraction* ϕ_{app}/ϕ_t *(see text for definition) for the first, second and seventh compressions (blue, orange and green respectively) on the Langmuir-Pockels trough. Error bars are estimated from the distribution of samples in each bin.*

The most recognisable feature is the sigmoidal shape of the surface pressure as a function of area shown by the first cycle in figure 6.3. This shape aligns with previous studies discussed in chapter 4 and illustrated by figure 4.1. However the 5 mN/m surface pressure here is much lower than the bare interfacial tension of the interface where collapse by buckling is expected to occur [1]. Particle expulsion or multilayer formation have also been reported as collapse modes, and they do not require such high surface pressures [2, 3].

But since we did not observe these collapse modes, we offer another hypothesis: under high enough surface pressures, the particles are pushed into close enough contact that they reach their Van der Waals minimum and aggregate at the interface. By lowering the repulsion between particles, this relieves surface pressure and gradually changes the surface structure into islands of close packed

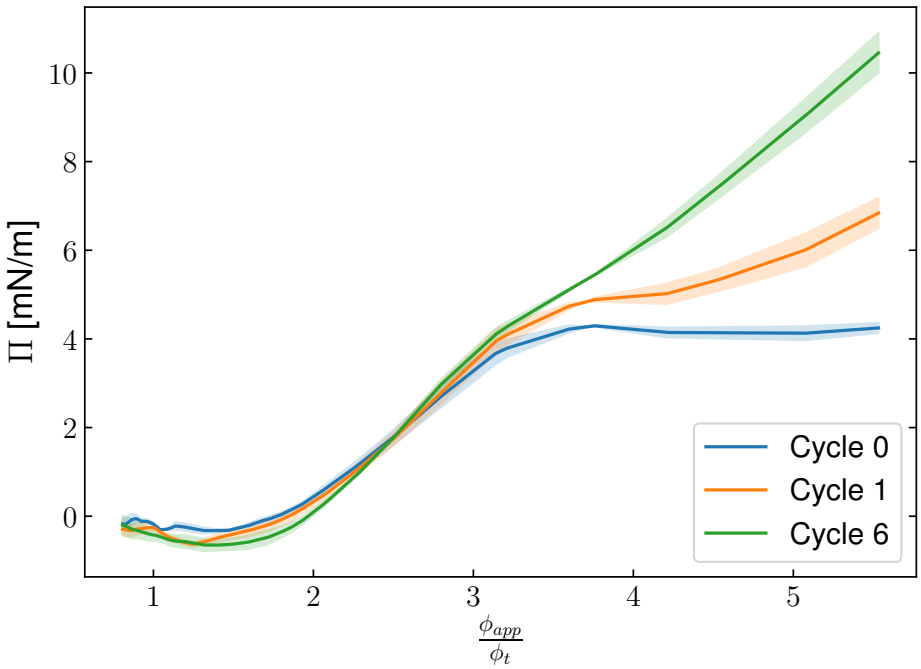

Figure 6.2 *Surface pressure* Π *as a function of normalised surface fraction* ϕ_{app}/ϕ_t *(see text for definition) for the first, second and seventh expansions (blue, orange and green respectively) on the Langmuir-Pockels trough. Error bars are estimated from the distribution of samples in each bin.*

particles. This compaction can be seen in the fluorescent micrographs shown in figure 6.4, which show the interface before and after compression and expansion. The more open, percolating structure seen in figures 6.4a and 6.4b becomes a coexistence of the more compact aggregates of figure 6.4c and low density regions between them, as shown in figure 6.4d. This hypothesis seems contradictory to the findings of Kralchevsky *et al.* who found that aggregation increased the surface pressure rather than reduced it [4]. However their model did not include Van der Waals attractions and their experiments involved charge-stabilised rather than sterically-stabilised particles, which may affect the relative significance of Van der Waals forces to their system.

Our observations align to some degree with those reported by Beltramo *et al.* [5] for sterically-stabilised polystyrene-polyvinylpyrrolidone (PS-PVP) particles at the water-air interface, who also attributed the cycle-to-cycle changes to morphological changes. However, they found that their plateau in surface pressure was due to buckling rather than the aggregation mechanism we outline above.

Rheological changes under compaction may have a bearing on the use of sterically-

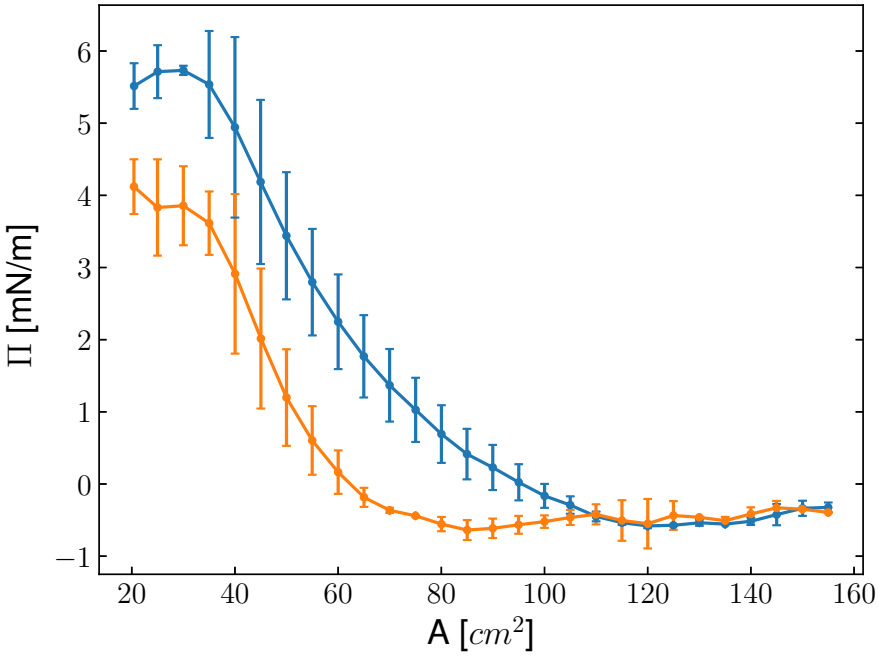

Figure 6.3 *Surface pressure* Π *as a function of area A for the first cycle of compression (blue) and expansion (orange) on the Langmuir-Pockels trough. Error bars are estimated from the distribution of samples in each bin.*

stabilised particles for Pickering emulsions: deformation that causes compaction could allow higher surface pressures and elasticity at high surface fraction, but leave large regions of low density at lower surface fractions. The resulting effect on emulsion stability would not be straightforward.

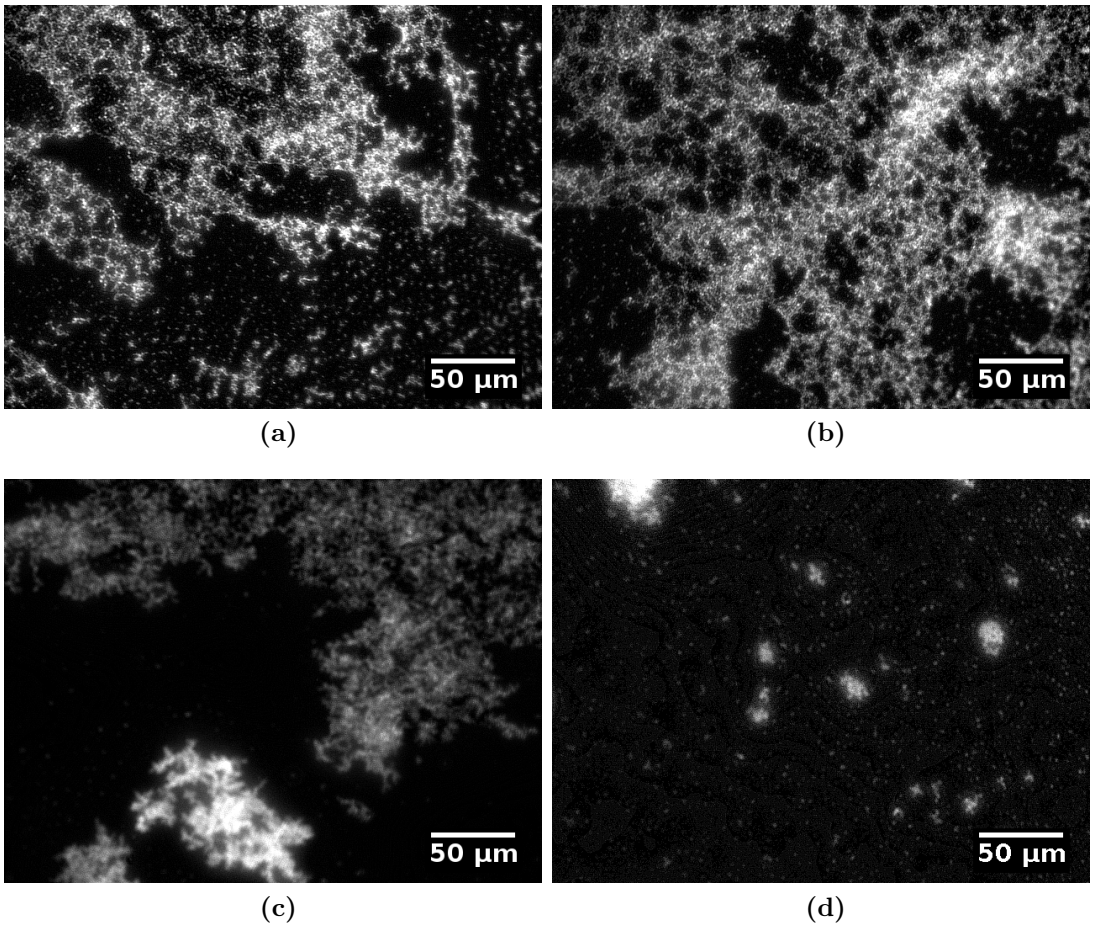

Figure 6.4 *Fluorescent micrographs showing the structure of the interface before compression (a,b) and after compression and expansion (c,d). All images are taken at an interfacial area close to the starting area.*

6.4.2 Comparison to Pendant Drop Results

We now compare the above results to the oscillating pendant drop experiments we presented in chapter 5. The Langmuir-Pockels trough data for the seventh (and final) compression and expansion cycle and pendant drop data from chapter 5 are shown in figure 6.5. It can be seen that while the elastic moduli in the region around Π= 5 mN/m agree, the qualitative shape of the plots differ. The Langmuir-Pockels trough data show a more rapid increase in elasticity at low Π, before slowing at higher surface pressures. This is in contrast to the steady increase in elasticity observed on the oscillating pendant drop. However as we learned in chapter 4, sonication of the particle dispersion immediately before addition to the interface changes the stress response. Figure 6.6 compares the seventh compression and expansion cycle for the sonicated case to the oscillating pendant drop data. The agreement is good -unsurprising given that the particle

dispersion used for pendant drop experiments was also sonicated before use.

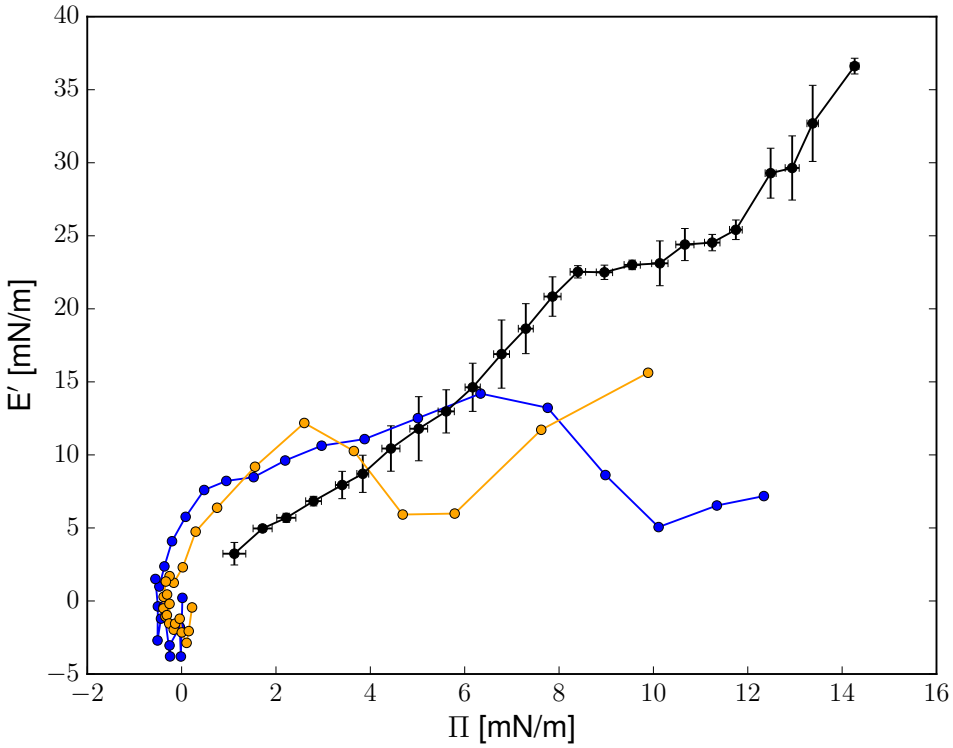

Figure 6.5 *Dilational elasticity E' as a function of surface pressure Π for oscillating pendant drop measurements (black) and compression (blue) and expansion (orange) measurements on a Langmuir-Pockels trough (seventh compression-expansion cycle). Error bars are estimated from the distribution of samples in each bin. The particle dispersion was not sonicated before addition to the trough.*

While the agreement between techniques is good for compression and expansion in the trough experiments at low Π, above $\Pi = 4$ mN/m the expansion data presents a notably higher elastic modulus. We explain this by considering the interfacial structure: during compression, the structure is more connected and particles sustain a steadily increasing surface pressure as the surface fraction increases. During expansion, large voids are created and the surface pressure drops rapidly. Since the dilational elastic modulus measures the rate of change of surface pressure with surface concentration, a larger modulus is presented during expansion.

There are some reasons to be wary of the comparison between techniques. First, with a maximum area strain of 88% the strains involved in Langmuir-Pockels trough measurements are much larger than the 4% used for pendant drop experiments. The strain in the trough experiment has surpassed 4% before the

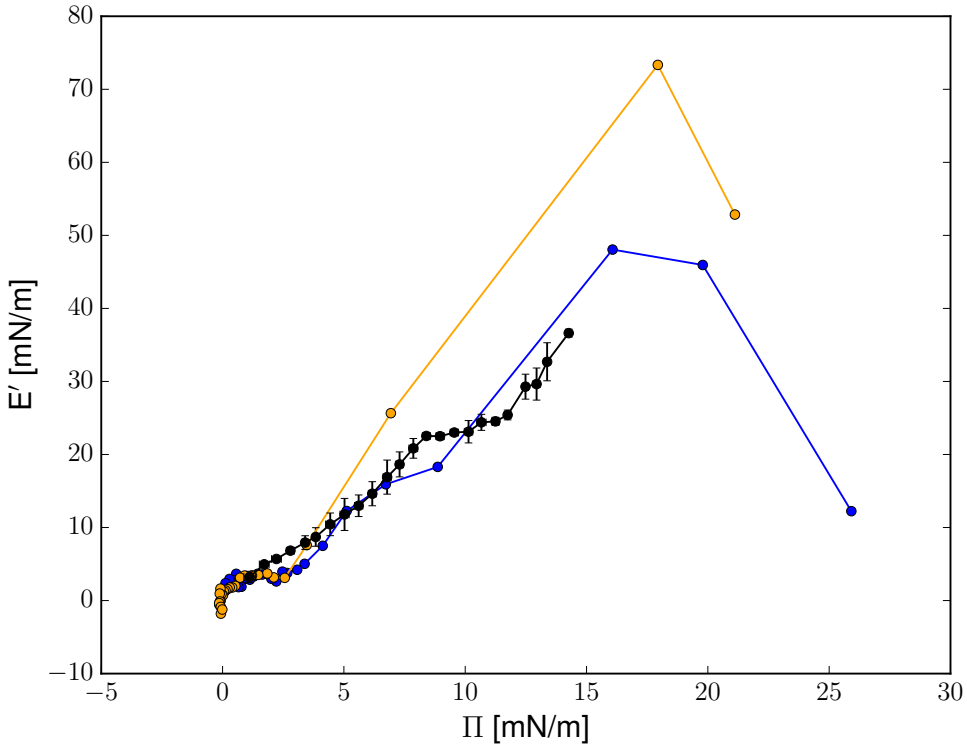

Figure 6.6 *Dilational elasticity E' as a function of surface pressure* Π *for oscillating pendant drop measurements (black) and compression (blue) and expansion (orange) measurements on a Langmuir-Pockels trough (seventh compression-expansion cycle). The particle dispersion was sonicated before addition to the trough.*

surface pressure has begun to rise. Verwijlen *et al.* [6] and more recently Pepicelli *et al.* [7] have discussed how large strains can require more careful constitutive modelling than the simple linear model discussed in chapter 1.

Second, as we discussed in chapters 1 and 2 the Langmuir-Pockels trough does not apply a purely dilational strain to the interface so shear components of the interfacial stress can affect the measurement [7], especially for smaller particles [1]. As we have kept the Wilhelmy plate fixed perpendicular to the barriers in our experiments, we cannot estimate these shear components. But based on the good agreement in figure 6.6 and the reportedly weak shear response of comparable particles [8] it seems reasonable to neglect their effect.

Finally, gravity has a component parallel to the interface in drop experiments but does not in trough experiments. The Bond number (see chapter 1) for an individual particle in the drop experiments is $\mathrm{Bo} = \mathcal{O}(10^{-8})$. This is insignificant, but one might wonder whether these particles have a significant collective weight acting on one particle such as in the keystone effect described by Tavacoli *et*

al.[9]. If Bo $= 10^{-8}$, there must be more than 10^8 particles for there to be a significant collective effect. The maximum number of particles on the pendant drop interface at close packing, based on the particle size and drop surface area is 10^8. Therefore, this is a potentially significant effect, but only at high surface concentrations.

We can also analyse the effect of gravity on the particle monolayer following the approach of Law *et al.* [10]. We only have the surface pressure density scaling from our measurements, so to estimate the value of the surface pressure as a function of density we use the expression of Muntz *et al.* [11] with their parameters of $a_1 = 4136$ and inverse screening length $\kappa = 0.35$ μm^{-1} for a screened monopole potential between particles separated by r is

$$U_m = \frac{a_1 k_B T}{3r} e^{-\kappa r}. \tag{6.1}$$

Assuming a hexagonal lattice for simplicity so that $\phi = (2\pi/\sqrt{3})R^2/r^2$, and only including nearest neighbour interactions, the interaction energy per particle of radius R and cross-sectional area $a_p = \pi R^2$, and using our canonical ensemble approach, we can obtain the surface pressure using equation 1.40 as

$$\Pi = \frac{3a_1 k_B T}{2a_p} \phi \left(\kappa + \frac{1}{r}\right) e^{-\kappa r}. \tag{6.2}$$

From the force balance on a thin horizontal strip of the vertical monolayer, we follow Law *et al.* [10] and get

$$\mathrm{d}\Pi = -\rho m^* g \mathrm{d}z \tag{6.3}$$

with

$$m^* = (\rho_p - \rho_w)V_{pw} + (\rho_p - \rho_o)V_{po} \tag{6.4}$$

and

$$V_{pw} = \pi R^3 (1 + \cos(\theta))^2 (2 - \cos(\theta))/3, \quad V_{po} = 4\pi R^3/3 - V_{pw}. \tag{6.5}$$

It follows that

$$\int_{\rho_0}^{\rho} \frac{1}{\rho} \frac{\mathrm{d}\Pi}{\mathrm{d}\rho} \mathrm{d}\rho = -\int_0^z m^* g \mathrm{d}z. \tag{6.6}$$

Differentiating Π with respect to rho gives us

$$\frac{\mathrm{d}\Pi}{\mathrm{d}\rho} = \frac{a_1 k_B T}{4a_p} \left(\frac{3}{r} + r\kappa^2 - \kappa\right) e^{-\kappa r}. \tag{6.7}$$

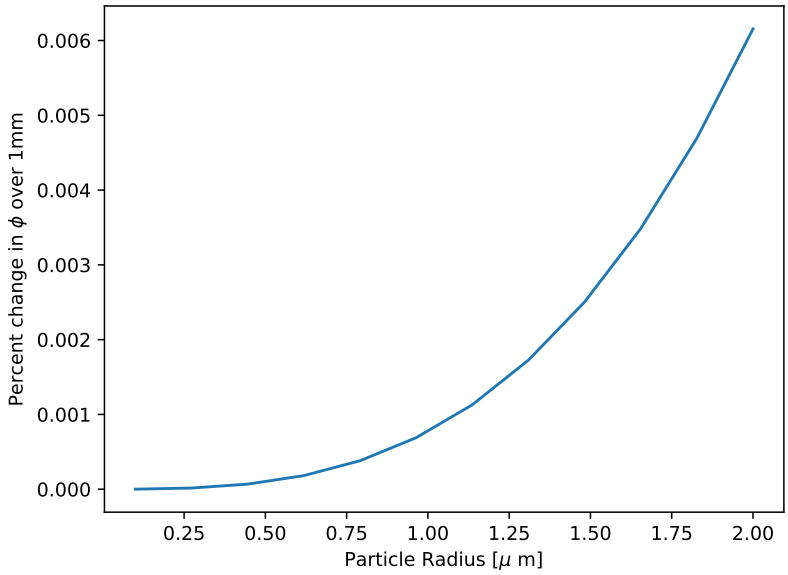

Figure 6.7 *Predicted percentage change in surface fraction ϕ over 1mm in height for a range of particle sizes.*

Integrating in terms of r rather than ρ leads us to

$$-m^* gz = \frac{a_1 k_B T}{2}\left(\left[\frac{3}{r_0}e^{-\kappa r_0} - \frac{3}{r}e^{-\kappa r}\right] + \kappa\left[e^{-\kappa r} - e^{-\kappa r_0}\right] - \int_{r_0}^{r}\frac{2\kappa}{r}e^{-\kappa r}\mathrm{d}r\right). \tag{6.8}$$

The final term in 6.8 is the exponential integral i.e. it does not integrate to an elementary function, but we can numerically solve this to obtain ϕ for a given phi_0. Finally, we can use this to calculate $(\phi - \phi_0)/\phi_0$, which informs us of how much the surface density varies over the given height z. Figure 6.7 shows the percentage change in surface fraction over 1 mm in height for various particle sizes. From this we would predict that surface sedimentation is negligible even for large particles. Experimentally, we have seen evidence to the contrary; we have seen drops form a clearly darker lower half which suggests surface sedimentation. We should therefore be cautious of this prediction, and it remains somewhat unclear whether gravity has a significant effect on the surface pressure for smaller particles.

Despite these differences between the systems, the agreement between the sonicated particles is good overall and verifies our data.

6.5 Conclusions

In this chapter we examined Langmuir-Pockels trough data previously discussed in chapter 4, here focussing on the changes over cycles of compression and expansion. Compression-expansion cycles were shown to affect interfacial properties by increasing the elastic modulus of the interface at high surface fractions through the compaction of the original open structure. Comparing the trough data with our pendant drop measurements from chapter 5, we found good agreement with the compression phase of the trough data if the particle dispersions were sonicated before use.

Bibliography

[1] Robert Aveyard, John H Clint, Dieter Nees, and Nick Quirke. Structure and collapse of particle monolayers under lateral pressure at the octane/aqueous surfactant solution interface. *Langmuir*, 16(23):8820–8828, 2000.

[2] Valeria Garbin, John C Crocker, and Kathleen J Stebe. Forced desorption of nanoparticles from an oil–water interface. *Langmuir*, 28(3):1663–1667, 2011.

[3] Theo D Kassuga and Jonathan P Rothstein. Buckling of particle-laden interfaces. *Journal of colloid and interface science*, 448:287–296, 2015.

[4] Peter A Kralchevsky, Krassimir D Danov, and Plamen V Petkov. Soft electrostatic repulsion in particle monolayers at liquid interfaces: surface pressure and effect of aggregation. *Philosophical Transactions of the Royal Society A: Mathematical, Physical and Engineering Sciences*, 374(2072):20150130, 2016.

[5] Peter J Beltramo, Manish Gupta, Alexandra Alicke, Irma Liascukiene, Deniz Z Gunes, Charles N Baroud, and Jan Vermant. Arresting dissolution by interfacial rheology design. *Proceedings of the National Academy of Sciences*, 114(39):10373–10378, 2017.

[6] T Verwijlen, L Imperiali, and J Vermant. Separating viscoelastic and compressibility contributions in pressure-area isotherm measurements. *Advances in colloid and interface science*, 206:428–436, 2014.

[7] Martina Pepicelli, Tom Verwijlen, Theo A Tervoort, and Jan Vermant.

Characterization and modelling of langmuir interfaces with finite elasticity. *Soft matter*, 13(35):5977–5990, 2017.

[8] Rob Van Hooghten, Victoria E Blair, Anja Vananroye, Andrew B Schofield, Jan Vermant, and Job HJ Thijssen. Interfacial rheology of sterically stabilized colloids at liquid interfaces and its effect on the stability of pickering emulsions. *Langmuir*, 33(17):4107–4118, 2017.

[9] Joe W Tavacoli, Gijs Katgert, E Grace Kim, Michael E Cates, and Paul S Clegg. Size limit for particle-stabilized emulsion droplets under gravity. *Physical review letters*, 108(26):268306, 2012.

[10] Adam D Law, D Martin A Buzza, and Tommy S Horozov. Two-dimensional colloidal alloys. *Physical review letters*, 106(12):128302, 2011.

[11] Iain Muntz, Franceska Waggett, Michael Hunter, Andrew B Schofield, Paul Bartlett, Davide Marenduzzo, and Job HJ Thijssen. Interaction between nearly hard colloidal spheres at an oil-water interface. *arXiv preprint arXiv:1812.10299*, 2018.

Chapter 7

Collective Particle Detachment from Liquid Interfaces

7.1 Abstract

Particle-laden interfaces have been known to buckle, expel particles, or form multilayers under compression. This chapter reports a novel phenomenon where large structures detach from particle-laden interfaces under compression. We show that particles of various sizes around and below 1 μm produce this phenomenon from both flat and curved interfaces. The structures are always ejected into the oil phase, suggesting a preferred curvature for the particle-laden interface which is consistent with the hydrophobicity of our particles. The process and structures produced are imaged by confocal microscopy, which suggest that the ejection of the structures proceeds from a buckled state, confirming a prediction from an earlier study on elastic films.

7.2 Introduction

Pickering emulsions have seen renewed interest recently and this interest has led naturally to investigation of the interfacial properties of particle laden interfaces [1–5]. It is well-known that colloids are energetically driven to adsorb to liquid interfaces with a contact angle θ, and that the reduction in free energy (ΔG) associated with the adsorption of a particle of radius R at an interface with interfacial tension γ is $\Delta G = \pi R^2 \gamma (1 - |\cos\theta|)^2$. For typical colloids this leads to an adsorption energy of several orders of magnitude greater than $k_B T$, and particles are usually considered irreversibly adsorbed [6, 7].

When particle-laden liquid interfaces are compressed, two collapse mechanisms have been observed on both flat and curved interfaces: buckling or wrinkling comparable to an elastic film [8–15], and particle expulsion from the interface [16–18]. It seems that the contact angle has a strong effect on which is observed [19–22]. Recently, Kassuga *et al.* [23] have observed trilayer formation in micron scale latex particle films as in earlier work by Leahy *et al.* [24] on gold nanoparticle films. These were thought to be due to folds forming after the initial buckling, which then contact the monolayer to form a trilayer.

The buckling of elastic films on liquid-fluid interfaces has attracted interest as a model problem related to elastic film buckling on elastic substrates [25]. The results developed have provided insight into the buckling of particle films, such as explaining the buckling wavelength's dependence on particle size [23]. For thin elastic films on fluid interfaces, there are also two modes of collapse: wrinkling [26, 27] and delamination [28]. Wrinkling begins with Eulerian buckling, with a wavelength determined by the balance between elastic energy, which favours a long wavelength, and gravitational energy, which favours a short wavelength. This leads to an expected wavelength of $\lambda = 2\pi(B/(\Delta\rho g))^{\frac{1}{4}}$ if the bending modulus is B and the superphase-subphase density difference is $\Delta\rho$. Wrinkle wavelength has been shown to decay from the centre to the border [29].

If compression is continued, the film may continue to wrinkle. The film weight breaks the degeneracy of symmetric and antisymmetric wrinkling, so that symmetric wrinkling is favoured if the film is denser than the subphase. Eventually the film will undergo a wrinkle-to-fold transition where most wrinkles shrink at the expense of a few which grow into larger folds [30]. Films denser than the subphase select downwards folds exclusively.

Otherwise, under further compression, delamination may occur instead of further wrinkling or folding. In this case it is energetically favourable for the fluid interface to spontaneously detach from the elastic film to form a 'blister' [28]. These mechanisms are illustrated in figure 7.1.

We aim to present a novel collapse mode for particle-laden liquid interfaces and offer some experimental insight into the mechanism. We discuss two possibilities (illustrated in figure 7.1) based on elastic film literature: ejection of a fold as predicted by Jambon-Puillet et al. in their 2016 work [30] or rapid delamination akin to that described by Wagner and Vella [28].

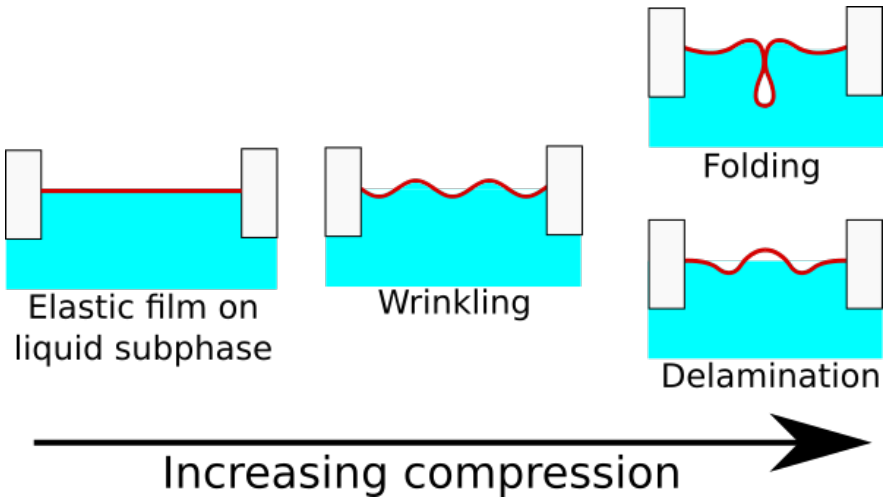

Figure 7.1 *Schematic of collapse modes for elastic films on a liquid.*

7.3 Materials and Methods

The particle radii R used were 208nm (ASM261), 264nm (ASM317), 474nm (ASM457) and 1120nm (ASM449), characterised by dynamic light scattering. Only the $R = 1120$nm particles were fluorescently labelled as described in chapter 2. Particle contact angles have been estimated by various techniques and reported values range from around $\theta = 130°$ (freeze-fracture) to around $\theta = 160°$ (gel-trapping, macroscopic contact angle) [6, 31, 32] while our own measurements by a recently developed spectroscopic technique [33] gave $\theta = 164.8 \pm 1.7°$ as discussed in chapter 2.

Water drops of various volumes were expanded into particles dispersed in oil on the drop tensiometer described in chapter 2, the particles were allowed to adsorb, then the drop surface was compressed or expanded by pumping water out of or into the drop. To generate oil in water drops, particle dispersion was taken up into a J shaped needle, then expanded into water before compression-expansion cycles. Water dyed with sodium fluorescein was used in some experiments to better visualise the water phase and interfacial wrinkling.

Two troughs were used to observe the compression of the particle laden interfaces. First, a standard Langmuir-Pockels PTFE trough and an imaging module (described in chapter 2) was used to take surface pressure (Π) measurements while observing surface concentration and structure. Second, a small aluminium trough made in-house (area 20×17 mm) and aluminium barrier was used to allow confocal imaging of the water/oil interface.

The standard trough was partially filled with water before oil was carefully added, defining an interfacial area we could subject to compression. Surface pressure

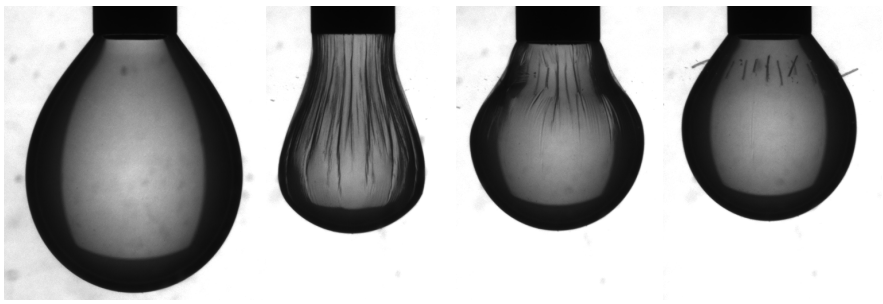

Figure 7.2 *Delamination from a water drop in oil proceeding from wrinkling for $r = 474nm$ particles during a compression-expansion cycle.*

measurements on the bare water-air and water-oil interfaces provided means of calibration, as described in chapter 2. Particles dispersed in oil were then added to the superphase near the interface and allowed to adsorb for an hour. A filter paper Wilhelmy plate, pre-soaked in water for 20 minutes to dissolve contaminants, was used to measure the surface pressure. Compression and expansion was performed at 5mm/min for a number of cycles.

For measurements using the smaller trough we partially filled the trough with water, then added particles dispersed in the oil. Particles were allowed to adsorb to the interface for an hour, then the barrier was moved by hand to compress the interface. The surface pressure was not measured. For confocal imaging we used a Leica SP8 confocal microscope, and a Leica HC PL FLUOTAR 10× objective with a numerical aperture of 0.30. The excitation laser had a wavelength of 488 nm and a prism was used to filter out this excitation light leaving only the emission light.

7.4 Results and Discussion

We begin by characterising the collective particle detachment. First, their occurrence is almost always preceded by wrinkling (a corrugation of the interface) and folding (where the interface comes into self-contact). Although wrinkling has been observed on the trough with $r = 1126$nm particles prior to delamination, it is not as clear as it is for droplets, that folding occurs. Figure 7.2 shows how delamination occurs during a compression-expansion cycle on a $R = 474$nm particle-covered water drop in oil.

Second, they seem to have a characteristic width of the order of 100μm: figure 7.3 shows projections of confocal micrographs of structures (using $R = 1126$nm particles) sat on the interface and others which have been extracted from the standard trough by pipette before being imaged on the confocal microscope.

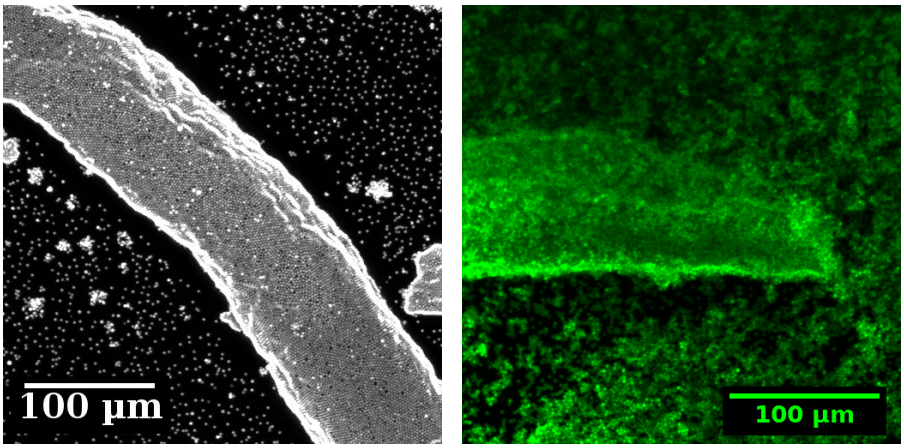

(a) (b)

Figure 7.3 *Confocal microscope images of fluorescent $R = 1126nm$ particle delaminates collected from the standard trough (left) and observed directly on the small trough (right). Images are generated from a z-projection of a z-stack.*

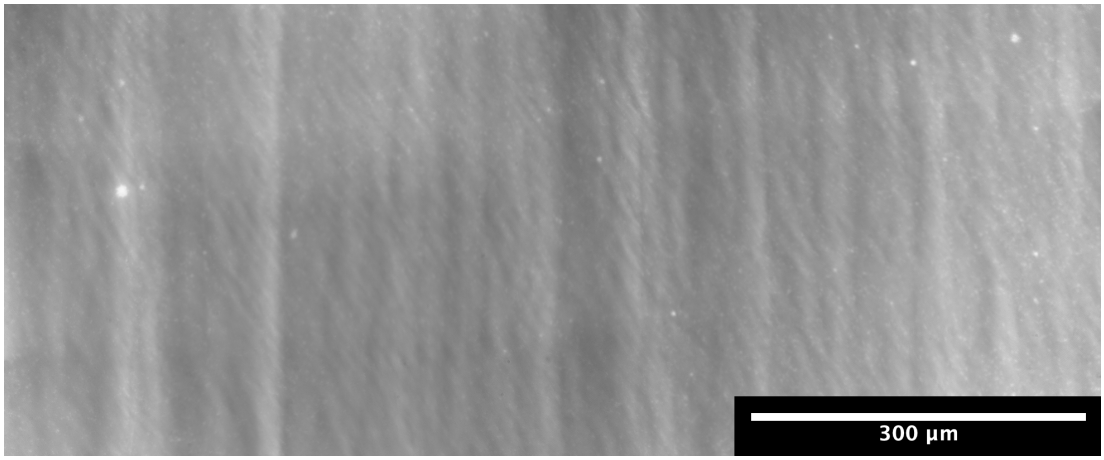

Figure 7.4 *Composite image of a buckled particle layer on the standard trough.*

This size is consistent with the buckling wavelength Aveyard *et al.* found for compressed polystyrene monolayers at an octane-water interface. Our own buckling shows a range of separations which are of comparable size to the detached structures, as can be seen in figure 7.4. Along with the observation that wrinkling precedes detachment, this suggests that the detached structures are connected to the buckling of the interface.

The detachment of folds in a particle-laden interface has been predicted previously in a study on elastic film behaviour at liquid interfaces by [30]: the self-contact of the interface allows the folds to 'pinch-off' as shown in figure 7.5. This is probably aided - we suggest - by the clearance of particles from the neck of the fold by drainage as described by Stancik *et al.* [34]. The folding mechanism predicts that

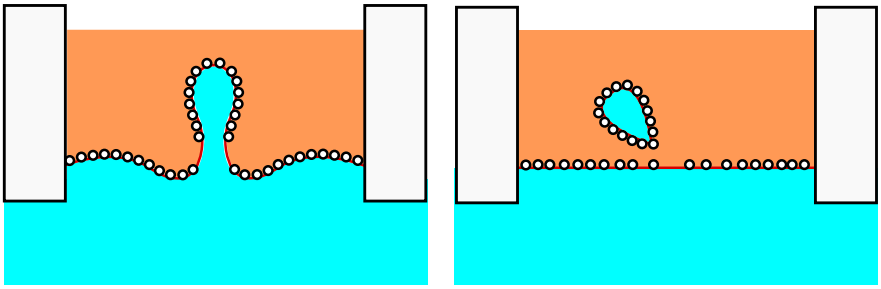

Figure 7.5 *Schematic of suggested folding mechanism for collective particle detachment.*

the ejected structures will include some water for our system.

It is not yet clear whether structures contain water, like an extended Pickering emulsion drop, or if they are simply particle aggregates. To investigate this, we used sodium fluorescein dyed water and non-dyed particles. Folds in the interface formed channels as they made self-contact, and sometimes these channels visibly trapped water. However, the dye changed the interfacial properties of the interface, making wrinkling highly reversible and preventing the detachment of the folds, so we could not confirm that the detached structures contain water; we can say only that the folds sometimes do.

Confocal microscopy scans of detached structures from systems without dyed water (figure 7.3) suggest that the detached structures are tubular and have a single particle layer on the outside - like a high aspect ratio Pickering drop - rather than being aggregates. This suggests that the 'delamination' mechanism shown in figure 7.1 and discussed in [28] is unlikely to be the case here because it is unclear how it could generate the tubular structures we observe.

The predicted folding mechanism also predicts that downwards folds - i.e. projecting into the water phase - will be favoured [30] because of the film weight. In contrast, we observe that delamination always occurs into the oil phase. Figure 7.6 shows delamination into the oil phase for two different particle sizes for both water-in-oil and oil-in-water interfaces. Also, by varying the focus height of the imaging which accompanies the trough measurements, we can see that the detached structures sit on top of the interface, in the oil phase.

We explain this by noting the small weight of the particle monolayer, and we propose that the particle contact angle leads to different bending moduli for different directions. For hydrophobic particles at an interface, if the interface bends such that the radius of curvature lies in the water phase, the adsorbed particles will be moved apart. If bent in the other direction, the particles will be forced further into contact, and the interface will exert a higher resistance.

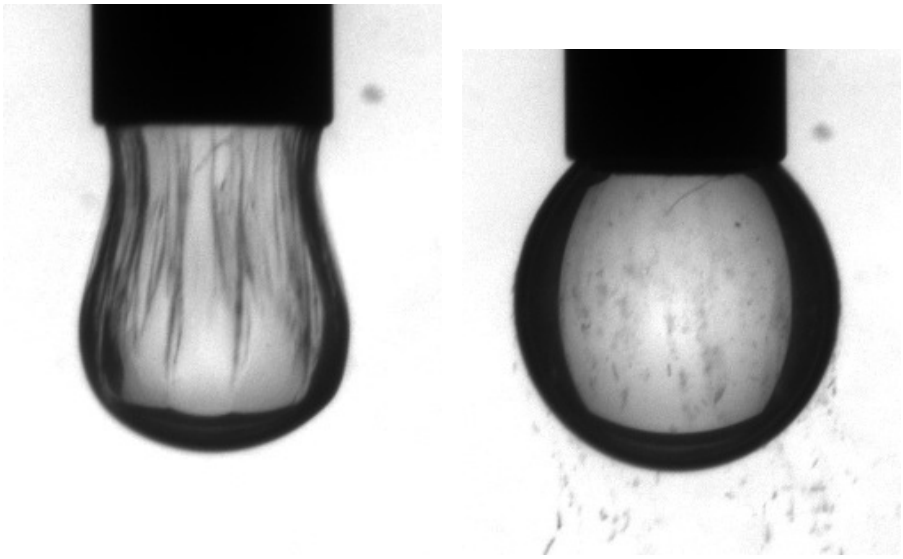

(a) **(b)**

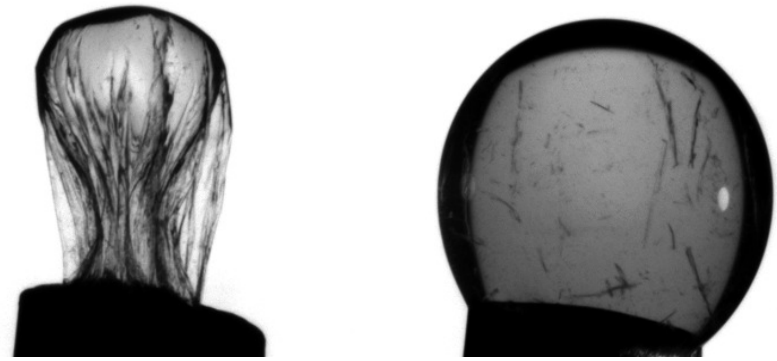

(c) **(d)**

Figure 7.6 *Delamination of $R = 264nm$ particles from a water drop in oil (top row) and of fluorescent $R = 199nm$ particles from an oil drop in water (bottom row). The observed structures quickly sediment. The small bright spot on the oil drop is illumination from the imaging module for higher magnification fluorescent imaging.*

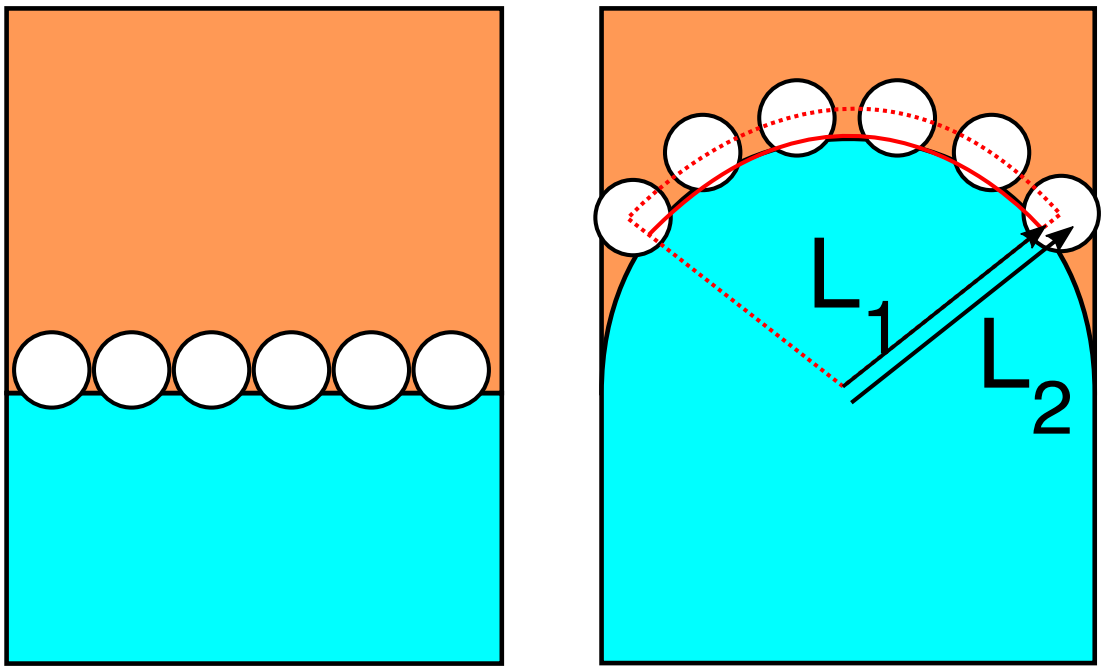

Figure 7.7 *Schematic of a particle-laden interface deformed by bending, for hydrophobic particles at the interface of water (blue) and oil (orange). L_1 is the radius of curvature of the interface, and L_2 is the radius of curvature of the particle centres.*

Figure 7.7 illustrates this: if the radius of curvature of the interface lying in the water phase is L_1, then $L_2 = L_1 + R$ and the particles have more space each. We suggest that this generates a preferred curvature which outweighs the effect of weight and leads to upwards folds, which in turn leads to ejection into the oil. This argument also predicts that hydrophilic particles will delaminate into the water phase.

Finally, we note that the detachment of large numbers of particles from the interface rapidly lowers the total surface fraction of particles there. We observe this on the trough: particle motion is arrested as the interface is compressed, then the interface suddenly becomes mobile and detached structures are observed above the interface.

An interesting observation of these structures is that on water drops, they have been observed to remain attached at one end for $R = 474$nm and $R = 264$nm particles, as shown in figure 7.8. For $R = 474$nm particles, the structures move to the base of the drop over time due to gravity - recall from chapter 2 that the particles are denser than water - which has a component acting parallel to the drop interface until the delaminates reach the drop apex. In the case of oil drops in water the structures simply fall into the needle instead. That the delaminates remain stuck to the drop shown in figure 7.8 is not so surprising when we consider

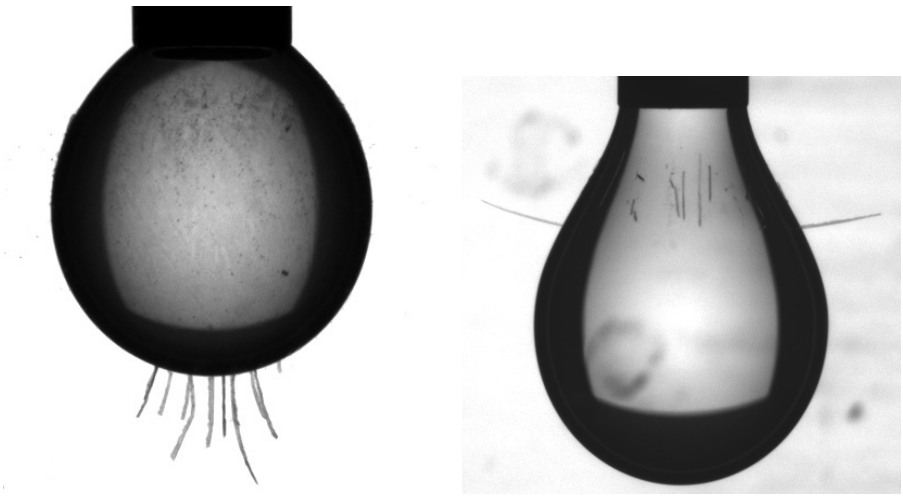

(a) **(b)**

Figure 7.8 *Delaminates from $R = 474nm$ (left) and $R = 264nm$ (right) particles stuck to the drop (water in oil) that formed them. The $R = 474nm$ delaminates have gradually moved to the base of the drop, some time after they are produced.*

the balance of energies. For a $R = 0.5\mu$m particle with a contact angle of $\theta = 160°$ at a water-dodecane interface, one particle attached to the interface can support the weight of roughly $2{\times}10^6$ particles.
In summary, we have described how collective particle detachment proceeds from wrinkling and folding of the interface, the re-mobilising effect it has on the remaining particles at the interface, and how the ejected structures can remain partly attached to the interface.

7.5 Conclusions

We have observed the detachment of large structures of sterically-stabilised particles from an oil-water interface for several particle sizes around and below 1 μm on flat and droplet interfaces, as predicted by Jambon-Puillet et al.[30]. This phenomenon can be explained by the 'pinch-off' of self-contacting folds which develop as the interface is compressed. The structures are consistently ejected into the oil phase, which we attribute to a preferential bending modulus induced by their hydrophobicity.

Bibliography

[1] J Thijssen and Jan Vermant. Interfacial rheology of model particles at liquid interfaces and its relation to (bicontinuous) pickering emulsions. *J. Phys. Condens. Matter*, 30:023002, 2018.

[2] Bernard P Binks and Tommy S Horozov. *Colloidal particles at liquid interfaces*. Cambridge University Press, 2006.

[3] Gerald G Fuller and Jan Vermant. Complex fluid-fluid interfaces: rheology and structure. *Annual review of chemical and biomolecular engineering*, 3:519–543, 2012.

[4] Omkar S Deshmukh, Dirk van den Ende, Martien Cohen Stuart, Frieder Mugele, and Michel HG Duits. Hard and soft colloids at fluid interfaces: Adsorption, interactions, assembly & rheology. *Advances in colloid and interface science*, 222:215–227, 2015.

[5] Bernard P Binks. Particles as surfactants - similarities and differences. *Current opinion in colloid & interface science*, 7(1-2):21–41, 2002.

[6] Rob Van Hooghten, Victoria E Blair, Anja Vananroye, Andrew B Schofield, Jan Vermant, and Job HJ Thijssen. Interfacial rheology of sterically stabilized colloids at liquid interfaces and its effect on the stability of pickering emulsions. *Langmuir*, 33(17):4107–4118, 2017.

[7] Pawel Pieranski. Two-dimensional interfacial colloidal crystals. *Physical Review Letters*, 45(7):569, 1980.

[8] Robert Aveyard, John H Clint, Dieter Nees, and Nick Quirke. Structure and collapse of particle monolayers under lateral pressure at the octane/aqueous surfactant solution interface. *Langmuir*, 16(23):8820–8828, 2000.

[9] Cécile Monteux, John Kirkwood, Hui Xu, Eric Jung, and Gerald G Fuller. Determining the mechanical response of particle-laden fluid interfaces using surface pressure isotherms and bulk pressure measurements of droplets. *Physical Chemistry Chemical Physics*, 9(48):6344–6350, 2007.

[10] Dominic Vella, Pascale Aussillous, and L Mahadevan. Elasticity of an interfacial particle raft. *EPL (Europhysics Letters)*, 68(2):212, 2004.

[11] Hui Xu, Sonia Melle, Konstantin Golemanov, and Gerald Fuller. Shape and buckling transitions in solid-stabilized drops. *Langmuir*, 21(22):10016–10020, 2005.

[12] Nicolas Tsapis, Eric R Dufresne, Shrabani S Sinha, Christophe S Riera, John W Hutchinson, Lakshminarayana Mahadevan, and David A Weitz. Onset of buckling in drying droplets of colloidal suspensions. *Physical review letters*, 94(1):018302, 2005.

[13] Tommy S Horozov, Robert Aveyard, Bernard P Binks, and John H Clint. Structure and stability of silica particle monolayers at horizontal and vertical octane- water interfaces. *Langmuir*, 21(16):7405–7412, 2005.

[14] M Safouane, D Langevin, and BP Binks. Effect of particle hydrophobicity on the properties of silica particle layers at the air- water interface. *Langmuir*, 23(23):11546–11553, 2007.

[15] Nicolas Taccoen, François Lequeux, Deniz Z Gunes, and Charles N Baroud. Probing the mechanical strength of an armored bubble and its implication to particle-stabilized foams. *Physical Review X*, 6(1):011010, 2016.

[16] Gy Tolnai, A Agod, M Kabai-Faix, AL Kovacs, JJ Ramsden, and Z Hórvölgyi. Evidence for secondary minimum flocculation of stöber silica nanoparticles at the air- water interface: Film balance investigations and computer simulations. *The Journal of Physical Chemistry B*, 107(40):11109–11116, 2003.

[17] Valeria Garbin, John C Crocker, and Kathleen J Stebe. Forced desorption of nanoparticles from an oil–water interface. *Langmuir*, 28(3):1663–1667, 2011.

[18] Vincent Poulichet and Valeria Garbin. Ultrafast desorption of colloidal particles from fluid interfaces. *Proceedings of the National Academy of Sciences*, 112(19):5932–5937, 2015.

[19] Samuel O Asekomhe, Raymond Chiang, Jacob H Masliyah, and Janet AW Elliott. Some observations on the contraction behavior of a water-in-oil drop with attached solids. *Industrial & engineering chemistry research*, 44(5):1241–1249, 2005.

[20] Sándor Bordács, Attila Agod, and Zoltán Hórvölgyi. Compression of langmuir films composed of fine particles: collapse mechanism and wettability. *Langmuir*, 22(16):6944–6950, 2006.

[21] Francesca Ravera, Michele Ferrari, Libero Liggieri, Giuseppe Loglio, Eva Santini, and Alessandra Zanobini. Liquid–liquid interfacial properties of mixed nanoparticle–surfactant systems. *Colloids and Surfaces A: Physicochemical and Engineering Aspects*, 323(1):99–108, 2008.

[22] Sepideh Razavi, Kathleen D Cao, Binhua Lin, Ka Yee C Lee, Raymond S Tu, and Ilona Kretzschmar. Collapse of particle-laden interfaces under compression: buckling vs particle expulsion. *Langmuir*, 31(28):7764–7775, 2015.

[23] Theo D Kassuga and Jonathan P Rothstein. Buckling of particle-laden interfaces. *Journal of colloid and interface science*, 448:287–296, 2015.

[24] Brian D Leahy, Luka Pocivavsek, Mati Meron, Kin Lok Lam, Desiree Salas, P James Viccaro, Ka Yee C Lee, and Binhua Lin. Geometric stability and elastic response of a supported nanoparticle film. *Physical review letters*, 105(5):058301, 2010.

[25] Fabian Brau, Pascal Damman, Haim Diamant, and Thomas A Witten. Wrinkle to fold transition: influence of the substrate response. *Soft Matter*, 9(34):8177–8186, 2013.

[26] Luka Pocivavsek, Robert Dellsy, Andrew Kern, Sebastián Johnson, Binhua Lin, Ka Yee C Lee, and Enrique Cerda. Stress and fold localization in thin elastic membranes. *Science*, 320(5878):912–916, 2008.

[27] Haim Diamant and Thomas A Witten. Compression induced folding of a sheet: An integrable system. *Physical review letters*, 107(16):164302, 2011.

[28] Till JW Wagner and Dominic Vella. Floating carpets and the delamination of elastic sheets. *Physical review letters*, 107(4):044301, 2011.

[29] Jiangshui Huang, Benny Davidovitch, Christian D Santangelo, Thomas P Russell, and Narayanan Menon. Smooth cascade of wrinkles at the edge of a floating elastic film. *Physical review letters*, 105(3):038302, 2010.

[30] Etienne Jambon-Puillet, Dominic Vella, and Suzie Protière. The compression of a heavy floating elastic film. *Soft matter*, 12(46):9289–9296, 2016.

[31] Lucio Isa, Falk Lucas, Roger Wepf, and Erik Reimhult. Measuring single-nanoparticle wetting properties by freeze-fracture shadow-casting cryo-scanning electron microscopy. *Nature communications*, 2:438, 2011.

[32] Job HJ Thijssen, Andrew B Schofield, and Paul S Clegg. How do (fluorescent) surfactants affect particle-stabilized emulsions? *Soft Matter*, 7(18):7965–7968, 2011.

[33] Imre T Horváth, Pierre Colinet, and Maria Rosaria Vetrano. Measuring contact angles of small spherical particles at planar fluid interfaces by light extinction. *Applied Physics Letters*, 108(20):201605, 2016.

[34] Edward J Stancik, Mehrnaz Kouhkan, and Gerald G Fuller. Coalescence of particle-laden fluid interfaces. *Langmuir*, 20(1):90–94, 2004.

Chapter 8

Proteins at Liquid Interfaces and Comparison to Interfacial Colloids

8.1 Abstract

In this chapter we bring together the insights we gained in previous chapters to attempt to understand proteins at interfaces using a colloid model. We will first compare the physics behind the interfacial rheology of proteins and particles and point out areas of similarity and difference. Moving on to our experiments, we will highlight how size appears to be a minor factor for the interfacial rheology for both. Using the cage protein ferritin as a model particle-like protein, we show how the understanding of particles at interfaces developed in earlier chapters allows us to interpret the interfacial rheology of proteins. Finally, we will discuss how both particles and proteins present a novel collapse mode.

8.2 Introduction

We began this thesis with an explanation of why it is important to understand the interfacial rheology of proteins and how particles may help us to do that. In this chapter we briefly remind the reader of the characteristics of protein and particle interfacial rheology we discussed in chapter 1 before we present our experiments on ferritin - a relatively large (approx. 12 nm), approximately spherical cage protein with a mineral core [1]. Having discussed our results, we will then be in a position to draw together the connections between particle and protein interfacial behaviour before we come to our conclusions in chapter 9.

Proteins are ubiquitous surface active agents in food and nature, and their

interfacial rheology matters for a number of reasons [2]. Commonly cited is its relevance to dispersion stability, but it is also important to biological functions such as lung alveoli, digestion, and biofilms [3–5]. To better understand this interfacial behaviour, we set out to use colloidal particles as a model system.

The properties of particles at interfaces depend very much on the properties of the particles themselves: tuning interaction forces can create a range of structures from two-dimensional gels to crystals, with a correspondingly wide range of mechanical responses [6]. However, what they have in common is a high desorption energy for the adsorbed particles. This causes surface pressure and the dilational elasticity to increase as surface concentration increases until the interface yields through buckling or particle expulsion at a critical surface concentration. As we saw in chapter 7, further compression beyond buckling can even lead to the formation of elongated structures.

Proteins also show a wide range of structures and reponses. For example, while many proteins can be understood as a 2-D gel, BslA is known to form well-ordered rafts at the interface, and under high compression can form tubule-like structures not dissimilar to particles [7, 8]. Ultimately proteins are folded polymers (as are our polymer colloids, though they are in a poor solvent condition) and models of their interfacial behaviour may need to treat them as such, especially for proteins which unfold at the interface such as β-casein [9].

For globular proteins such as bovine serum albumin and β-lactoglobulin we expect the comparison to be beneficial, but it is also useful for proteins which do unfold as the comparison should allow us to differentiate between particle-like behaviour and unfolding-related behaviour. We noted earlier in chapter 1 that some authors have already performed such a comparison. For example, Cicuta *et al.* showed that both colloidal particles and β-lactoglobulin produced a master curve for the shear modulus as a function of frequency, which held for various surface concentrations [10]. More recently, Tcholakova *et al.* compared particles, globular proteins, and surfactants as emulsifiers and found that globular proteins can indeed behave similarly to particles as an emulsifier depending on experimental conditions such as pH [11], and that mass-balance equations used to predict mean drop size can be applied to both particles and proteins. This comparison may also inform our understanding of colloid behaviour - Fainerman *et al.* used a model developed for proteins (and discussed in chapter 1) to understand surface pressure isotherms for micro and nano sized particles [12].

Unsurprisingly given the difficulty of imagining how one would vary only the size of a protein and nothing else, the effect of protein size specifically has only been

the subject of one study to our knowledge - though even there it is unclear whether important factors such as rigidity were controlled. Murphy *et al.* compared the dilational rheology of β-lactoglobulin aggregates of different sizes from 200-300 nm in diameter. While they found that smaller aggregates increased the dilational elasticity (with negligible loss modulus) more quickly, the differences between them were otherwise small in terms of surface pressure and elasticity as a function of strain.

In studying particle interfacial behaviour we hoped to build a bridge from that understanding to the domain of proteins. But proteins are generally complex, so we aim to enter that domain via a model particle-like protein. For this purpose we explored ferritin. Ferritins are a family of large, cage-like, approximately spherical globular protein weighing 450kDa, with an external diameter of about 12nm and internal diameter of about 8nm, and often have a mineral core [13]. Bacteria, plants, animals, aerobic and anaerobic organisms all use them for protein cofactor synthesis and iron storage [1, 14, 15]. So far they have found use as nanomaterial templates - e.g. nanoparticles which can target cancer cells [16] - but future uses may involve more specific features such as the ion channels which exist in the ferritin cage walls [1]. For such applications it is important to understand their interfacial properties - e.g. for the production of Langmuir-Blodgett films - in addition to our intended use as a model particle-like protein.

The interfacial properties of ferritin were recently reviewed by Jutz *et al.* [15]. Ferritin forms a dense crystalline monolayer at the (buffered) water-decane interface. Its surface pressure isotherm was determined by plotting the equilibrium surface tensions for various bulk concentrations. It shows a sharp rise at a certain bulk concentration before reaching a 'knee' as concentration continues to increase, which was associated with compression of the proteins' occupied area. This curve agreed well with the compressible areas theory described in chapter 1 which treats interfacial interactions rather simply.

We therefore try to use our theory described in chapter 1 and applied to particles in chapter 5 to better understand the inter-protein interactions. In the following experiments we focus on the water-dodecane interface and conduct a very similar procedure to chapter 5 for ease of comparison. We will show that ferritin has short-ranged interactions which scale in energy ϵ_i with the surface concentration ϕ as approximately $\epsilon_i \propto \phi^3$, in qualitative agreement with previous reports.

8.3 Method

To study the interfacial rheology of ferritin (Sigma, Ferritin from equine spleen, Type I saline solution, Lot SLBQ9541V) we used a n-dodecane drop in buffered water. The buffer used a combination of 25 mM concentration solutions of monobasic sodium phosphate and dibasic sodium phosphate mixed approximately in a 2:3 monobasic:dibasic ratio, and adjusted until a calibrated pH meter (Mettler-Toledo) read a pH of 7.00. Given the manufacturer's stated concentration on the certificate of analysis as 55 mg/mL we prepared solutions to various concentrations from 0.005 mg/mL to 1 mg/mL. Dynamic light scattering measurements (which were described in chapter 2) were performed on a 0.01 mg/mL sample to estimate the protein size. We found a hydrodynamic diameter of 10-14 nm, consistent with previous reports of the structure as being 12nm in diameter [17].

We prepared a 45 μL drop of n-dodecane in buffer to calibrate or in buffered ferritin solution for measurements, and applied the oscillating pendant drop method described in chapter 2 and used previously to study particles in chapter 5. We applied an area strain of approximately 2 % at a frequency of 0.05 Hz. These values for the strain and frequency were chosen after sweeping these variables to determine regions where the elastic complex modulus did not vary with either. To measure the dilational elastic modulus we restricted ourselves to a concentration of 0.005 mg/mL so that the surface pressure would vary little during any individual measurement of the elastic modulus. The raw data on surface pressure and surface area of the drop as a function of time were analysed as described in chapter 2 to calculate the complex dilational modulus. Three non-oscillating drops were produced for each concentration, from which we calculated a mean and error estimate. Four oscillating drops were tested at one concentration of 0.005 mg/mL. Surface pressures for the oscillating drop are reported as averages over the observation window used to calculate the dilational modulus.

8.4 Ferritin Interfacial Rheology Results and Discussion

After drop formation ($t = 0$) ferritin begins adsorbing to the drop interface, as evidenced by the increasing surface pressure and elastic modulus shown in figure 8.1. We can see faster rates of surface pressure increase with increasing concentration, though the increase from the 0.005 mg/mL oscillating drop to the

0.01 mg/mL non-oscillating drop is small. While the surface pressure continues to rise for the oscillating drop, the elastic modulus E' reaches a plateau after an hour. The loss modulus remains very low throughout, suggesting that ferritin could resist bubble shrinkage or Ostwald ripening in dispersions [18]. We observed a similarly negligible loss modulus for PHSA-PMMA particles in chapter 5, though here the surface pressures and elastic modulus values are higher - 20 mN/m vs. 14 mN/m for Π and 60 mN/m vs. 30 mN/m for E'.

These data can be compared with experiments on the water/decane interface by Jutz *et al.* shown in figure 40 of [19]. They found an equilibrium surface pressure of 14 mN/m for 0.005 mg/mL, which is significantly lower than what we observe after a much shorter time. This difference could be explained by the influence of oscillations on the adsorption. Oscillations may both increase advective flow to the interface and disrupt the interfacial structure, allowing further adsorption.

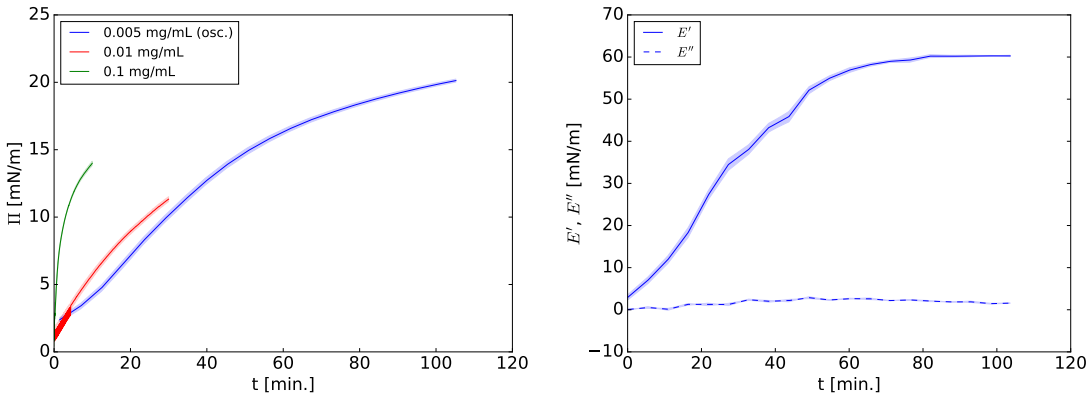

(a) **(b)**

Figure 8.1 *(a) Surface pressure* Π *for various bulk concentrations and (b) dilational elastic modulus* E' *and loss modulus* E'' *for a bulk concentration of 0.005 mg/mL ferritin as a function of time t after water drop creation in n-dodecane.*

Plotting the elastic modulus E' as a function of surface pressure Π in figure 8.2 we see another parallel with earlier experiments: the relationship is linear for $\Pi < 15$ mN/m. In a study on β-lactoglobulin, Cicuta and Terentjev suggested that oscillations might be responsible for the surprisingly large linear region of the observed $E(\Pi)$ plot by allowing the exploration of otherwise inaccessible conformations [20]. This leads us to attempt to apply the theory we introduced in chapter 1 and applied in chapter 5.

In that theory the gradient of $E(\Pi)$ represents $(1 + \lambda)$ where λ describes the scaling of average (per protein) interaction energy ϵ_i with surface fraction ϕ as $\epsilon_i(\phi) \propto \phi^{\lambda}$. Assuming that this can be straightforwardly related to the pair

potential energy $\xi(\phi)$ allows us to say $\epsilon_i(\phi) \propto \xi(\phi)$. Then, taking the structure to be hexagonal [19] provides the relationship between surface fraction and mean interparticle separation r as $\phi \propto r^{-2}$. Thus $\xi(r) \propto r^{-2\lambda}$.

For our measurements, the observed gradient is 3.99 ± 0.02, so $(1+\lambda) = 3.99 \pm 0.02$, this means $\xi(r) \propto r^{-5.98 \pm 0.04}$. In their 2012 review, Garbin *et al.* gave a number of approximate forms for various types of interaction ranging from capillary forces to electrostatic interaction [21]. None of those forms match the observed scaling so it is not immediately clear whether this is a useful interpretation. Capillary interactions due to roughness or an anisotropic shape have $\xi(r) \propto r^{-4}$, while as we discussed in chapter 5 charged particles at an interface have a long-ranged term of $\xi(r) \propto r^{-3}$. The Van der Waals interaction between atoms has a well-known dependence of r^{-6}, however large scale bodies have a different dependence on separation [22] and it is not clear that ferritin is small enough for the r^{-6} dependence to be a reasonable expectation. The linear $E(\Pi)$ behaviour has also been observed for asphaltanes[1] by Rane *et al.*, for β-lactoglobulin by Cicuta and Terentjev, and results by Lucassen-Reynders *et al.* suggest that it occurs for other proteins also at low surface pressures [9, 20, 23]. However, each set of authors use a different model for this behaviour. Rane *et al.* use a Langmuir equation, Cicuta and Terentjev use scaling laws developed for polymers along with a Flory model for the overlap concentration, while Lucassen-Reynders *et al.* use the compressible areas model discussed in chapter 1. A key difference between our model and the compressible areas model is that we only consider the interaction potential's effect on the surface pressure i.e. the enthalpic contribution, while the compressible areas model mainly deals with the entropic contribution and approximates the interactions as proportional to the square of the surface concentration - see chapter 1. The interaction we observed could simply be due to steric repulsion i.e. an entropy driven repulsion and this would be fundamentally consistent at least with the models discussed above, though the expected scaling for steric interaction is unclear.

There are already moves towards a unification of our understanding of particle and protein interfacial rheology, such as the use of the compressible areas model - developed for proteins - to fit the surface pressure behaviour of micro and nanoparticles [12]. Here, we offer a colloid based understanding of how interactions affect the gradient of a linear $E(\Pi)$ relationship: higher gradients indicate shorter ranged forces. In the case of ferritin, this implies that the interaction forces between proteins are short-ranged, though we must qualify

[1] key surface active polyaromatic compounds in oil recovery

this by pointing out that this approach only considers the enthalpic contribution to surface pressure, which may not be applicable to small proteins. This result of short-ranged interactions is consistent with the small range of accessible areas (defined by $\omega_{min} = 2.0 \times 10^7\ m^2/\text{mol}$ and $\omega_{max} = 2.5 \times 10^7\ m^2/\text{mol}$) ferritin was found to occupy when the compressible areas model was used to fit its behaviour - table 12 of [19].

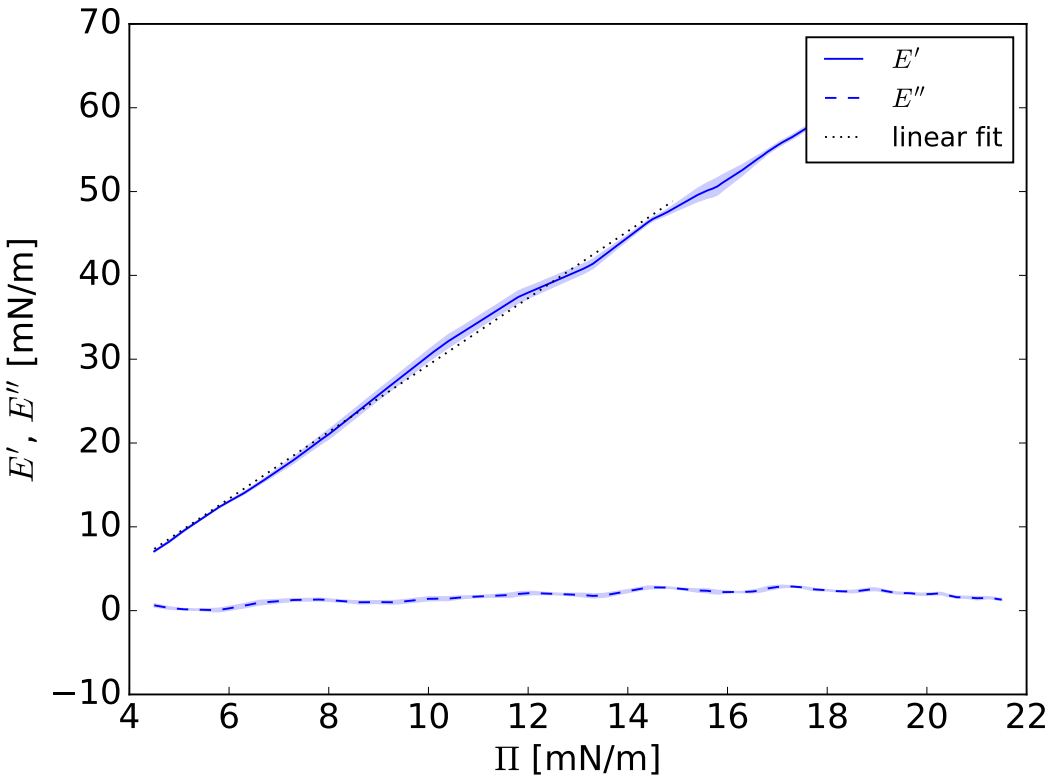

Figure 8.2 *Dilational elastic modulus E' and loss modulus E'' of ferritin at a bulk concentration of 0.005 mg/mL adsorbing to a water/n-dodecane interface, as a function of surface pressure Π, and a linear fit up to $\Pi = 15$ mN/m with gradient 3.98±0.02.*

Having discussed one connection between particles and proteins, we now turn to the remaining two we will discuss: the relative unimportance of size (over a certain range), and the phenomenon of collective particle detachment discussed in chapter 7.

As we discussed in the introduction to this chapter, it is difficult to investigate the effect of size independently of other factors. Perhaps the closest attempt was by Murphy *et al.* on β-lactoglobulin aggregates, whose size can be controlled by pH and heat [24]. This study found only small differences in their interfacial rheology between the different sizes of aggregates. Using sterically-stabilised particles we

have found little difference down to 400 nm diameter, but this was seemingly dependant on aggregation - see chapter 4. This is consistent with other work on charge-stabilised colloids, which found that size does not matter over this range. However for such sizes adsorption energies are still large, so desorption is usually considered irreversible. In comparison protein sizes are typically much smaller than this - usually less than $\mathcal{O}(10)$ nm - with correspondingly smaller adsorption energies, so future studies hoping to connect particles and proteins should focus on the range of particle sizes which have adsorption energies approaching thermally accessible levels i.e. nanoparticles or particles with extreme contact angles.
One aspect in which our large colloids may prove to be a successful model is for proteins which strongly adsorb to the interface not because of their size, but because of other reasons such as in the case of BslA, where a conformational change at the interface increases the desorption energy [25]. In chapter 7 we saw that folds in the particle-laden interface lead to the detachment of tubular structures. A very similar phenomenon was observed by Morris *et al.* [8], who also found that long tubular structures detached from the interface upon compression. Future studies may develop this analogy to understand the specific properties required for collective particle detachment.

8.5 Conclusions

In this chapter we examined the interfacial rheology of ferritin as a candidate for a model particle-like protein and found that it exhibited similar characteristics to particle behaviour observed in earlier chapters: negligble dilational loss modulus, and a linear region of elasticity as a function of surface pressure. We applied our particle-based model, described in chapter 1, to understand this behaviour and found that ferritin inter-protein forces are short-ranged, consistent with a report by Jutz [19]. Regarding the effect of particle size, we discussed how this seems to be an unimportant factor for particles and proteins which are several hundred nanometers in diameter perhaps due to the large desorption energies. These large desorption energies may be useful to understand larger or unusually strongly adsorbing proteins such as BslA, which show a similar phenomenon to the collective particle detachment we described in chapter 7. However, future studies should concentrate on low desorption energy particles as model systems.

Bibliography

[1] Elizabeth C Theil. Ferritin protein nanocages - the story. *Nanotechnology perceptions*, 8(1):7, 2012.

[2] Brent S Murray. Rheological properties of protein films. *Current Opinion in Colloid & Interface Science*, 16(1):27–35, 2011.

[3] Minoru Ueno. Colloidal and interfacial properties of lung surfactants. *Membrane*, 27:233–43, 2002.

[4] Pedro Reis, Krister Holmberg, Reinhard Miller, Jurgen Kragel, Dmitri O Grigoriev, Martin E Leser, and Heribert J Watzke. Competition between lipases and monoglycerides at interfaces. *Langmuir*, 24(14):7400–7407, 2008.

[5] Keith M Bromley, Ryan J Morris, Laura Hobley, Giovanni Brandani, Rachel MC Gillespie, Matthew McCluskey, Ulrich Zachariae, Davide Marenduzzo, Nicola R Stanley-Wall, and Cait E MacPhee. Interfacial self-assembly of a bacterial hydrophobin. *Proceedings of the National Academy of Sciences*, 112(17):5419–5424, 2015.

[6] Bernard P Binks and Tommy S Horozov. *Colloidal particles at liquid interfaces*. Cambridge University Press, 2006.

[7] Brent S Murray. Interfacial rheology of food emulsifiers and proteins. *Current opinion in colloid & interface science*, 7(5-6):426–431, 2002.

[8] Ryan J Morris, Keith M Bromley, Nicola Stanley-Wall, and Cait E MacPhee. A phenomenological description of bsla assemblies across multiple length scales. *Philosophical Transactions of the Royal Society A: Mathematical, Physical and Engineering Sciences*, 374(2072):20150131, 2016.

[9] EH Lucassen-Reynders, J Benjamins, and VB Fainerman. Dilational rheology of protein films adsorbed at fluid interfaces. *Current Opinion in Colloid & Interface Science*, 15(4):264–270, 2010.

[10] Pietro Cicuta, Edward J Stancik, and Gerald G Fuller. Shearing or compressing a soft glass in 2d: time-concentration superposition. *Physical review letters*, 90(23):236101, 2003.

[11] S Tcholakova, ND Denkov, and A Lips. Comparison of solid particles, globular proteins and surfactants as emulsifiers. *Physical Chemistry Chemical Physics*, 10(12):1608–1627, 2008.

[12] VB Fainerman, VI Kovalchuk, EH Lucassen-Reynders, DO Grigoriev, JK Ferri, ME Leser, M Michel, R Miller, and H Möhwald. Surface-pressure isotherms of monolayers formed by microsize and nanosize particles. *Langmuir*, 22(4):1701–1705, 2006.

[13] PM Harrison, SC Andrews, PJ Artymiuk, GC Ford, JR Guest, J Hirzmann, DM Lawson, JC Livingstone, JMA Smith, A Treffry, et al. Probing structure-function relations in ferritin and bacterioferritin. *Advances in inorganic chemistry*, 36:449–486, 1991.

[14] Elizabeth C Theil. Ferritin: the protein nanocage and iron biomineral in health and in disease. *Inorganic chemistry*, 52(21):12223–12233, 2013.

[15] Gunther Jutz, Patrick van Rijn, Barbara Santos Miranda, and Alexander Boker. Ferritin: a versatile building block for bionanotechnology. *Chemical reviews*, 115(4):1653–1701, 2015.

[16] Masaki Uchida, Michelle L Flenniken, Mark Allen, Deborah A Willits, Bridgid E Crowley, Susan Brumfield, Ann F Willis, Larissa Jackiw, Mark Jutila, Mark J Young, et al. Targeting of cancer cells with ferrimagnetic ferritin cage nanoparticles. *Journal of the American Chemical Society*, 128(51):16626–16633, 2006.

[17] David M Lawson, Peter J Artymiuk, Stephen J Yewdall, John MA Smith, J Craig Livingstone, Amyra Treffry, Alessandra Luzzago, Sonia Levi, Paolo Arosio, Gianni Cesareni, et al. Solving the structure of human h ferritin by genetically engineering intermolecular crystal contacts. *Nature*, 349(6309):541, 1991.

[18] William Kloek, Ton van Vliet, and Marcel Meinders. Effect of bulk and interfacial rheological properties on bubble dissolution. *Journal of Colloid and Interface Science*, 237(2):158–166, 2001.

[19] Günther Jutz. *Mineralized Bionanoparticle Pickering Emulsions*. PhD thesis, University of Bayreuth: Germany, 2008.

[20] P Cicuta and EM Terentjev. Viscoelasticity of a protein monolayer from anisotropic surface pressure measurements. *The European Physical Journal E*, 16(2):147–158, 2005.

[21] Valeria Garbin, John C Crocker, and Kathleen J Stebe. Nanoparticles at fluid interfaces: Exploiting capping ligands to control adsorption, stability and dynamics. *Journal of colloid and interface science*, 387(1):1–11, 2012.

[22] Jacob N Israelachvili. *Intermolecular and surface forces*. Academic press, 2015.

[23] Jayant P Rane, Vincent Pauchard, Alexander Couzis, and Sanjoy Banerjee. Interfacial rheology of asphaltenes at oil–water interfaces and interpretation of the equation of state. *Langmuir*, 29(15):4750–4759, 2013.

[24] Ryan W Murphy, Brian E Farkas, and Owen G Jones. Dynamic and viscoelastic interfacial behavior of β-lactoglobulin microgels of varying sizes at fluid interfaces. *Journal of colloid and interface science*, 466:12–19, 2016.

[25] Giovanni B Brandani, Marieke Schor, Ryan Morris, Nicola Stanley-Wall, Cait E MacPhee, Davide Marenduzzo, and Ulrich Zachariae. The bacterial hydrophobin bsla is a switchable ellipsoidal janus nanocolloid. *Langmuir*, 31(42):11558–11563, 2015.

Chapter 9

Conclusions and Outlook

We conclude this thesis with a summary of each chapter's results and a view on what remains to be addressed. Chapter 1 outlined the understanding of colloid and protein interfacial rheology and introduced our sterically-stabilised model system. Specifically, we sought to explore the effect of particle size on the interfacial rheology and structure so that we might better connect microscopic properties, structure, and rheology.

In chapter 2 we described how we characterised our particles by size (by light scattering) and by contact angle - using a recently developed spectroscopic approach from the literature. We discussed how we measure their interfacial rheology by two commonly used techniques - the Langmuir-Pockels trough and the oscillating pendant drop - and how we complement these techniques with imaging to study the interfacial structure.

Chapter 3 looked at the interfacial structure of three particle sizes in detail. We explored image analysis methods of extracting the surface fraction of particles and saw that for our system (which lacks fine particle resolution for the sub-micron particles) the only approach which worked for all three particle sizes was to count the number of bright pixels in the processed images. We also saw that smaller particles displayed more aggregates at the interface than larger particles did.

Examining the mechanical response of these three particle sizes on the Langmuir-Pockels trough in chapter 4 we found that while there initially appeared to be a difference between them, sonication of the bulk particle dispersions before use made the resulting interfacial structures much more comparable and also made their surface pressure response much more similar, which led us to conclude that size is an unimportant parameter over the range we considered. This result, obtained for sterically-stabilised particles, is consistent with the literature on

charge-stabilised particles.

With size seemingly unimportant to the mechanical properties after sonication we focused on our smallest particle size in chapter 5, using the oscillating pendant drop to measure the dilational rheology. This allowed us to apply the theoretical understanding we developed in chapter 1 to estimate the scaling of the interparticle interaction energy at the interface. This scaling could be explained by a dipolar potential, but also the screened monopole potential reported by Muntz *et al* (see chapter 5) so we do not conclude that we have identified a particular interaction, especially since we assume hexagonal interfacial structure and a straightforward relationship between interparticle potential and average interaction energy per particle. Nevertheless, both explanations are electrostatic in nature, suggesting that these sterically-stabilised particles behave as charge-stabilised particles at the interface.

In chapter 6 we compared our results from chapter 4 to our results from chapter 5. This comparison allowed us both to verify that two different techniques yielded comparable results. Further, it allowed us to discuss an apparent discrepancy in the colloidal interfacial rheology literature where pendant drop and Langmuir-Pockels trough results were explained by adsorption energies only or interaction energies only, respectively. Using the theoretical understanding we developed in chapter 1 we were able to explain this discrepancy as a result of the differing timescales of measurement.

Chapter 7 focused on the collapse mode of the adsorbed colloid layers that we produced. We found a novel mechanism of collapse where interfacial folding resulted in the detachment of said folds. This was found to be consistent with an earlier prediction made in studies of elastic sheets at liquid interfaces, and suggested an analogy with protein behaviour: the highly elastic protein BslA has also shown a similar phenomenon.

Finally, chapter 8 discussed the comparison between particle and protein behaviour, and examined the interfacial rheology of a candidate model protein - ferritin. Like particles, it was also found to have predominantly elastic behaviour, with an elastic modulus proportional to the surface pressure at not-too-high surface pressures. Application of the model developed in chapter 1 for particles to this protein system suggested short-ranged inter-protein interactions, consistent with previous studies.

In summary, we have examined a sterically-stabilised particle system and found that structure varied with size - smaller particles being more aggregated - but the variation vanished when dispersions were sonicated immediately before

use. Measurements of the interfacial rheology led us to improve the theoretical understanding of colloid surface pressure, and we saw that our sterically-stabilised particles behave as charge-stabilised particles do at the interface. We also identified a novel yielding mode for compressed interfaces laden with these particles, which is similar to a mechanism which occurs for BslA. Measurements of ferritin's interfacial rheology found it to be predominantly elastic and suggested that our colloid models may help us to understand protein behaviour. Future studies may address our model's limited treatment of structure, further decrease the minimum sizes of particles considered to connect with nanoparticles, and seek a truly sterically-stabilised interfacial system.